

# 19 A 'Calculate then Interpolate' Approach to Monitoring Regional Moisture Availability

Tim R. McVicar\* and David L.B. Jupp†

## Abstract

This chapter describes a method to estimate moisture availability in the 1.1 million km<sup>2</sup> Murray–Darling Basin (MDB) in southeast Australia. Remotely sensed data from the advanced very high resolution radiometer (AVHRR) are combined with meteorological data to estimate the normalised difference temperature index (NDTI). The NDTI provides a measure of moisture availability, the ratio of actual to potential evapotranspiration. Eighty-five per cent of variation in the modelled NDTI could be explained by surface temperature minus air temperature, per cent vegetation cover and net radiation. These three covariates can be used across the network of meteorological stations to calculate NDTI images, which map changes in moisture availability across the MDB. The method uses a 'calculate then interpolate' (CI) approach: the per-pixel variation present in the AVHRR data is used as the backbone for the spatial interpolation. Using the spatially dense AVHRR-based covariates in a CI approach avoids errors that occur between measurement points when interpolating variables for regional hydrological modelling, most significantly the spatial pattern of rainfall. The NDTI provides a link into regional water balance modelling that does not require spatial interpolation of daily rainfall. Assessing spatial and temporal interactions between the NDTI and the normalised difference vegetation index (NDVI) provides useful information about regional hydroecological processes, including agricultural management, within the context of Australia's highly variable climate and sparse network of meteorological stations.

本文估算了澳大利亚东南部默里达令盆地 (MDB) 一百一十多万平方公里土地的可利用水分。标准差值温度指数 (NDTI) 系由气象台站资料和 AVHRR 遥感数据运算而来, 用以计算有效水分, 即水分蒸发蒸腾实际总量与潜在总量的比例。用地表温度和空气温度的差值、植被覆盖度和净辐射三个变量, 可以较好地解释数值变动 (决定系数  $r^2=85\%$ )。通过气象网络各台站的这三种数据, 可以计算得到 NDTI 图象, 显示 MDB 可利用水分的变化情况。该方法计算后再插值 (CI), 以逐像元变化的 AVHRR 数据为主干, 作

\* CSIRO Land and Water, PO Box 1666, Canberra, ACT 2601, Australia. Email: tim.mcvicar@csiro.au

† CSIRO Earth Observation Centre, PO Box 3023, Canberra, ACT 2601, Australia.

McVicar, T.R. and Jupp, D.L.B. 2002. A 'calculate then interpolate' approach to monitoring regional moisture availability. In: McVicar, T.R., Li Rui, Walker, J., Fitzpatrick, R.W. and Liu Changming (eds), *Regional Water and Soil Assessment for Managing Sustainable Agriculture in China and Australia*, ACIAR Monograph No. 84, 258–276.

空间插值运算。因为在 AVHRR 图像上, 变量的空间分布稠密, 使用 CI 法, 可以避免区域水文模型变量插值测点之间的误差, 作降雨空间分布插值时尤其明显。由于澳大利亚的气候多变, 气象台站分布稀疏, 评估 NDTI 和 NDVI (标准差值植被指数) 间的时空相互作用, 可以提供包括农业活动在内的区域性水文-生态过程的有用信息。

HYDROLOGICAL and plant growth models are often developed at points. One way of extending the models to regions is to interpolate the relevant data and then perform calculations on the interpolated measurements. For example, Cole et al. (1993), Kittel et al. (1995), Carter et al. (1996), Nalder and Wein (1998) and Thornton et al. (1997) interpolated the input parameters and driving variables, and then calculated the values at each location. The interpolation can be a daunting task, depending on the complexity of the model, the spatial and temporal resolution and the extent of the modelling. Chapter 16 discusses the idea of 'data construct'. Another way of extending the models to regions is to use some remotely sensed variables with interpolated meteorological variables and then perform the calculations. Moran et al. (1996), Pierce et al. (1993) and Zhang et al. (1995) have used this approach. Raupach et al. (1997) used output from a general circulation model (GCM) as input to a coupled carbon, water and energy flux model. In this approach the GCM is viewed as an 'interpolator' of the required input meteorological variables for the spatially distributed process model. Prince et al. (1998) use high frequency advanced very high resolution radiometer (AVHRR) data to provide estimates of some of the variables needed for a regional plant growth model, which is run at every point. The approach used in all of these methods can be summarised as 'interpolate then calculate' (IC).

A less frequently used approach is to 'calculate then interpolate' (CI). Stein et al. (1991) first introduced

CI procedures to simulate the moisture deficit for a 404-hectare (ha) area in the Netherlands. They used 399 observations in the modelling framework, where seven procedures (four CI and three IC) were performed. Subsequently, the results for each of the seven were compared with another 100 observations, and a mean squared error (MSE) for each was calculated. Overall, the CI procedures provided lower MSE results than the IC procedures, which led Stein et al. (1991) to state that 'in short, CI procedures are to be preferred over IC procedures'. Bosma et al. (1994) simulated the three-dimensional flow of a heavy metal contaminant and used both IC and CI methods, using ordinary point kriging, to predict a parameter for a 20 m<sup>2</sup> field. They analysed the influence of sample size and concluded that, for the smallest samples, CI procedures performed better than IC procedures. These previous papers provide support for the use of CI in comparison to IC.

Our study integrated data types with very different spatial and temporal scales. AVHRR data are spatially dense, with an at-nadir 1.1 km<sup>2</sup> resolution, and are recorded over large areas in a matter of seconds, at a specific time, for specific wavelengths. Remotely sensed data are therefore a 'census' at a particular spatial scale, recorded at a specific time. Depending on the amount of cloud coverage and the repeat characteristics of the satellite, optical remotely sensed data may be available only weekly or monthly. Meteorological data are recorded sparsely, with the points often separated by tens to hundreds of kilometres. The variables measured at

these points represent a certain area. However, the exact area being represented by a given point measurement is unknown because the spatial autocorrelation is unknown. Meteorological data from standard long-term, large-area surface networks are usually daily integrals (e.g. rainfall ( $P$ ) and wind run ( $U$ )) or daily extremes (e.g. maximum ( $T_x$ ) and minimum ( $T_n$ ) air temperatures) acquired regularly over decades. Thus, remotely sensed data are spatially dense but temporally sparse, while meteorological data are spatially sparse but temporally dense. One aim of our research was to combine the high temporal density of meteorological data with the high spatial density of remotely sensed data. The inherent spatial density of remotely sensed data may be compromised by the IC approach. As a result, geographic information system (GIS) boundaries may lead to artefacts in the final modelled images.

We used covariates derived mainly from spatially dense AVHRR data to spatially interpolate the normalised difference temperature index (NDTI). The approach is very similar to using a digital elevation model (DEM) as a covariate to interpolate surfaces of air temperature. Various numerical approaches can be used to spatially interpolate point data (Lam 1983); two of the most popular are splines and kriging. Several recent papers (e.g. Dubrule 1983; Dubrule 1984; Hutchinson 1993; Hutchinson and Gessler 1994; Laslett 1994; Borga and Vizzaccaro 1997) have compared the outputs from splines and kriging and found little difference between the two in most circumstances, provided the interpolation parameters were selected carefully. Incorporating regular gridded data, usually a DEM, but in this case AVHRR-based variables, as a covariate can be performed routinely using ANUSPLIN (Hutchinson 1997), a commercially available software package. Any spline or kriging package that can utilise covariates can be used to spatially interpolate NDTI.

## The Normalised Difference Temperature Index

Jackson et al. (1977) developed the following empirical model to estimate daily actual evapotranspiration ( $\lambda E_{a\_DAY}$ ):

$$\lambda E_{a\_DAY} - R_{n\_DAY} = A - B(T_s - T_a)$$

where  $R_{n\_DAY}$  is the daily net radiation in watts per square metre ( $W/m^2$ ),  $T_s$  is the surface temperature (K),  $T_a$  is the air temperature (K), and  $A$  and  $B$  are empirical coefficients. Seguin et al. (1982a, 1982b) extended this approach. Lagouarde (1991) described how the approach could be implemented and noted that the effect of changes in surface cover type and amount (especially roughness length) on the coefficient  $B$  were not addressed by the model. Courault et al. (1996) extended the work and provided alternative parameterisations for  $B$ . In principle,  $A$  and  $B$  should be consistent over areas with similar land cover structure.

The crop water stress index (CWSI) was originally developed at the agricultural field and daily time scale (Jackson et al. 1981). AVHRR-based estimates of actual evapotranspiration ( $\lambda E_{a\_AVHRR}$ ) to  $\lambda E_{a\_DAY}$  are usually related using the approximation of Jackson et al. (1983), which has been extended by Xie (1991). Both are in the context of agricultural field-scale experiments.

There is an alternative to using spatial variance in remotely sensed data to map  $\lambda E_{a\_DAY}$ .  $T_s$  can be linked with meteorological variables if the meteorological data have the same temporal resolution as the remotely sensed data. High temporal resolution (e.g. every minute) meteorological data usually require intensive field campaigns for small, well-instrumented catchments. However, McVicar and Jupp (1999a) have recently shown that meteorological variables at the time of remotely sensed data acquisition can be adequately estimated from daily meteorological data for use with a resistance energy balance model

(REBM). This allows the development of a ‘dual’ approach to the well-known CWSI. Consequently, large regions in an operational framework can be monitored to derive a spatially varying index of moisture availability ( $m_a$ , the ratio of actual evapotranspiration to potential evapotranspiration ( $\lambda E_p$ )) from daytime  $T_s$ . The development of the NDTI undertakes this dual approach. The NDTI is defined as:

$$NDTI = \frac{(T_\infty - T_s)}{(T_\infty - T_0)} \quad (1)$$

The two bounding temperatures,  $T_0$  and  $T_\infty$ , are derived by inverting an REBM.  $T_0$  is an REBM inverted surface temperature when  $r_s$  (the composite surface resistance) = 0 s/m — that is, when it is assumed  $\lambda E_a = \lambda E_p$ .  $T_\infty$  is an REBM inverted surface temperature when  $r_s = \infty$  s/m — that is, when it is assumed  $\lambda E_a = 0$  W/m<sup>2</sup>. The methods and assumptions used here are discussed fully in Jupp et al. (1998). In our study, daytime  $T_s$  is derived from the AVHRR sensor; however, it could be derived from any other space, or airborne, thermal sensor. If the REBM and the meteorological data —  $T_a$  vapour pressure ( $e_a$ ), shortwave radiation ( $R_s$ ) and wind speed ( $u$ ) — estimated at the time of AVHRR data acquisition, are well defined, a time series of  $T_s$  should fall within the envelope defined by the limits  $T_0$  and  $T_\infty$ . McVicar and Jupp (1998) presented this relationship for five years of AVHRR  $T_s$  data recorded at Cobar, Australia.

The NDTI can be regarded as a specific time-of-day version of the CWSI. The NDTI brings the concept of mapping  $m_a$  from  $T_s$  onto a regional basis and is generic across different land surfaces by using the per-pixel variation present in the AVHRR data as the backbone for the spatial interpolation. This is achieved by developing suitable spatial covariates that incorporate AVHRR per-pixel variation. Both  $T_s - T_a$  and  $R_n$  are potential covariates (Jackson et al. 1977). Vegetation cover ( $VegCov$ ) is a potential covariate if changes in surface cover type and amount are to be incorporated.

## Data Sets

Our requirements for daily meteorological data are modest: only  $T_m$ ,  $T_x$  and  $P$  are essential. However, in the 1.1 million km<sup>2</sup> Murray–Darling Basin (MDB), only 63 Australian Bureau of Meteorology (ABM) stations have measured this data continuously from 1980 until the present. Figure 1 shows the location of the MDB and of the relevant meteorological sites. If available, daily  $U$  (km/day) was used to estimate  $u$  (m/s) (McVicar and Jupp 1999a). The northwest cloudband is a synoptic scale feature of the Australian region (Colls and Whitaker 1990), so 13 additional ABM stations to the north and west of the MDB were included in the meteorological database. Within the extended NDTI study area, there are 70 ABM stations, of which 57 are in the basin and an additional 13 are to the north and west of the basin.

Remotely sensed data were acquired by the AVHRR sensor on board the NOAA-9 and NOAA-11 satellites. Cracknell (1997) provides an extensive overview of the AVHRR sensor, the NOAA series of satellites and some previous applications of AVHRR data. The data archive that focuses on the MDB consists of 97 AVHRR single overpass afternoon images from June 1986 to January 1994, recorded at approximately monthly time intervals.

## Selecting the Spatial Covariates

At Cobar (Fig. 1) daily meteorological data  $T_m$ ,  $T_x$ ,  $P$  and  $U$  were linked using the procedures described in McVicar and Jupp (1999a) to estimate  $T_a$ ,  $e_a$ ,  $R_s$  and  $u$  at the times of AVHRR data acquisition. The data were used with variables routinely derived from AVHRR data ( $T_s$ ,  $VegCov$  and albedo ( $\alpha$ )) in the REBM (Jupp et al. 1998) to model NDTI and  $\lambda E_a$ . This was performed only for the 73 cloud-free AVHRR overpasses at Cobar.

The utility of each of the three potential covariates ( $T_s - T_a$ ;  $VegCov$ ; and  $R_n$ ) was evaluated by linearly regressing them against the REBM outputs of NDTI

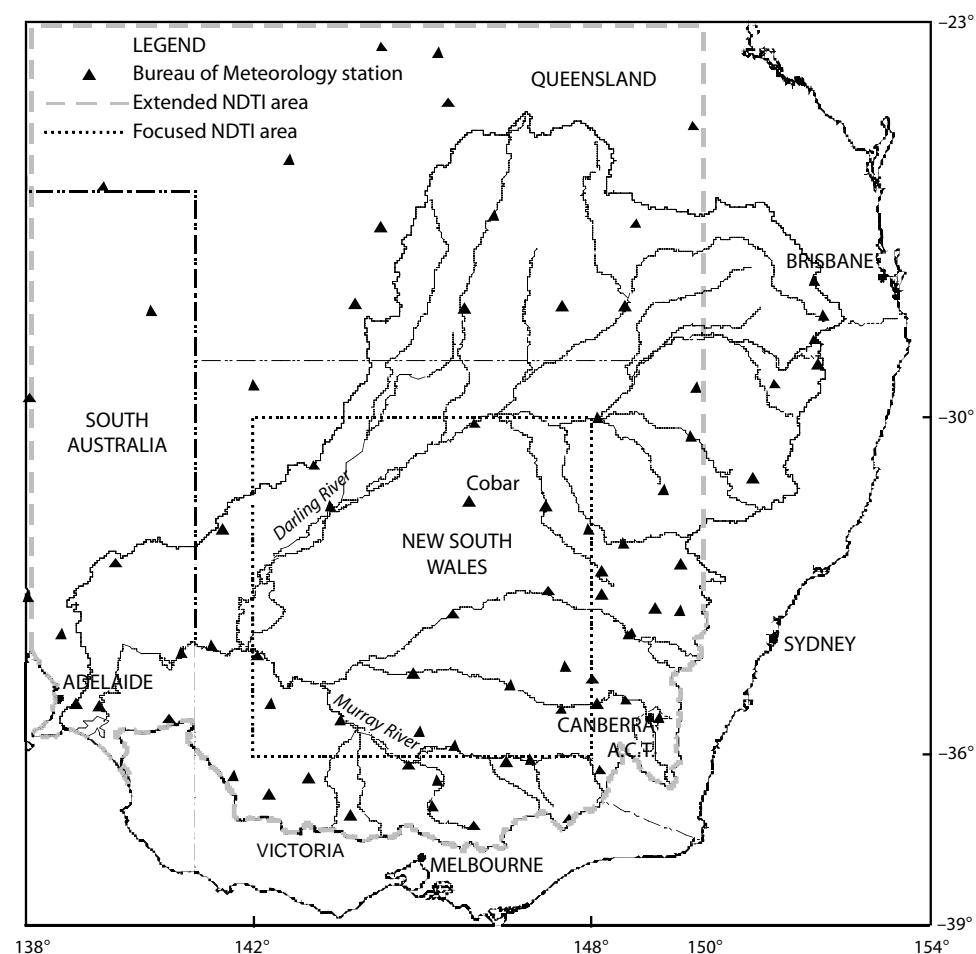


**Figure 1.** Location of sites in the Murray–Darling Basin, Australia. The sites of the 76 Australian Bureau of Meteorology (ABM) stations are indicated. The focus and extended normalised difference temperature index (NDTI) study areas are shown.

or  $\lambda E_a$ . Multiple linear regression was used as required. Table 1 shows the results. Only data with  $r_s$  greater than 0 s/m and  $R_n$  greater than  $125 \text{ W/m}^2$  were used in the analysis. Increasing the  $R_n$  threshold increased the  $r^2$  statistic but reduced the number of observations in the analysis, and vice versa. The threshold of  $R_n > 125 \text{ W/m}^2$  was a pragmatic balance between the strength of the relationship between the three potential covariates and the REBM NDTI, and the number of observations used (McVicar and Jupp 1999b).

Table 1 shows the results of the regression analysis between the REBM NDTI and one potential

covariate in turn.  $T_s - T_a$  had the largest  $r^2$  and lowest standard error of the estimate of Y on X (SEY). Multiple linear regression analysis showed that  $T_s - T_a$  and  $R_n$  were able to explain 79% of the variance within the NDTI, while  $T_s - T_a$  and  $VegCov$  were able to explain only 60% (Table 1). When all three potential covariates were used, 85% of the variance within the NDTI was explained and the SEY was less than 0.1.

It is interesting to note that when we regressed  $\lambda E_a$  against each potential covariate in turn,  $R_n$  provided the highest  $r^2$  and the lowest SEY (Table 1). The  $r^2$  and SEY values when both  $T_s - T_a$  and  $R_n$  were used

were almost identical to the values when  $T_s - T_a$ ,  $R_n$  and  $VegCov$  were used (Table 1). This indicates that, if interpolating  $\lambda E_a$  rather than  $m_a$ ,  $VegCov$  is not as important as  $T_s - T_a$  and  $R_n$ .

We calculated regression model estimates of the NDTI and  $\lambda E_a$ —denoted NDTI' and  $\lambda E_a'$  respectively—based on one covariate ( $T_s - T_a$ ), two covariates ( $T_s - T_a$  and  $R_n$ ) or three covariates ( $T_s - T_a$ ,  $R_n$  and  $VegCov$ ). We then cross-plotted them against the REBM NDTI or REBM  $\lambda E_a$ , respectively. Figures 2a–c show the results for NDTI when three covariates were used for the modelling. The use of three covariates explained most of the variance of the REBM NDTI (Fig. 2a–c). This confirms that all three potential covariates should be developed as spatial surfaces to interpolate the NDTI. This is not necessary for spatially interpolating  $\lambda E_a$  by comparing  $\lambda E_a'$  with REBM  $\lambda E_a$ ; Figures 2d–f show that this regression can be performed adequately using only  $T_s - T_a$  and  $R_n$  as spline model covariates.

### Developing the Spatial Covariates

We used the CI approach to interpolate the NDTI, which was calculated at the ABM stations (considered points in the MDB) and then spatially

interpolated. We used the following data to develop continuous grids, to be used as covariates, or in the modelling of  $R_n$ :

- interpolated meteorological data ( $T_a$ ,  $e_a$  and effective beam transmittance at 0 m ( $\tau_0$ ));
- remotely sensed data ( $T_s$  and  $\alpha$ );
- supervised classification of AVHRR reflective data used as a GIS stratum with the time series of AVHRR reflective data ( $VegCov$ ); and
- $R_n$  modelled using all of the above six variables as inputs.

Figure 3 illustrates the development of the six input variables required to generate  $R_n$ ; Figure 4 shows how  $R_n$  is calculated.  $T_s - T_a$  and  $VegCov$  are developed from some of the six variables. The following discussion provides further details of the methods used to develop the spatial covariates and intermediate variables, and the results we obtained.

### Air temperature ( $T_a$ )

Continuous grids of  $T_a$  for the specific times of AVHRR data acquisition were calculated in a two-step process. First,  $T_a$  was temporally interpolated from  $T_n$  and  $T_x$  to provide estimates of  $T_a$  at the 70

**Table 1.** Regression analysis using REBM NDTI or REBM  $\lambda E_a$  as the dependent variable and the potential covariates as the independent variable(s).

Independent variable(s)	Dependent variable					
	REBM NDTI			REBM $\lambda E_a$		
	$r^2$	SEY	df	$r^2$	SEY	df
$T_s - T_a$	0.42	0.17	47	0.01	67.1	47
$R_n$	0.00	0.23	47	0.38	53.0	47
$VegCov$	0.31	0.19	47	0.21	59.7	47
$T_s - T_a$ and $R_n$	0.79	0.11	46	0.95	15.4	46
$T_s - T_a$ and $VegCov$	0.60	0.14	46	0.21	60.3	46
$T_s - T_a$ , $R_n$ and $VegCov$	0.85	0.09	45	0.97	12.5	45

df = degrees of freedom; NDTI = normalised difference temperature index;  $r^2$  = coefficient of determination; REBM = resistance energy balance model; SEY = standard error of the estimate of Y on X. See text for an explanation of the other symbols. There were 49 observations.

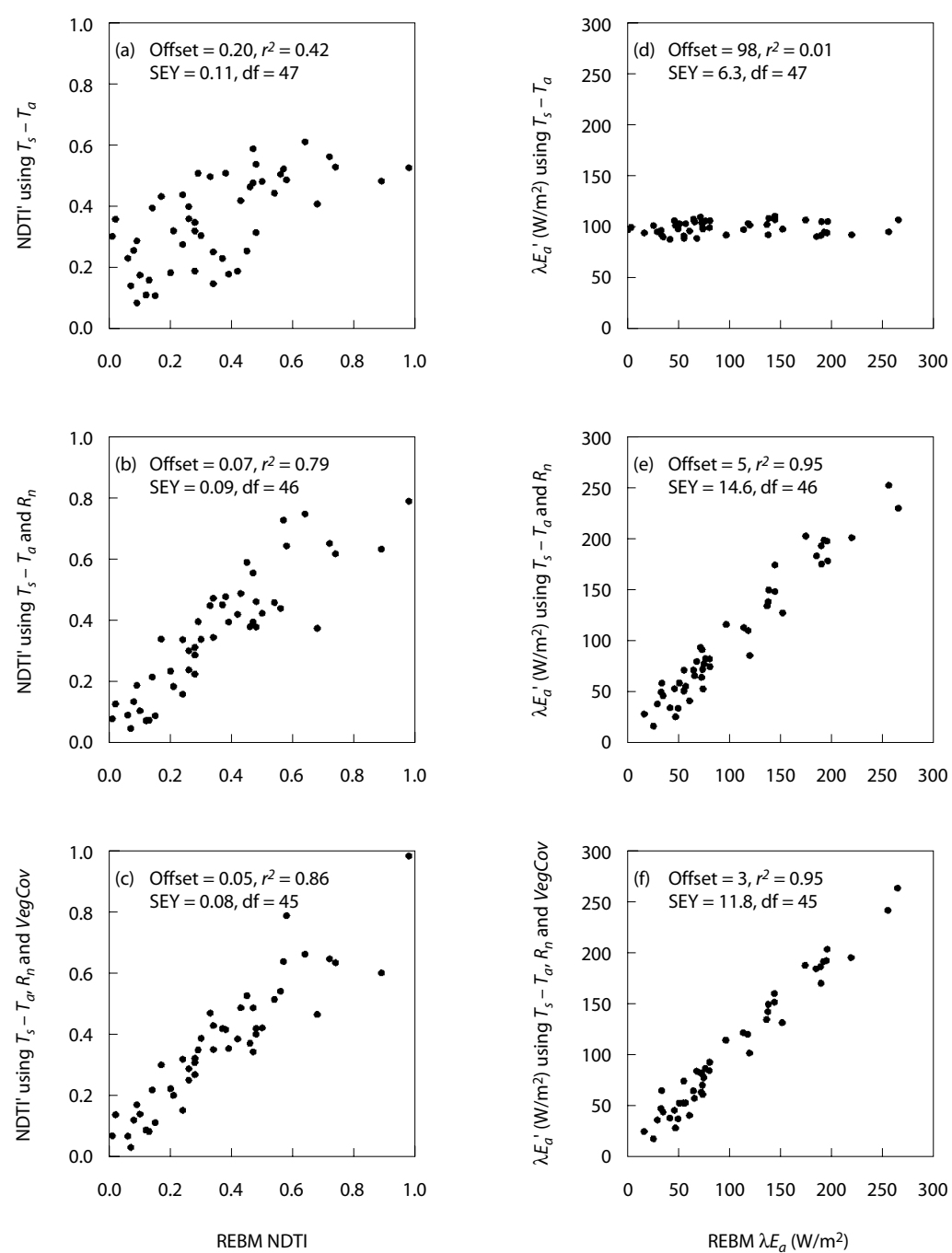


**Figure 2.** Cross-plots of resistance energy balance and regression models. (a) to (c) show resistance energy balance model (REBM) normalised difference temperature index (NDTI) with regression model NDTI'; (d) to (f) show REBM  $\lambda E_a$  with regression model  $\lambda E_a'$ . The regression models are based on (a) and (d)  $T_s - T_a$ ; (b) and (e)  $T_s - T_a$  and  $R_n$ ; (c) and (f)  $T_s - T_a$ ,  $R_n$  and VegCov. SEY = standard error of the estimate of Y on X. See text for an explanation of the terms used.

ABM stations, denoted  $T_{a\_AVHRR\_PT}$  in Figure 3. Second, the values of  $T_{a\_AVHRR\_PT}$  were spatially interpolated to generate continuous grids of  $T_a$  for the extended NDTI study site (Fig. 1), denoted  $T_{a\_AVHRR\_GD}$  in Figure 3.

To select the spline model parameters, we undertook a detailed analysis using  $T_{a\_AVHRR\_PT}$  supporting the AVHRR overpass acquired by NOAA-9 Orbit Number 14301, 22 September 1987 at 1629 local time. The influence of elevation was incorporated into the thin plate spline (TPS) by fitting the data with four variations:

- bivariate TPS function of longitude and latitude;

- trivariate partial thin plate spline (PTPS), incorporating a bivariate TPS function of longitude and latitude and a constant linear dependence on elevation;
- trivariate TPS function of longitude, latitude and elevation, in the units of metres; and
- trivariate TPS function of longitude, latitude and elevation, in the units of kilometres.

When using elevation (or any other variable) as an independent spline variable in a TPS, the units can influence the output surface. Hutchinson (1995) explored the scaling of elevation when interpolating mean monthly rainfall: elevation data expressed as

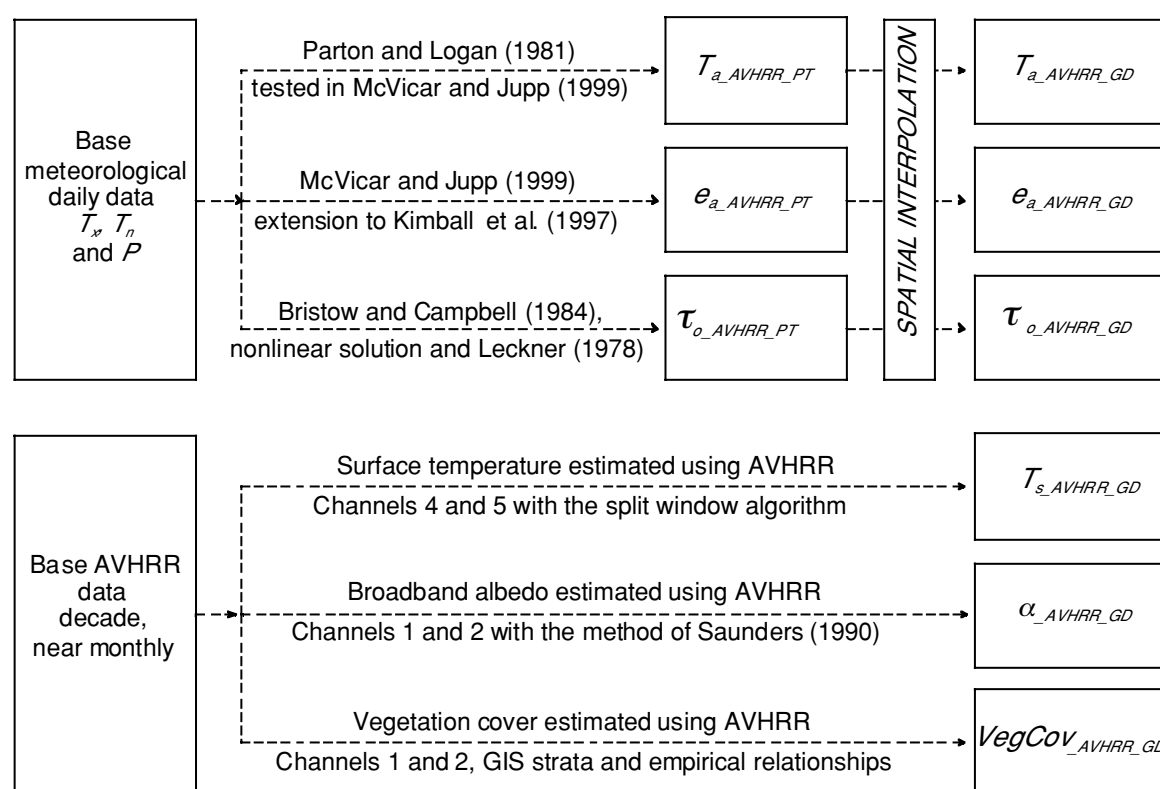


**Figure 3.** Development of the required variables at the specific time of day when advanced very high resolution radiometer (AVHRR) data are acquired.

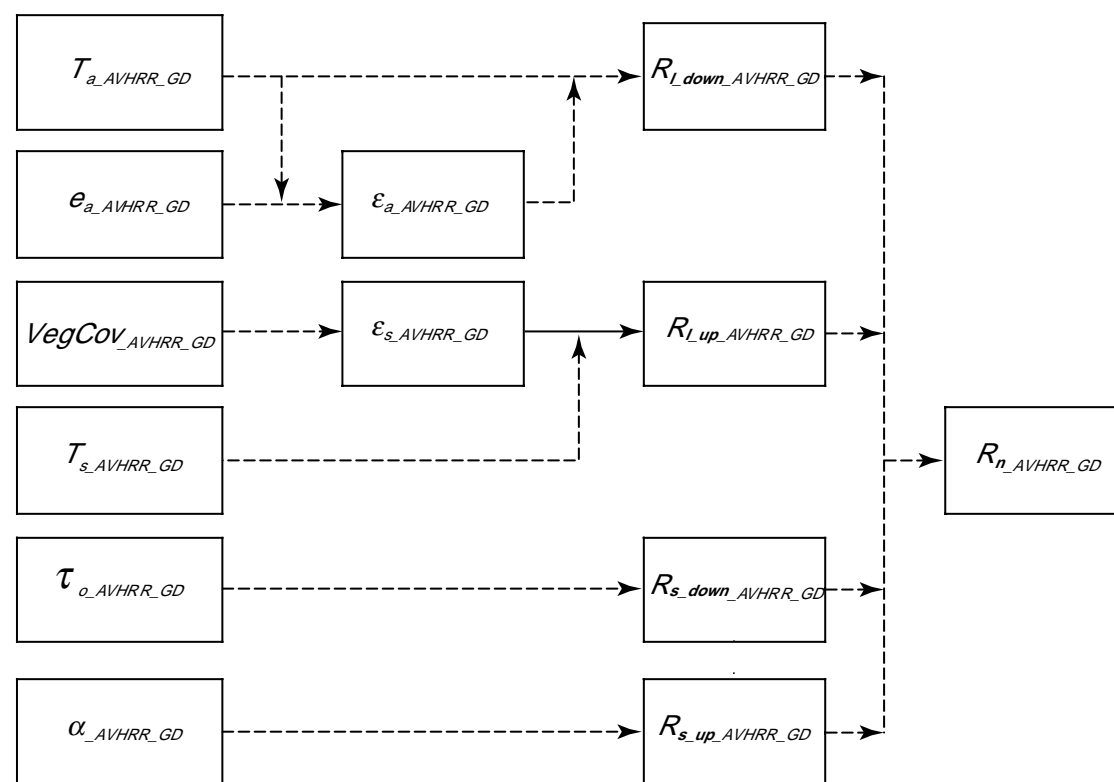
The six variables are derived from two main sources. Daily meteorological data ( $T_n$ ,  $T_x$  and  $P$ ) are used to estimate  $T_a$ ,  $e_a$  and  $\tau_o$ . Then these three variables are spatially interpolated. AVHRR data are used to estimate  $T_s$ ,  $\alpha$  and  $VegCov$ .  $T_s - T_a$  and  $VegCov$  are used as covariates. All six variables are used in modelling the third covariate  $R_n$  (see Fig. 4). The subscript *AVHRR* refers to the specific time of day that AVHRR data are acquired; the subscript *PT* refers to measurements made at a 'point'; the subscript *GD* refers to measurement, or interpolated output, which is a continuous 'grid'.

kilometres were both convenient and in the range of units that provided a minimal validation residual. For TPS, the range of all independent variables should be approximately equal. However, scaling of elevation does not influence the output statistics if the TPS is extended to a PTPS by including elevation as a linear parametric submodel. This is the case for all covariates. As shown above, we scaled the elevation in metres or kilometres when using a trivariate TPS. The order of the partial derivative ( $m$ ) was varied from 2 to 4 (three cases) for each of the four cases shown in the above bullet points, resulting in a total of 12 options.

For all 12 spline models, the smoothing parameter ( $\lambda$ ) was automatically selected by minimising the generalised cross-validation error, denoted as  $GCV(m, \lambda)$ . McVicar and Jupp (1999b) present full

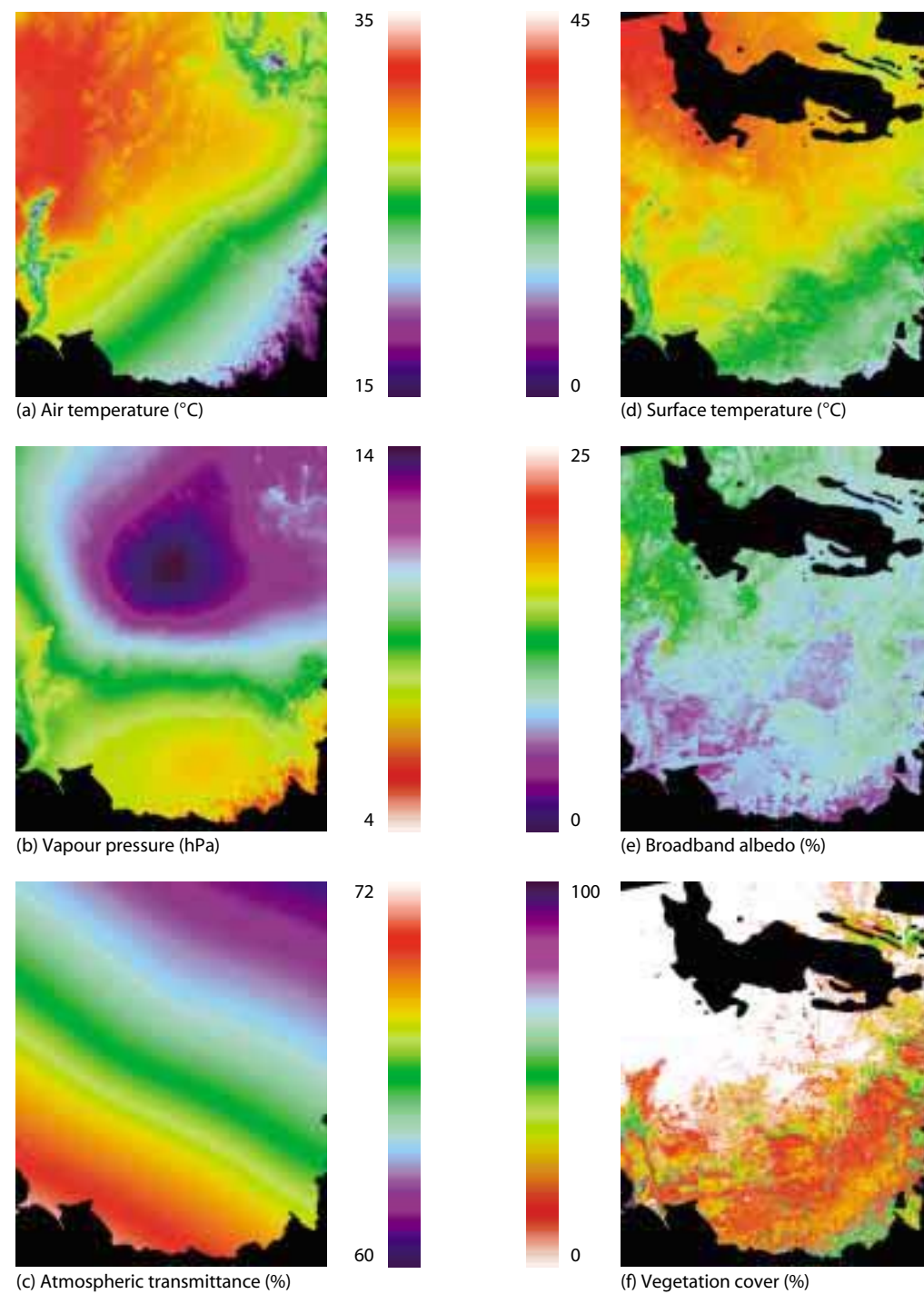
statistics for all 12 options. The trivariate TPS with elevation in kilometres  $m = 3$  had the lowest  $\sqrt{GCV(m, \lambda)}$  ( $0.792^\circ\text{C}$ ) and this spline model was used to spatially interpolate the 97 surfaces of  $T_{a\_AVHRR\_GD}$ , using  $T_{a\_AVHRR\_PT}$  as input data (Fig. 3).

Figure 5a shows the output for 22 September 1987.  $T_a$  gradually increases from the southeast to the northwest, but this trend is modified by local changes in elevation. The northwest portion is considered semiarid; in the southeast during September (the southern hemisphere spring), if drought conditions are not experienced, there is a spring growth flush of cereal crops (wheat, barley and oats). The 97 continuous grids of  $T_a$  were calculated and used with the other variables as required to develop the covariates (Fig. 4).



**Figure 4.** Development of  $R_n$ .

$R_l$  and  $R_s$  refer to longwave and shortwave radiation, respectively; the subscript 'down' refers to radiative fluxes from the atmosphere towards the land surface; the subscript 'up' refers to radiative fluxes from the land surface toward the atmosphere. Refer to Figure 3 for the development of the six input variables.



**Figure 5.** Continuous grids of the six required variables. The required variables are (a)  $T_a$  (°C); (b)  $e_a$  (hPa); (c)  $\tau_0$  (%); (d)  $T_s$  (°C); (e)  $\alpha$  (%); and (f)  $VegCov$  (%) for the extended normalised difference temperature index (NDTI) area shown in Figure 1. Variables (a), (b) and (c) are derived from spatial interpolation based on data recorded at the 70 ABM stations. Variables (d), (e) and (f) are derived from advanced very high resolution radiometer (AVHRR) data, some of which are not reliable because they are cloud affected; these data have been nulled and are shown in black. Note the difference in the smoothness of the output based on the source of the data. Refer to Figure 3 for the development of the six variables.

### Vapour pressure ( $e_a$ )

Continuous grids of  $e_a$  for the specific times of AVHRR data acquisition were calculated using two steps. The first was to temporally estimate  $e_a$ . Recently Kimball et al. (1997) estimated dew point temperature based on empirical regressions between  $T_x$  and  $T_m$ , and an introduced term 'EF', which is the ratio of Priestly–Taylor  $\lambda E_{p\_DAY}$  divided by annual precipitation. The assumption that  $e_a$  remains constant throughout the day was improved upon by linearly interpolating  $e_a$  between the times of sunrise for consecutive days, denoted K97 'interpolation' in McVicar and Jupp (1999a). The K97 interpolation method was used to develop  $e_{a\_AVHRR\_PT}$  (Fig. 3) estimates at the 70 ABM stations (Fig. 1). In the second step, the values of  $e_{a\_AVHRR\_PT}$  were spatially interpolated to generate continuous grids of  $e_a$  for the extended NDTI study site (Fig. 1), denoted  $e_{a\_AVHRR\_GD}$  in Figure 3. To test the sensitivity of  $m$  and the use of and units of elevation as a covariate (Jackson et al. 1985) in developing  $e_{a\_AVHRR\_GD}$ , we used the same 12 spline models used for  $T_a$ .

For all 12 spline models,  $\lambda$  was again automatically selected by minimising  $GCV(m, \lambda)$ . The model with the lowest  $\sqrt{GCV(m, \lambda)}$  is the trivariate PTPS  $m = 2$  (1.11 hPa). McVicar and Jupp (1999b) provide full statistics for all 12 spline models. Figure 5(b) shows the output for 22 September 1987. The area of high  $e_a$  in the northern portion of Figure 5(b) approximately conforms to the area identified as cloud in the AVHRR data (Fig. 5d–f). The 97 continuous grids of  $e_a$  were calculated and used to model atmospheric emissivity ( $\epsilon_a$ ) (Fig. 4).

### Atmospheric transmittance ( $\tau_0$ )

Calculating continuous grids of  $\tau_0$  for the specific days of AVHRR data acquisition is a two-step process. First, we calculated  $\tau_{0\_AVHRR\_PT}$  (Fig. 3), for each of the 97 AVHRR days at each of the 70 ABM stations. McVicar and Jupp (1999b) present full details. Second, we spatially interpolated  $\tau_{0\_AVHRR\_PT}$  to provide continuous grids of  $\tau_0$ ,

denoted  $\tau_{0\_AVHRR\_GD}$  (Fig. 3), using a TPS. Detailed results for the spatial interpolation of  $\tau_{0\_AVHRR\_GD}$ , using  $\tau_{0\_AVHRR\_PT}$  as the input data, for the bivariate TPS varying  $m$  from 2 to 4 were examined. As with  $T_a$ ,  $\lambda$  was automatically selected by minimising  $GCV(m, \lambda)$ . The bivariate TPS  $m = 2$  has the lowest  $\sqrt{GCV(m, \lambda)}$  (0.0157%). McVicar and Jupp (1999b) provide the complete listing of output statistics. Elevation was not incorporated in this spline model as the relationship between  $\tau_0$  and elevation is implicitly defined by using a DEM in the calculation of downward short-wave radiation ( $R_{s\_down}$ ).  $\tau_{0\_AVHRR\_GD}$  is assumed constant over the day; the specific time of day, day of year and geographical position of each resampled AVHRR pixel centre are used to determine transmission path length ( $p$ ) and cosine of the solar zenith angle ( $\cos\theta_z$ ).

Figure 5c shows this output for 22 September 1987; the area of lower  $\tau_0$  approximately conforms to the area of higher  $e_a$  (shown in Fig. 5b) and is identified as cloud in Figure 5d–f. The 97 continuous grids of  $\tau_0$  are used to calculate  $R_{s\_down}$  (Fig. 4).

### Surface temperature ( $T_s$ )

$T_{s\_AVHRR\_GD}$  is calculated using a split-window approach, which takes advantage of the differential atmospheric absorption observed in AVHRR channels 4 and 5. The radiance measured by AVHRR channels 4 and 5 is converted to brightness temperatures, denoted  $T_4$  and  $T_5$  respectively, using Planck's law. An estimate of brightness  $T_s$ , denoted  $Tb_s$ , has then been developed using the formula  $Tb_s = T_5 + 3 \Delta T_{4,5} + 0.5$ , where  $\Delta T_{4,5}$  is  $T_4 - T_5$ . The split-window coefficients were determined by simulating the absorption coefficients for the AVHRR channel 4 and 5 bandwidths using Australian atmospheric data (Maher and Lee 1977) and the LOWTRAN6 package (Kneizys et al. 1983).  $T_s$  estimates were obtained by correcting the data for emissivity, based on pixel fractional  $VegCov$  using 0.98 for vegetation emissivity ( $\epsilon_v$ ) and 0.96 for ground (or soil) emissivity ( $\epsilon_g$ ) (Wan and Dozier 1996). Generating  $T_{s\_AVHRR\_GD}$  does not require any spatial interpolation.

Figure 5d shows the increase in  $T_s$  toward the semiarid area in the northwest; lower  $T_s$  values to the southeast are associated with an increase in  $m_a$ . The increases in  $\lambda E_a$  are associated with an increase in  $VegCov$  due to the spring growth flush of cereal crops (Fig. 5f). Cloud clearing means that AVHRR data are available only when there was no cloud. The 97 images of  $T_s$  were calculated and used with the other variables as required to develop the covariates (Fig. 4).

### Broadband albedo ( $\alpha$ )

$\alpha_{AVHRR\_GD}$  was calculated using the Saunders (1990) model with AVHRR channels 1 and 2 (Fig. 3). Sensor drift degradation was taken into account using the methods provided by Mitchell (1999). The resulting effective reflectance factor is used in the Saunders model to estimate  $\alpha_{AVHRR\_GD}$  for all 97 AVHRR images. Figure 5e is an example of  $\alpha$ ; the high albedo area to the west is Lake Frome, a salt lake; the very small area to the southeast is snow cover on the Australian Alps. Remnant forests and woodlands have the lower albedos. The 97 images of  $\alpha$  were calculated and used to model the shortwave radiation reflected upward by the surface ( $R_{s\_up}$ ) (Fig. 4).

### Vegetation cover

$VegCov_{AVHRR\_GD}$  is calculated as continuous grids for the specific days of AVHRR data acquisition in a two-step process. Firstly, we defined a stratum of woody and nonwoody vegetation by classifying reflective AVHRR data from several dates throughout 1987 into a woody/nonwoody vegetation stratum. Secondly, we developed empirical relationships between in situ leaf area index (LAI) and AVHRR channels 1 (Red) and 2 (NIR). For nonwoody vegetation,  $LAI = -1.15 + 0.96 \times (NIR/Red)$  (McVicar et al. 1996a); for woody vegetation,  $LAI = -4.65 + 4.22 \times (NIR/Red)$  (McVicar et al. 1996b). Finally  $LAI_{AVHRR\_GD}$  were converted into estimates of  $VegCov$  using the relationship  $VegCov = 100.0 \times (1.0 - \exp^{-LAI/2})$ , assuming random distribution of foliage above the

soil and uniform leaf-angle distribution (Choudhury 1989).

Figure 5f illustrates this output for 22 September 1987. The areas of higher amounts of  $VegCov$  are remnant forests and woodlands; the large expanse of moderate values across the southern portion of the image (Fig. 5f) is due to the spring growth flush of cereal crops. The large expanse with 0%  $VegCov$  toward the northwest is semiarid (Fig. 5f) and corresponds to the area of high  $T_s$  in Figure 5d.  $VegCov$  is used as a covariate and is also used to calculate surface emissivity ( $\epsilon_s$ ).

### Net radiation ( $R_n$ )

$R_n$  can be expressed as the sum of its four components:

$$R_n = R_{s\_down} - R_{s\_up} + R_{l\_down} - R_{l\_up} \quad (2)$$

where  $R_s$  is short-wave radiation and  $R_l$  is longwave radiation. The components can be calculated from the six variables introduced above (see Fig. 4). An IC approach is used for  $R_n$  because  $R_n$  is strongly influenced by  $\alpha$  and  $T_s$ , which can be discontinuous due to land use (e.g. when agricultural land is adjacent to remnant forest). Information about  $\alpha$ ,  $T_s$  and  $VegCov$  is obtained directly from the spatially dense AVHRR data (Fig. 3). This means that changes in  $\alpha$ ,  $T_s$  and  $VegCov$  are accounted for in space—at  $1/64^{\text{th}}$  of a degree, the spatial resolution of the resampled AVHRR data—and in time, near monthly, the temporal resolution in the AVHRR data base.

The methods used to model the radiation components are fully documented in McVicar and Jupp (1999b) and are briefly documented below.  $R_{s\_down}$  is modelled by:

$$R_{s\_down} = \tau_0^{\frac{P}{P_0}} \cos \theta_s Q'_0 \quad (3)$$

where  $P$  is the total pressure (the subscripts denote the altitude above a zero height surface) and  $Q'_0$  is

the exoatmospheric normal solar irradiance modified for sun–earth distance. The input variables required are:

- a continuous raster of  $\tau_0$  (see above);
- the specific time of day, day of year and geographical position of the pixel centre of resampled AVHRR data (used to determine  $p$  and  $\cos\theta_s$ );
- a continuous raster of height, obtained from AUSTDEM Ver 4.0; and
- slope and aspect, derived from the DEM (used to modify the calculation) (Iqbal 1983).

$R_{s\_up}$  is the fraction of  $R_{s\_down}$  reflected by the surface; this is controlled by  $\alpha$ .  $R_{l\_down}$  is calculated using the method described in Kustas et al. (1989), in which  $\epsilon_a$  and  $T_a$  are variables. The estimate of  $\epsilon_a$  relies on  $e_a$  and  $T_a$  (Brutsaert 1975). To calculate  $R_{l\_up}$ , both  $\epsilon_s$  and  $T_s$  are required (Kustas et al. 1989).  $\epsilon_s$  is calculated from  $VegCov$ , using 0.98 for  $\epsilon_v$  and 0.96 for  $\epsilon_g$  (Wan and Dozier 1996). The relatively small component of outgoing longwave radiation by reflected sky radiation is ignored (Jackson et al. 1985).

We developed the components of  $R_n$  using the methods described above and summarised in Figure 4. In Figure 6a the longitudinal banding of  $R_{s\_down}$  is due to changes in  $p$  and  $\cos\theta_s$  when the AVHRR data were acquired at 1629 local time. Modification by elevation, slope and aspect are shown. Figure 6b illustrates the influence of  $\alpha$  and banding of  $R_{s\_down}$  on  $R_{s\_up}$ . The spatial pattern of  $R_{l\_down}$ , shown in Figure 6c is dominated by  $T_a$ .  $R_{l\_up}$  (Fig. 6d) follows the spatial variability present in  $T_s$ . The components have been added together (Equation 2) to provide continuous rasters of  $R_n$ , denoted  $R_{n\_AVHRR\_GD}$ , which is used as a covariate.  $R_{n\_AVHRR\_GD}$  for 22 September 1987 is illustrated in Figure 7c.

## Applying the Spatial Covariates to the Murray–Darling Basin

We used the CI approach to develop the 97 surfaces of the NDTI for the focus area of the MDB. The NDTI (Equation 1) was calculated at the ABM stations shown in Figure 1. To generate continuous NDTI surfaces, we used a quintivariate PTPS, incorporating a bivariate TPS function of longitude and latitude with constant linear dependencies on  $T_s - T_a$ ,  $VegCov$  and  $R_n$  (see Figures 7a, b and c respectively). To select the spline model, we varied  $m$  from 2 to 4 and assessed its influence (McVicar and Jupp 1999b). We examined detailed results for the spatial interpolation of NDTI for the three options  $m = 2$  to 4; full results are presented in McVicar and Jupp (1999b). As with  $T_a$  above,  $\lambda$  was automatically selected for the spline models by minimising  $GCV(m, \lambda)$ . The model with the lowest  $\sqrt{GCV(m, \lambda)}$  was the quintivariate PTPS with three covariates  $m = 2$ .

The high spatial density of AVHRR data is seen in the resulting NDTI images. Figure 8a shows the NDTI image for spring (22 September 1987) and Figure 8b shows the NDTI image for summer (25 December 1987). Changes in the NDTI between the two dates are shown in Figure 8c, where blue is an increase, green fairly constant and red a decrease between the two dates. Figure 8a shows that the Menindee Lakes system is the only area where NDTI is greater than 0.8, with the southern portion of the wheatbelt in the southeast having an NDTI of about 0.5. Some areas around the Menindee Lakes also have an NDTI of about 0.5; these are assumed to have received scattered rainfall. Figure 5d shows the larger extent of this pattern, confirmed by a decrease in  $T_s$ . In Figure 8b some areas with an NDTI greater than 0.8 are lakes while others are associated with flood irrigation of crops and remnant river red gum forests (Barham and Gulpa State Forests) along the Murray River. On the Cobar peneplain there are scattered areas with NDTI values of approximately 0.5, which corresponds to

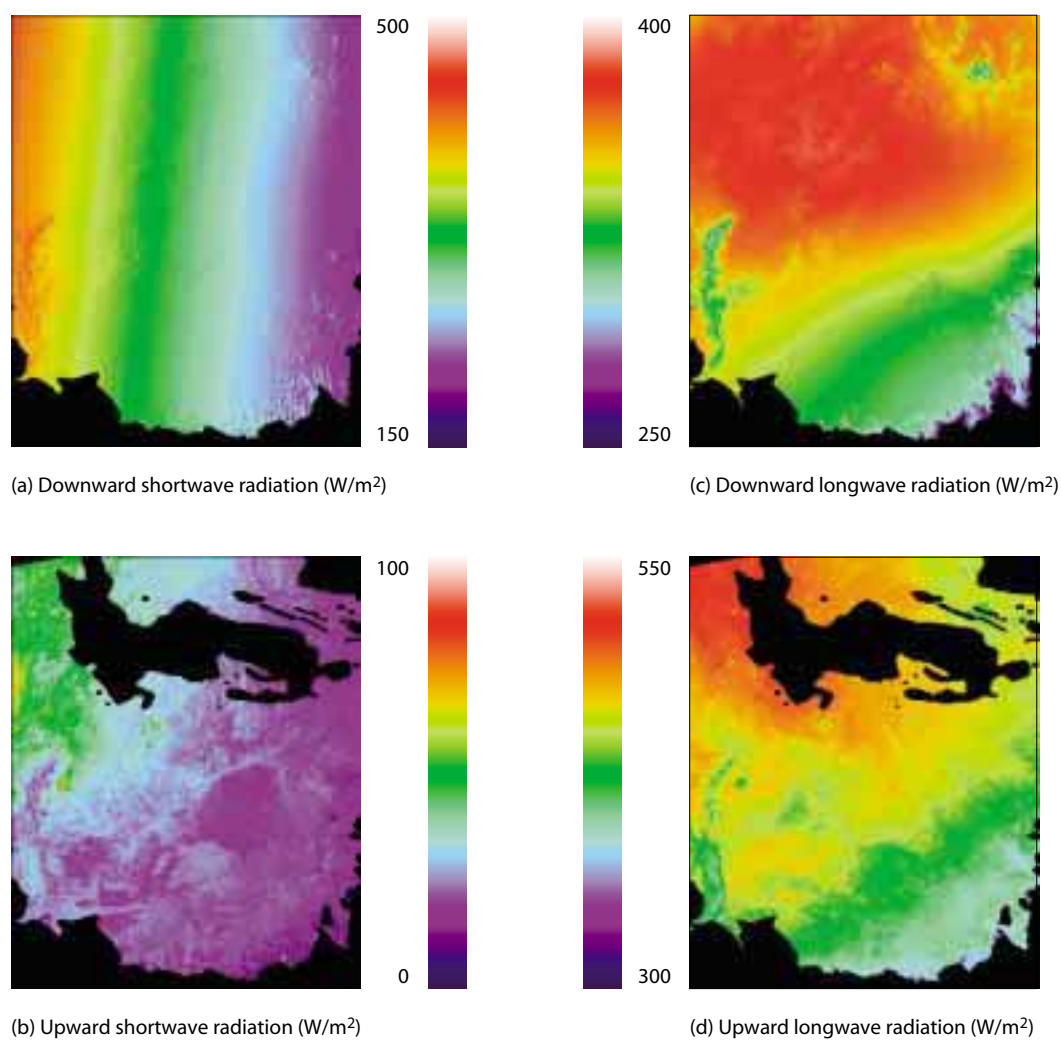


**Figure 6.** Continuous grids of the four radiation components. The figure shows (a)  $R_{s\_down}$  ( $W/m^2$ ); (b)  $R_{s\_up}$  ( $W/m^2$ ); (c)  $R_{l\_down}$  ( $W/m^2$ ) and (d)  $R_{l\_up}$  ( $W/m^2$ ) for the extended normalised difference temperature index (NDTI) area shown in Figure 1 used to calculate  $R_n$ . Variables (b) and (d) require input variables from advanced very high resolution radiometer (AVHRR) data (see Fig. 4). Consequently the areas cloud affected in the AVHRR data (see Fig. 5) are nulled and are shown as black for these variables. Refer to Figure 4 for the development of the four components.

areas where the NDTI has increased between the two dates (Fig. 8c); these areas have probably received scattered rainfall.

Figures 8d and 8e show the AVHRR derived estimates of *VegCov* for spring and summer, respectively. The remnant deep-rooted forests are identified by having a stable *VegCov* between the two seasons. This is especially seen for the remnant river red gum forests along the Murray River. In the

woodlands of the Cobar peneplain, *VegCov* is mainly stable. However, there are some areas on the Cobar peneplain—the blue areas in Fig. 8f—where *VegCov* has increased between the two periods. These areas are associated with an increase in the NDTI (Fig. 8c). This increase in *VegCov* is probably associated with an increase in the amount of grass cover. The grasses have adapted to respond to short-term changes in available moisture and will be observable through the relatively open overstorey canopy (10–20%).

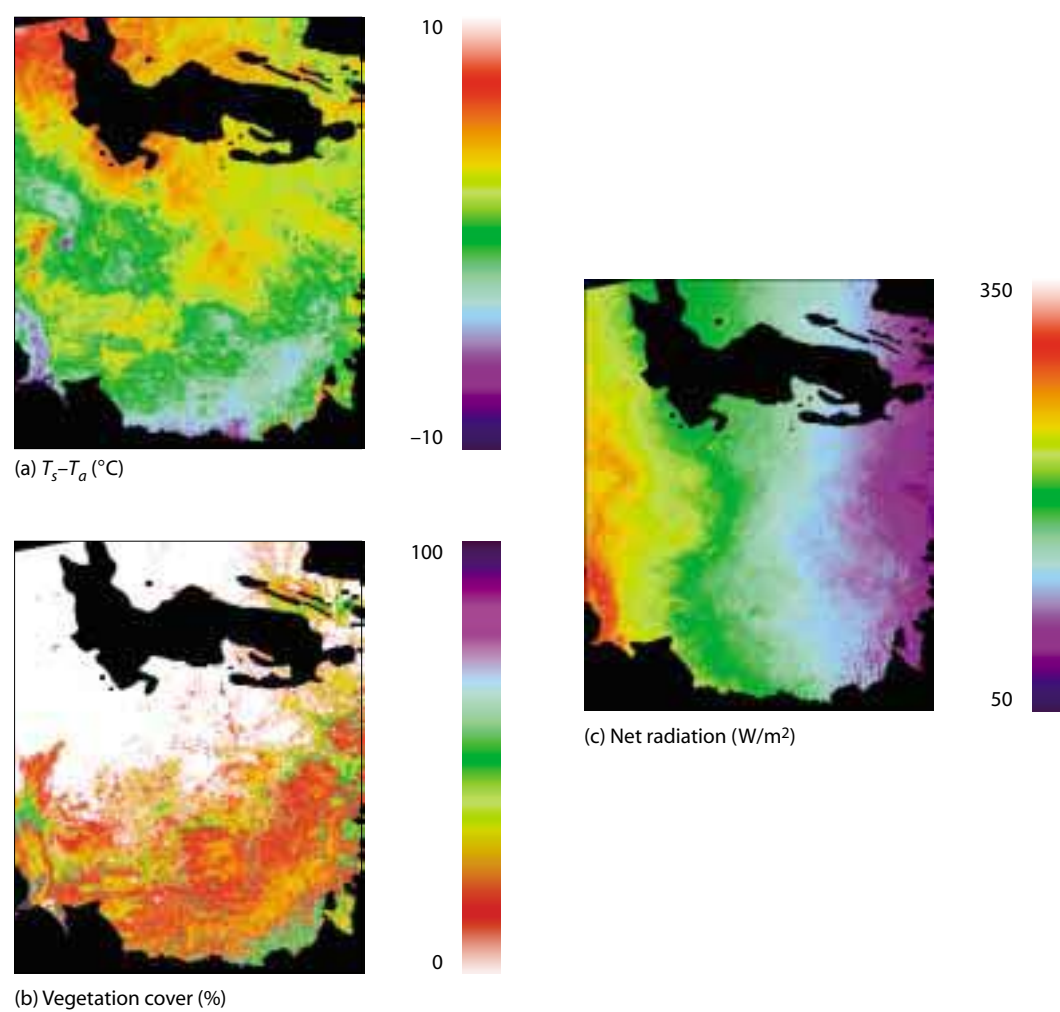


**Figure 7.** Continuous grids of the three covariates. The figure shows (a)  $T_s - T_a$  (°C); (b)  $VegCov$  (%) and (c)  $R_n$  ( $W/m^2$ ) for the extended normalised difference temperature index (NDTI) area shown in Figure 1. All three covariates use advanced very high resolution radiometer (AVHRR) data; consequently areas cloud affected in the AVHRR data (see Fig. 5 and 6) are nulled and are shown as black for each of the covariates.

The changes between the two dates in NDTI (Fig. 8c) and  $VegCov$  (Fig. 8f) are similar, though not identical. For example, along the northeastern border of the two images, there is a large negative change in  $VegCov$  due to harvesting of cereal crops, whereas in this area the NDTI remains fairly constant (it is less than 0.2 for both dates). To assist in regional agricultural management, including drought assessment, the resulting NDTI images and reflective-based images, such as  $VegCov$  or the

normalised difference vegetation index (NDVI), and their interactions, need to be analysed in a spatial-temporal context. If the NDTI is viewed as an indicator of moisture availability, and the NDVI is thought of as an indicator of moisture utilisation, there is an opportunity to separate variability induced by climate from that induced by management (McVicar and Jupp 1998). For example, in cropping or pasture agricultural systems, if the NDTI reduces during a growing

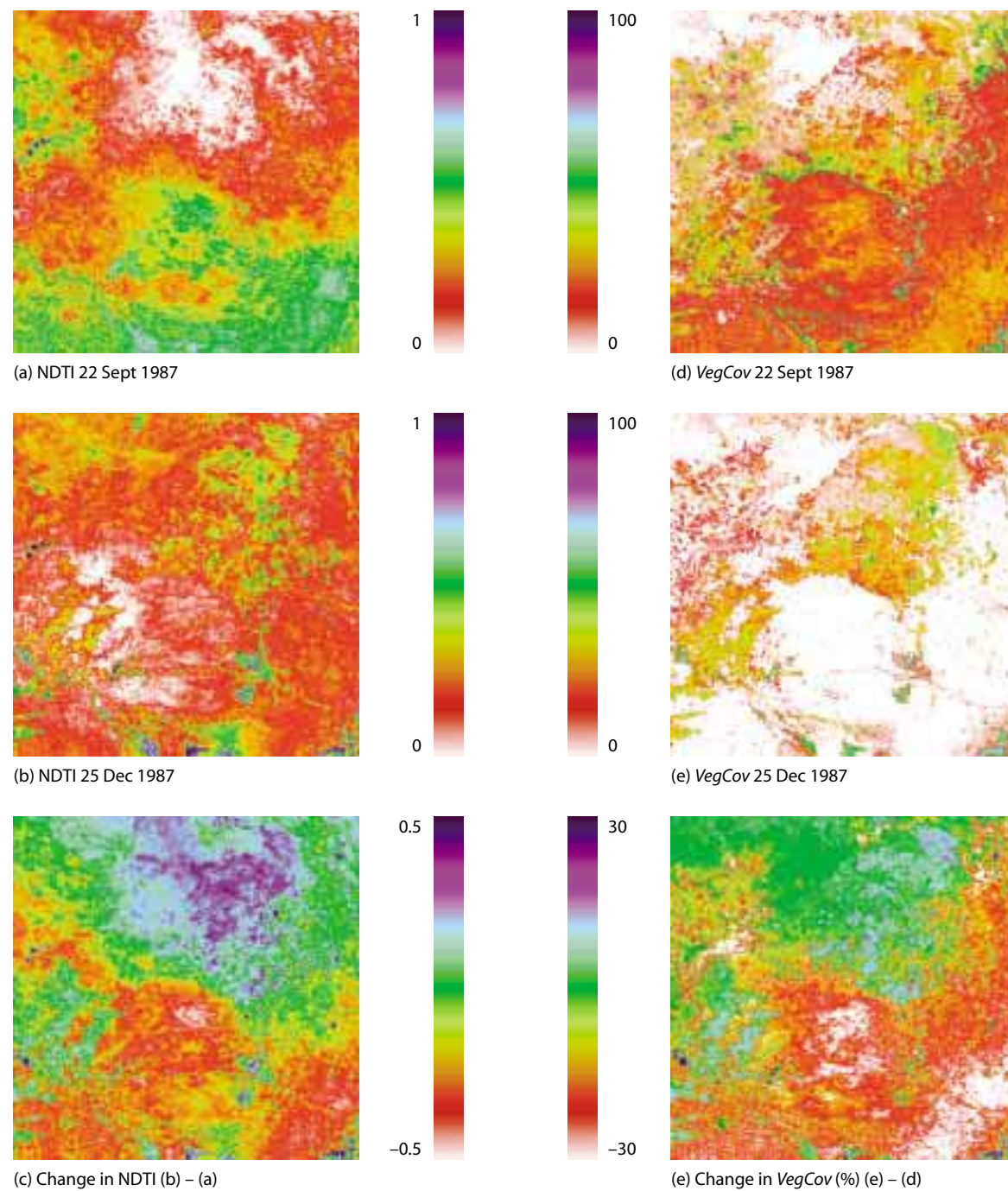


**Figure 8.** Images of the focus NDTI area shown in Figure 1. The figure shows (a) normalised difference temperature index (NDTI) for 22 September 1987; (b) NDTI for 25 December 1987 and (c) the difference of NDTI between these two dates, calculated as (b) - (a). (d) to (f) as for (a) to (c), except that VegCov is shown.

season while the NDVI increases, this would indicate that some of the decrease in moisture availability was due to transpiration. However, there may be cases where the NDTI reduces during the growing season and the NDVI fails to show any response. Such a case could be the result of disease or insect damage early during the crop growing season and the resulting decrease in moisture availability may be attributable only to soil evaporation. During crop growing seasons these interactions may be best analysed by calculating the integrals under a time series of NDTI and NDVI images. The timing of the maximum NDTI and NDVI during crop growth periods would probably have to be included. McVicar and Jupp (2002) provide a formal sensitivity analysis of the variables used in developing the covariates to interpolate the NDTI.

### Conclusions

The NDTI, which can be considered a specific time-of-day version of the CSWI, is calculated using an REBM at the ABM stations where meteorological data are acquired. We have used a CI approach to spatially interpolate the NDTI from these isolated stations to generate a continuous surface in the MDB. Three covariates were required:  $T_s - T_a$ ,  $VegCov$ , and  $R_n$ . They were obtained mainly from AVHRR data and spatial interpolation of selected meteorological variables, with  $R_n$  modelled using an IC approach. We are not advocating CI in preference to IC; the underlying issues determine which is most useful in a given situation. We are advocating, and have presented, a CI method that inherently uses the high spatial density of AVHRR data as the backbone for the spatial interpolation.

The NDTI provides a link into regional water balance modelling that does not require spatial interpolation of daily rainfall. Assessing spatial and temporal interactions between the NDTI and  $VegCov$  or NDVI will provide useful information about regional hydroecological processes, including agricultural management, in the context of Australia's highly variable climate.

### Acknowledgments

This research has been supported in part with contributions by ACIAR and CSIRO Land and Water. We had helpful discussions with Dr Michael Hutchinson (Australian National University, Centre of Resources and Environmental Studies) while conducting this research.

### References

- Borga, M. and Vizzaccaro, A. 1997. On the interpolation of hydrologic variables: formal equivalence of multiquadratic surface fitting and kriging. *Journal of Hydrology*, 195, 160–171.
- Bosma, W.J.P., Marinussen, M.P.J.C. and van der Zee, S.E.A.T.M. 1994. Simulation and areal interpolation of reactive solute transport. *Geoderma*, 62, 217–231.
- Brutsaert, W.H. 1975. On a derivable formula for longwave radiation from clear skies. *Water Resources Research*, 11, 742–744.
- Carter, J., Flood, N., Danaher, T. et al. 1996. Development of a National Drought Alert Strategic Information System. Volume 3. Development of data rasters for model inputs. Final Report to Land and Water Resources Research and Development Corporation, Queensland Department of Primary Industries, 20, Brisbane, 76.
- Choudhury, B.J. 1989. Estimating evaporation and carbon assimilation using infrared temperature data: vistas in modelling. In: Asrar, G., ed., *Theory and Applications of Optical Remote Sensing*. New York, John Wiley and Sons, 628–690.
- Cole, C.V., Paustian, K., Elliott, E.T., Metherell, A.K., Ojima, D.S. and Parton, W.J. 1993. Analysis of agroecosystem carbon pools. *Water, Air and Soil Pollution*, 70, 357–371.
- Colls, K. and Whitaker, R. 1990. *The Australian Weather Book*. Sydney, Child and Associates.
- Courault, D., Lagouarde, J.P. and Aloui, B. 1996. Evaporation for maritime catchment combining a meteorological model with vegetation information and airborne surface temperatures. *Agricultural and Forest Meteorology*, 82, 93–117.
- Cracknell, A.P. 1997. *The Advanced Very High Resolution Radiometer (AVHRR)*. London, Taylor and Francis.
- Dubrule, O. 1983. Two methods with different objectives: splines and kriging. *Mathematical Geology*, 15, 245–257.
- Dubrule, O. 1984. Comparing splines and kriging. *Computers and Geosciences*, 10, 327–338.
- Hutchinson, M.F. 1993. On thin plates splines and kriging. In: Tarter, M.E. and Lock, M.D., eds, *Computing and Science in Statistics*, Vol. 25. University of California, Berkeley: Interface Foundation of North America, 55–62.
- Hutchinson, M.F. 1995. Interpolating mean rainfall using thin plate smoothing splines. *International Journal of Geographic Information Science*, 9, 385–403.
- Hutchinson, M.F. 1997. *ANUSPLIN Version 3.2 User Guide*. Canberra, ANU.

- Hutchinson, M.F. and Gessler, P.E. 1994. Splines—more than just a smooth interpolator. *Geoderma*, 62, 45–67.
- Iqbal, M. 1983. *An Introduction to Solar Radiation*. Vancouver, Academic Press.
- Jackson, R.D., Hatfield, J.L., Reginato, R.J., Idso, S.B. and Pinter Jr., P.J. 1983. Estimation of daily evapotranspiration from one-time-of-day measurements. *Agricultural Water Management*, 7, 351–362.
- Jackson, R.D., Idso, S.B., Reginato, R.J. and Pinter Jr., P.J. 1981. Canopy temperature as a crop water stress indicator. *Water Resources Research*, 17, 1133–1138.
- Jackson, R.D., Pinter Jr., P.J. and Reginato, R.J. 1985. Net radiation calculated from remote multispectral and ground station meteorological data. *Agricultural and Forest Meteorology*, 35, 153–164.
- Jackson, R.D., Reginato, R.J. and Idso, S.B. 1977. Wheat canopy temperature: a practical tool for evaluating water requirements. *Water Resources Research*, 13, 651–656.
- Jupp, D.L.B., Tian, G., McVicar, T.R., Qin, Y. and Fuqin, L. 1998. *Soil Moisture and Drought Monitoring Using Remote Sensing. I: Theoretical Background and Methods*. Canberra, CSIRO Earth Observation Centre, 96.
- Kimball, J.S., Running, S.W. and Nemani, R.R. 1997. An improved method for estimating surface humidity from daily minimum temperature. *Agricultural and Forest Meteorology*, 85, 87–98.
- Kittel, T.G.F., Rosenbloom, N.A., Painter, T.H. and Schimel, D.S. 1995. The VEMAP integrated database for modelling United States ecosystem/vegetation sensitivity to climate change. *Journal of Biogeography*, 22, 857–862.
- Kneizys, F.X., Shettle, E.P., Abreu, L.W., Anderson, G.P., Chetwynd, J.H., Gallery, W.O., Selby, J.E. and Clough, S.A. 1983. *Atmospheric transmittance/radiance: computer code LOWTRAN 6*. Technical Report AFGL-TR-83-0187. Massachusetts, United States Air Force Geophysics Laboratory, 200.
- Kustas, W.P., Jackson, R.D. and Asrar, G. 1989. Estimating surface energy-balance components from remotely sensed data. In: Asrar, G., ed., *Theory and Application of Optical Remote Sensing*. New York, John Wiley and Sons, 604–627.
- Lagouarde, J.-P. 1991. Use of NOAA AVHRR data combined with an agrometeorological model for evaporation mapping. *International Journal of Remote Sensing*, 12, 1853–1864.
- Lam, N.S. 1983. Spatial interpolation methods: a review. *The American Cartographer*, 10, 129–149.
- Laslett, G.M. 1994. Kriging and splines: an empirical comparison of their predictive performance in some applications. *Journal of the American Statistical Association*, 89, 391–409.
- Maher, J.V. and Lee, D.M. 1977. *Upper Air Statistics Australia. Surface to 5 mb 1957 to 1975*. Canberra, Department of Science, Bureau of Meteorology.
- McVicar, T.R. and Jupp, D.L.B. 1998. The current and potential operational uses of remote sensing to aid decisions on drought exceptional circumstances in Australia: a review. *Agricultural Systems*, 57, 399–468.
- McVicar, T.R. and Jupp, D.L.B. 1999a. Estimating one-time-of-day meteorological data from standard daily data as inputs to thermal remote sensing based energy balance models. *Agricultural and Forest Meteorology*, 96, 219–238.
- McVicar, T.R. and Jupp, D.L.B. 1999b. Using AVHRR data and meteorological surfaces to spatially interpolate moisture availability in the Murray–Darling Basin. *Canberra, CSIRO Land and Water*, 45.
- McVicar, T.R. and Jupp, D.L.B. 2002. Using covariates to spatially interpolate moisture availability in the Murray–Darling Basin: a novel use of remotely sensed data. *Remote Sensing of Environment*, 79, 199–212.
- McVicar, T.R., Jupp, D.L.B. and Williams, N.A. 1996a. Relating AVHRR vegetation indices to LANDSAT TM leaf area index estimates. *Canberra, CSIRO Division of Water Resources*, 33.
- McVicar, T.R., Walker, J., Jupp, D.L.B., Pierce, L.L., Byrne, G.T. and Dallwitz, R. 1996b. Relating AVHRR vegetation indices to in situ leaf area index. *Canberra, CSIRO Division of Water Resources*, 54.
- Mitchell, R.M. 1999. Calibration status of the NOAA AVHRR solar reflectance channels: CalWatch Revision 1. Melbourne, CSIRO Atmospheric Research Technical Paper No. 42, 20.
- Moran, M.S., Rahman, A.F., Washburne, J.C., Goodrich, D.C., Weltz, M.A. and Kustas, W.P. 1996. Combining the Penman-Monteith equation with measurements of surface temperature and reflectance to estimate evaporation rates of semi-arid grassland. *Agricultural and Forest Meteorology*, 80, 87–109.
- Nalder, I.A. and Wein, R.W. 1998. Spatial interpolation of climatic Normals: test of a new method in the Canadian boreal forest. *Agricultural and Forest Meteorology*, 92, 211–225.
- Parton, W.J. and Logan, J.A. 1981. A model for diurnal variation in soil and air temperature. *Agricultural Meteorology*, 23, 205–216.
- Pierce, L.L., Walker, J., Dowling, T.I., McVicar, T.R., Hatton, T.J., Running, S.W. and Coughlan, J.C. 1993. Ecohydrological changes in the Murray–Darling Basin. III. A simulation of regional hydrological changes. *Journal of Applied Ecology*, 30, 283–294.
- Prince, S.D., Goetz, S.J., Dubayah, R.O., Czajkowski, K.P. and Thawley, M. 1998. Inference of surface and air temperature, atmospheric precipitable water and vapor pressure deficit using Advanced Very High-Resolution Radiometer satellite observations: comparison with field observations. *Journal of Hydrology*, 212, 230–249.
- Raupach, M.R., Finkele, K., Briggs, P.B., Cleugh, H.A., Coppin, P.A., Leuning, R. and Graetz, R.D. 1997. Water and carbon dynamics of the Australian biosphere. In: Munro, R.K. and Leslie, L.M., eds, *Climate Prediction for Agricultural and Resource Management: Australian Academy of Science Conference, Canberra, 6–8 May 1997*. Canberra, Bureau of Resources Sciences, 211–229.

- Saunders, R.W. 1990. The determination of broad band surface albedo from AVHRR visible and near-infrared radiances. *International Journal of Remote Sensing*, 11, 49–67.
- Seguin, B., Baelz, S., Monget, J.M. and Petit, V. 1982a. Utilisation de la thermographie IR pour l'estimation de l'évaporation régionale. I: Mise au point méthodologique sur le site de la Crau. *Agronomie*, 2, 7–16.
- Seguin, B., Baelz, S., Monget, J.M. and Petit, V. 1982b. Utilisation de la thermographie IR pour l'estimation de l'évaporation régionale. II: Résultats obtenus à partir de données de satellite. *Agronomie*, 2, 113–118.
- Stein, A., Staritsky, I.G., Bouma, J., Van Eijsbergen, A.C. and Bgegt, A.K. 1991. Simulation of moisture deficits and areal interpolation by universal cokriging. *Water Resources Research*, 27, 1963–1973.
- Thornton, P.E., Running, S.W. and White, M.A. 1997. Generating surfaces of daily meteorological variables over large regions of complex terrain. *Journal of Hydrology*, 190, 214–251.
- Wan, Z. and Dozier, J. 1996. A generalized split-window algorithm for retrieving land-surface temperature from space. *IEEE Transactions on Geoscience and Remote Sensing*, 34, 892–905.
- Xie, X. 1991. Estimation of daily evapotranspiration (ET) from one-time-of-day remotely sensed canopy temperature. *Remote Sensing of Environment (China)*, 6, 253–260.
- Zhang, L., Lemeur, R. and Goutorbe, J.P. 1995. A one-layer resistance model for estimating regional evapotranspiration using remote sensing data. *Agricultural and Forest Meteorology*, 77, 241–261.

# 20 Application of a Mean Annual Water Balance Model to the Murray–Darling Basin: Past, Present and Future

Andrew S. Bradford\* and Lu Zhang\*

## Abstract

Catchment water balance is strongly affected by land-use and vegetation characteristics; generally, trees use more water than pasture and crops. As a result, forested catchments yield less stream flow (water yield). In the Murray–Darling Basin (MDB) there are plans to convert large areas of pasture to forestry plantations in the coming decades; a range of commercial and environmental considerations motivates these plans. This chapter describes how a simple water balance model in a geographic information systems (GIS) framework can be used to assess average annual stream flow under different land-use scenarios. The model only requires percentage forest cover of a catchment and mean annual rainfall. The method is well suited for regional-scale assessment of the impacts of change in land use on water yield.

The case study described here is based on average rainfall data for 1980–95, and vegetation cover data under different land-use conditions obtained from the MDB Commission, the Australian Land Information Group (AUSLIG), and CSIRO Forestry and Forest Products. Estimated mean annual catchment water yields agreed well with measured stream flow data for catchments with medium to high rainfall in the MDB but tended to overestimate water yield for low-rainfall catchments. The model showed that clearing native vegetation in the MDB is likely to significantly increase water yield from most of the catchments within the basin. It also predicted that afforestation in the basin may reduce mean annual water yield by up to 40 mm/year.

土地利用方式和植被类别影响流域水量平衡。一般情况下树木比牧草、农作物消耗更多的水分，因而森林覆盖的流域产生的径流较少。出于环境和商业的考虑，计划在未来的几十年里，把默里达令盆地（MDB）的草地大面积改造成林地。本文介绍了一个简单的水量平衡模型在地理信息系统里如何评估不同土地利用方式产生的径流量。该模型只要求输入流域的森林覆盖率

\* CSIRO Land and Water, PO Box 1666, Canberra, ACT 2601, Australia. Email: lu.zhang@csiro.au

Bradford, A.S. and Lu Zhang. 2002. Application of a mean annual water balance model to the Murray–Darling Basin: past, present and future. In: McVicar, T.R., Li Rui, Walker, J., Fitzpatrick, R.W. and Liu Changming (eds), *Regional Water and Soil Assessment for Managing Sustainable Agriculture in China and Australia*, ACIAR Monograph No. 84, 277–290.

和年均降雨量，可用于评估区域范围土地利用变化对产水量的影响。

本项研究基于 1980–1995 年的平均降雨量和不同土地利用下的植被覆盖度。对 MDB 里降雨量高或适中的流域所估算的产水量与实测值吻合很好，但对降水少的流域的估算值偏高。该模型显示原始森林的砍伐很可能使得 MDB 多数流域的产水量大增。它也预测 MDB 完成造林后，年均产水量可减少多达 40 毫米。

LAND use in the Murray–Darling Basin (MDB) has undergone massive changes following European settlement. These changes have significantly modified the hydrological regime of the catchment. The replacement of perennial deep-rooted native vegetation with shallow-rooted vegetation such as perennial grasses, annual grasses and crops has resulted in major changes to catchment-wide evapotranspiration and stream flow (Zhang et al. 1999, 2001; Vertessy and Bessard 1999). These changes to the water balance and vegetation have in turn had major effects on the salt balance and stream salinity within the catchments (Jolly et al. 1997, 2001; Natural Heritage Trust 2001).

There are plans to convert large areas of pasture in the MDB to forestry plantations in the coming decades (e.g. Department of Primary Industries and Energy 1997). A range of commercial and environmental considerations, including the management of dryland salinity, motivates these plans. As this paper demonstrates, the spatial distribution of plantations within catchments greatly influences the resulting change in hydrology.

A number of studies have shown that evapotranspiration from a forested catchment is generally greater than that from a grassed catchment with the same climatic conditions (Holmes and Sinclair 1986; Turner 1991; Zhang et al. 2001). Thus,

land-use management strategies will impact on catchment water balance. The key factors controlling evapotranspiration include rainfall interception, net radiation, advection, turbulent transport, leaf area and plant available water capacity. The relative importance of these processes is likely to depend on climate, soil and vegetation conditions. Zhang et al. (2001) have developed a simple water balance model to assess impacts of land-use changes, which requires only vegetation, annual total streamflow and rainfall data. The model agreed with independent water balance estimates from more than 250 catchments. This paper describes how the model was used within a GIS framework to estimate catchment water yield under different vegetation conditions in the MDB.

### Mean Annual Water Balance Model

Zhang et al. (2001) developed the catchment balance model used in this study, based on an examination of annual rainfall and evapotranspiration relationships. It is assumed that, under very dry conditions, potential evapotranspiration exceeds precipitation and actual evapotranspiration equals precipitation; under very wet conditions, water availability exceeds potential evapotranspiration and actual evapotranspiration equals potential evapotranspiration. Based on these assumptions, mean annual evapotranspiration (*ET*)

can be calculated from mean annual rainfall ( $P$ ) and potential evapotranspiration ( $E_0$ ):

$$ET = P \left\{ \frac{1 + w \left( \frac{E_0}{P} \right)}{1 + w \left( \frac{E_0}{P} \right) + \left( \frac{E_0}{P} \right)^{-1}} \right\} \quad (1)$$

where  $w$  is the plant available water coefficient.

Following Eagleson (1982), we assumed that mean annual evapotranspiration from a catchment is the sum of the evapotranspiration from herbaceous vegetation ( $ET_{nonforest}$ ) (including soil evaporation) and from forest ( $ET_{forest}$ ), weighted linearly according to their percentage areas. The general equation can be expressed as:

$$ET_{total} = f \times ET_{forest} + (1-f) \times ET_{nonforest} \quad (2)$$

where  $f$  is percentage area of a catchment forested. The nonforest part of a catchment could be further divided into woodland and grasses if such data were available.

To simplify the calculation, the parameters in Equation 1 were established for forested and nonforested catchments:

$$ET_{forest} = \left\{ \frac{1 + 2.0 \times \frac{1410}{P}}{1 + 2.0 \times \frac{1410}{P} + \frac{P}{1410}} \right\} \times P \quad (3)$$

$$ET_{nonforest} = \left\{ \frac{1 + 0.5 \times \frac{1100}{P}}{1 + 0.5 \times \frac{1100}{P} + \frac{P}{1100}} \right\} \times P \quad (4)$$

These relationships are shown in Figure 1, together with observed evapotranspiration from the catchments listed in Zhang et al. (1999). The size of these catchments varied from less than 1 km<sup>2</sup> to 6 × 10<sup>5</sup> km<sup>2</sup>, and they span a variety of climates. The vegetation varies from same-aged plantation trees to native woodlands, open forest, rainforest,

eucalypt forest, native and managed grassland, and agricultural cropping.

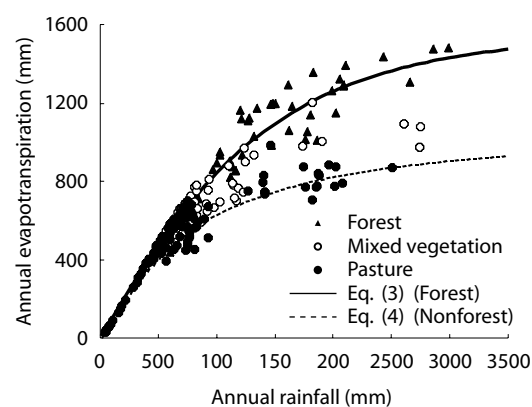


**Figure 1.** Relationships between annual evapotranspiration and rainfall (Zhang et al. 1999).

It is clear from Figure 1 that most of the forested catchments plot within the upper curve described by Equation 3, nonforested catchments plot around the lower curve described by Equation 4 and mixed vegetation catchments plot in the middle. The relationships described by Equations 3 and 4 are very similar to the empirical curves proposed by Holmes and Sinclair (1986) for catchments in Victoria.

Assuming that the change in catchment water storage over a long period is zero, catchment average water yield is calculated as the difference between long-term average rainfall and evapotranspiration. Figure 2 shows the resulting relationship between water yield and rainfall.

## Case Studies

Estimation of the impact of land-use changes on catchment water yield for the main drainage divisions within the MDB (Fig. 3) required spatial data sets of rainfall, catchment boundaries and forest cover. We considered three land-use scenarios — pre-European vegetation, current vegetation and potential future forest plantation. We describe the sourcing and manipulation of these data, which were obtained from various government agencies and

captured for different purposes, and the methods and procedures used to estimate catchment area rainfall and percentage forest cover from these data.

We characterised forest cover for a given catchment using pre-European, current and potential future plantation forest areas of different temporal and spatial scales. Problems associated with initial vegetation classification were overcome by reclassifying the data into two main categories. This process allowed us to compare past, present and potential future vegetation coverage. We wrote ArcInfo programs (ARC macro languages; AMLs) to automate the resampling, the reprojecting of data and the model itself.

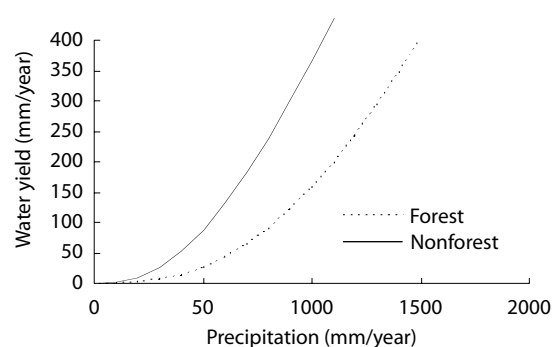


**Figure 2.** Relationship between catchment water yield and rainfall.

### Rainfall surface

Monthly interpolated rainfall surfaces were combined to give a mean annual rainfall surface for 1980–95. Each grid cell is  $0.05^\circ$ , or approximately  $25 \text{ km}^2$  (Jolly et al. 1997). The grid point analysis technique used to derive surfaces provides an objective average for each grid cell and useful estimates of rainfall in data-sparse areas. However, in data-rich areas such as southeast Australia or in regions with a strong rainfall gradient, ‘data smoothing’ will occur, resulting in values at point locations which may differ slightly from the exact rainfall recorded. Figure 4 shows the range and spatial distribution of long-term mean annual rainfall across the MDB.

### Catchment boundaries

This project is based on 26 drainage divisions of the MDB with catchments ranging in size from  $700 \text{ km}^2$  to  $130,000 \text{ km}^2$  (Fig. 5). These catchment boundaries were taken from a previous salt load study (Jolly et al. 1997), which delineated catchments using a watershed analysis. Table 1 lists catchment areas and mean annual rainfall.

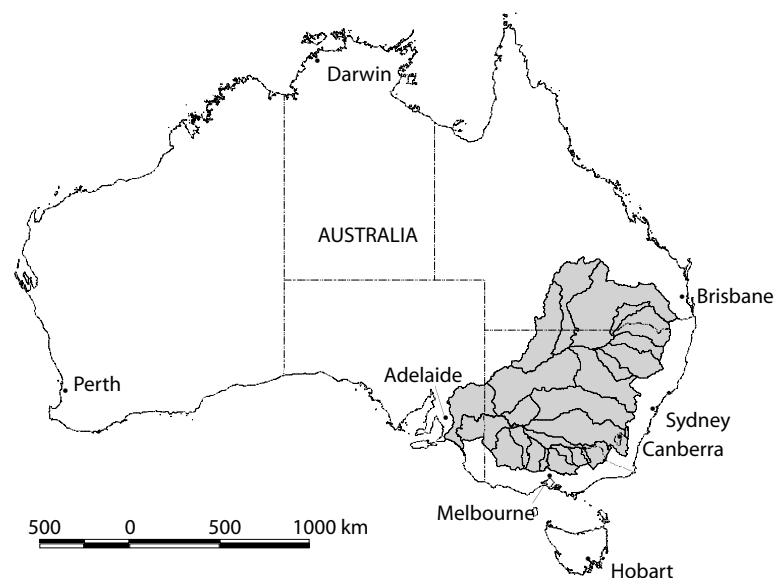


**Figure 3.** Location of the Murray–Darling Basin (grey area).

### M305 vegetation dataset

The m305 multistructured vegetation data set contains attributes characterising land cover and vegetation (Ritman 1995). This study focuses on the woody vegetation component of the land cover

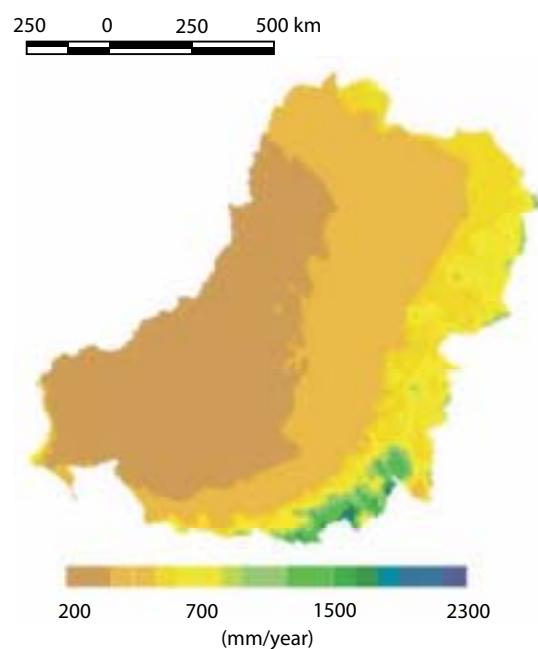


**Figure 4.** Distribution of mean annual rainfall throughout the Murray–Darling Basin.

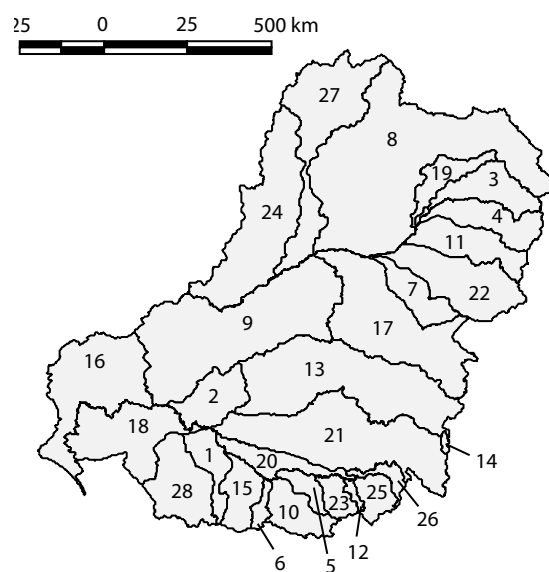


**Figure 5.** Location of the main drainage divisions within the Murray–Darling Basin (Jolly et al. 1997).

class. The woody vegetation was mapped from Landsat Thematic mapper (TM) imagery at a 30 m ground resolution with six bands per scene from as many cloud-free days as possible. Between late 1989 and 1991, images were chosen to maximise the

**Table 1.** Catchment area and mean annual rainfall for the 26 catchments within the Murray–Darling Basin.

ID No.	Catchments	Mean annual rainfall (mm)	Area (km <sup>2</sup> )
1	Warrego River	408	62,940
2	Condamine-Culgoa	482	162,597
3	Paroo River	281	73,953
4	Moonie River	519	14,342
5	Border Rivers	621	48,041
6	Gwydir	620	26,586
7	Namoi	617	42,000
8	Macquarie	523	74,792
9	Darling River	295	112,832
10	Castlereagh River	537	17,423
11	Lower Murray	281	58,274
12	Lachlan River	470	90,880
13	Benanee	291	21,345
14	Murrumbidgee River	556	81,643
15	Mallee	301	41,488
16	Avoca River	365	14,201
17	Lake George	701	942
18	Wimmera-Avon	405	30,367
19	Murray–Riverina	395	15,039
20	Loddon River	461	15,655
21	Upper Murray River	1,105	15,342
22	Broken River	593	7,099
23	Ovens River	992	7,981
24	Goulburn	829	16,857
25	Campaspe River	590	4,048
26	Kiewa	1,190	1,912

number of cloud-free days. The imagery was initially resampled from 30 m to 25 m. An unsupervised classification into 100 classes was performed on the imagery to derive the woody vegetation. Each map sheet required resampling from 25 m to 250 m because the final mosaic grid would otherwise have been too data intensive. The resulting woody vegetation layer was filtered to minimum clusters of 0.25 ha. Woody vegetation is represented as land cover class 7 and defined as vegetation that has 20% crown cover and is over 2 m in height. A consolidated grid surface was created from the 472 1:100,000 scale map sheets and each map sheet was reprojected from the Australian map grid (AMG) to latitudes and longitudes. New South Wales, Queensland and Victoria had three AMG zones and South Australia had one. The Albers equal area coordinate system (Ritman 1995) is recommended for the basin-wide area statements. However, the model framework discussed does not require any absolute measured areas; it needs only the proportion of catchment under forest.

#### Carnahan pre-European vegetation data

The Carnahan pre-European settlement vegetation mapping is stored as a 1:5,000,000 scale map covering all of Australia in a geographic projection. The polygon coverage is based on the AUSLIG present vegetation that was created from Landsat multispectral scanner (MSS) imagery at the 1:1,000,000 scale between 1980 and 1985. We derived the pre-European vegetation by modifying current vegetation polygons using historical information, including the diaries of explorers and camel drivers, and soil and vegetation reports that date to the latter part of the nineteenth century. The Carnahan source data are an estimation of what vegetation could have existed prior to European settlement.

The classification attributes of the 1980–85 data were carried across to the Carnahan data set. It was therefore possible to compare the AUSLIG base vegetation data set (1980–85 MSS data) and m305 vegetation data set. Although there are large

differences between the spatial scale of the current m305 and the Carnahan pre-European vegetation data sets, the Carnahan data is the best that is available at this time. From a temporal perspective, the AUSLIG current vegetation coverage (1980–85) and the m305 vegetation data set (1989–91) are comparable. The comparison was undertaken to set classification rules for the polygon attributes when compared to the tree areas of the m305. Finally, these rules were transferred to the Carnahan pre-European data set to model a possible scenario. Three attribute fields were analysed from the current AUSLIG vegetation data set: ‘tallest stratum’, ‘density’ and ‘species growth form’.

Vegetation density foliage cover is expressed in terms of the proportion of the ground that is shaded by the tallest stratum at midday (McDonald et al. 1990). The AUSLIG vegetation data set expresses this in four classes, from < 10% to > 70%. Class 1 is 0–10% (crowns well separated), class 2 is 10–30% (crowns clearly separated), class 3 is 30–70% (crowns touching or slightly separated) and class 4 is 70% or greater (crowns touching to overlapping). The density of foliage cover of the lower stratum is not recorded in the code.

We chose classes 2 to 4 from the foliage cover attribute field. Classes 2 and 3 contain the greatest source of potential error of commission because they cover a broad range of vegetation types and are therefore difficult to compare with the 20% crown cover of the m305 data set. Foliage density was the first class to be investigated, so class 2 was included on the grounds that vegetation height and species would sufficiently discriminate the tree areas for comparison with the m305 vegetation cover. Moreover, when class 2 was omitted, significant areas that were considered ‘tree’ by the m305 data set were not accounted for. In short, more class 2 was considered as ‘tree’ than as ‘no tree’ when comparing to the woody m305 data set.

Species growth form is primarily classified into three vegetation groups: grasses, shrubs and trees.

These three groups are further broken down by vegetation height. Grasses and shrubs less than 2 m high were considered to be nonwoody vegetation and were excluded from the classification because they did not fit the m305 woody vegetation criteria. Table 2 shows which classes were chosen from the AUSLIG present vegetation classes and used in the analysis of the Carnahan pre-European vegetation. Figure 6 shows how the comparison is represented spatially between the two vegetation data sets based on the rules in Table 2.

The tallest stratum is defined as the uppermost stratum in which most of the incoming solar radiation is intercepted (McDonald et al. 1990).

**Table 2.** The rules used in the vegetation classification of forest for the AUSLIG vegetation data sets.

Rule	Class	Vegetation type
1	Tallest stratum (TS_SD)	Eucalyptus Conifers
2	Density (TS_D)	10–30% 30–70% 70% >
3	Species growth form (GF)	Low trees < 10 m (L) Medium trees 10–30 m (M) Tall shrubs > 2 m (S) Tall trees > 30 m (T)

When the data were tested, the tallest stratum data field was tested against the m305 vegetation data set. Conifers and eucalyptus were found to have the best correlation with the woody component of the m305 data set.

We generated a new grid by merging the m305 vegetation data set and the AUSLIG ‘present vegetation’ cover. With such estimations, there is a chance that errors of omission from the original data will occur. The correlation matrix shown in Table 3 illustrates an 8% error of omission where m305 has forest present and AUSLIG ‘present vegetation’ does not, and an 8% error of commission where m305 has no forest present and AUSLIG ‘present vegetation’ shows forest. This comparison is encouraging, particularly because the m305 vegetation data set was generated from a classification on a cell-by-cell basis and the AUSLIG vegetation is a polygon data set of grouped like-vegetation classes.

**Table 3.** Correlation matrix of the m305 vegetation data set and the AUSLIG present vegetation data set with regard to tree and no-tree areas.

		AUSLIG present	
		No tree	Tree
m305	No tree	72%	8%
	Tree	8%	12%

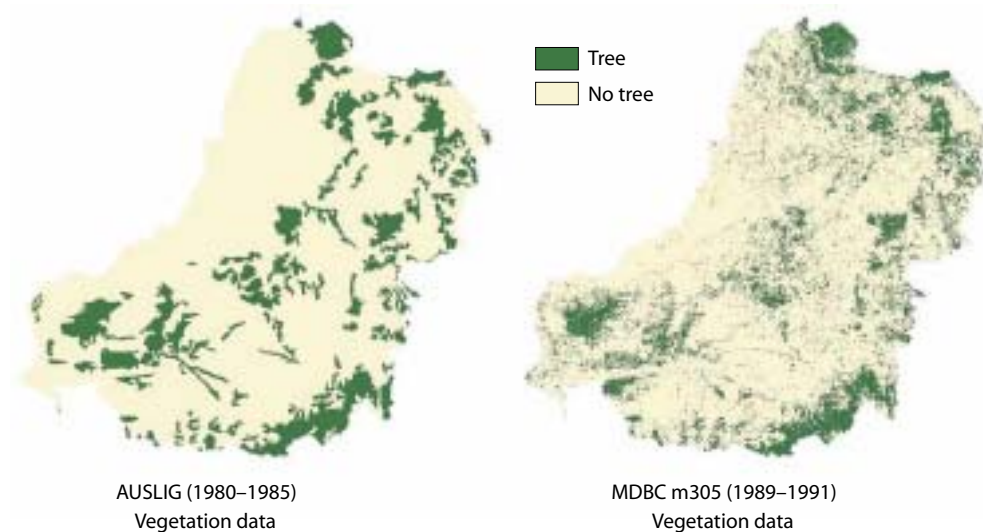


**Figure 6.** M305 vegetation and AUSLIG present vegetation shown as tree and no tree.

The rules described in Table 2 were applied to the Carnahan vegetation data set. Figure 7 shows the final classified Carnahan pre-European vegetation data set of tree and no tree.

#### Potential afforestation data

The potential afforestation data set was designed to predict areas suitable for hardwood plantation timbers across Australia. The main source data set used in this analysis considered the environmental factors that favour plantation hardwoods, including precipitation, topography, soils, pests and diseases (Booth and Jovanovic 1991). The potential forest plantation data set involved only the transformation of points to grids and reprojection from AMG coordinates to geographic coordinates. The cell size was  $0.05^\circ$  in latitude and longitude (approximately  $25 \text{ km}^2$ ). The resolution was chosen on the basis of the complexity of the analysis, storage requirements and the similarly coarse resolution of other data sets used in the suitability analysis. The attributes of the point data set were carried across to the grid surface. All areas suitable for plantation (i.e. low, medium or high suitability) were considered as the potential afforestation areas (Fig. 8); this represents the total areas currently under forest and the areas that can be reforested.



**Figure 7.** Classified tree/no tree data from the Carnahan pre-European vegetation data set.

## Results and Discussion

### Catchment water yield under current vegetation conditions

The m305 woody vegetation data set of the MDB provides a coherent data set across the basin. Evapotranspiration from each catchment was calculated by combining the vegetation data with the annual rainfall data. In order to compare the results with stream flow measurements, catchment water yield was obtained by subtracting evapotranspiration from rainfall. Figure 9 shows estimates of the catchment water yield in relation to rainfall for all 26 catchments. The calculated catchment-scale water yields ranged from 14 to 335 mm/year, and were within the mean annual water yield relationships defined by Equations 3 and 4. It is clear from Figure 9 that the difference in catchment water yield between forested and nonforested catchments is small (up to 700 mm/year). However, the difference becomes larger as rainfall increases, suggesting that changes in vegetation cover will have a relatively large impact on catchment water yield in high-rainfall areas. This is an important relationship because areas of high rainfall are of great importance for water supply and stream salinity dilution.

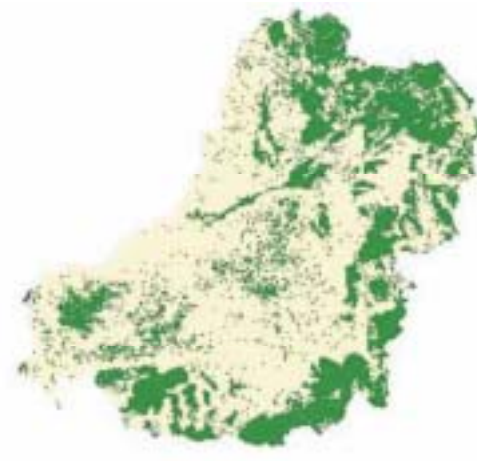


**Figure 8.** Potential plantation areas and the m305 vegetation data set combined.

Figure 10 shows the modelled catchment-scale water yields compared with long-term stream flow measurements reported by the Department of Natural Resources (1976) and Jolly et al. (1997). The best-fit slope through the origin was 1.03 and the model estimates were statistically consistent with the measurements. However, there were relatively large scatters in the results, and the model tended to overestimate water yield in low-rainfall catchments. When expressed as a percentage of mean annual rainfall, the error in the estimated water yield ranged between 16% and -5%.

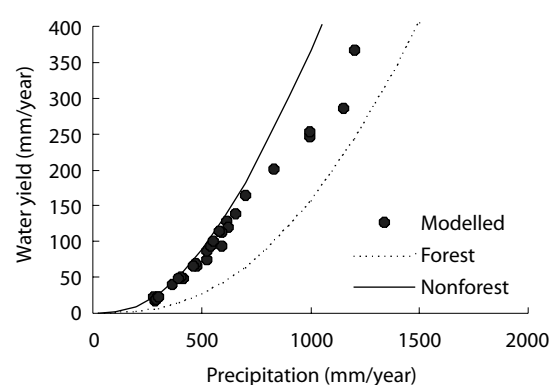


**Figure 9.** Estimates of water yield under current vegetation cover for the 26 catchments in the Murray–Darling Basin.

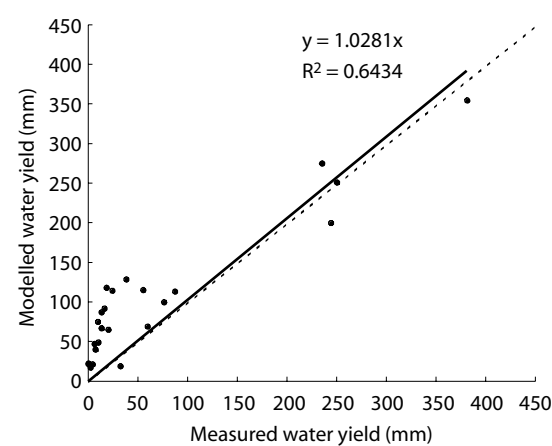


**Figure 10.** Comparison of calculated and measured catchment water yield for the major catchments in the Murray–Darling Basin. The dashed line is the 1:1 line and the solid line the regression line.

A number of factors could have contributed to the errors in the results. First, estimates of percentage forest cover could affect evapotranspiration modelled by Equation 3. In low rainfall catchments, average percentage forest cover was a small fraction of the total catchment area and some open woodlands were classified as nonforests. This would result in underestimates of evapotranspiration or overestimates of water yield. Second, rainfall distribution could also affect estimates of evapotranspiration and hence water yield. By using mean annual rainfall, the model is likely to underestimate evapotranspiration in catchments with summer dominant rainfall. Examination of the results shows that the model underestimated evapotranspiration in catchments such as Condamine–Culgoa, Moonie and Namoi. Rainfall in these catchments is summer dominant, with 35% of rain falling from December to February. The results from the model can be improved by introducing a seasonality index; this will be investigated in a future study. Finally, diversion of water occurs in many of the catchments in the MDB and it is extremely difficult to account for the effects of diversions on stream flow measurements. This shortcoming will also be investigated in a future study.

The estimated catchment water yields show significant spatial variation (Fig. 11). In the Benanee and Lower Murray catchments, mean annual water yield was less than 20 mm per year; in the eastern catchments, such as the Ovens and Upper Murray catchments, mean annual water yield was above 250 mm per year.

#### Catchment water yield under pre-European vegetation conditions

We used the model to try to evaluate the effect of clearing native vegetation on mean annual water yield based on current and pre-European vegetation data. Catchment water yields under pre-European vegetation conditions were calculated from the Carnahan pre-European vegetation data

set. We assumed that mean annual precipitation during that time was the same as the mean annual rainfall for the period 1980–95. The results are shown in Figure 12. The large-scale AUSLIG data set estimated average forest cover as 69% before European settlement. This value is significantly higher than the current forest cover of 20%, taken from the m305 woody vegetation data set. Table 4 illustrates the loss in forest cover for each catchment, using the above data set. As a result of loss of vegetation, estimated water yield under pre-

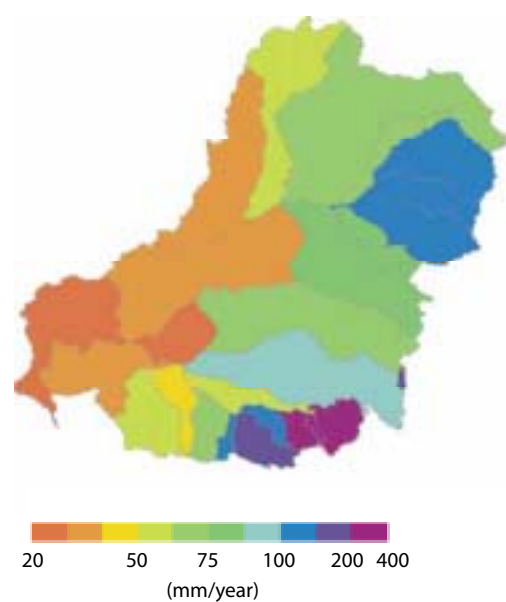


**Figure 11.** Predicted mean annual water yield distribution across the Murray–Darling Basin under current vegetation cover.

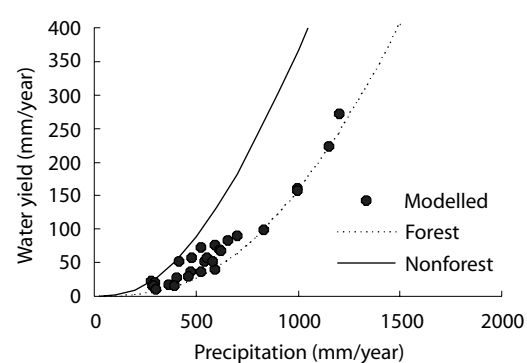


**Figure 12.** Catchment water yield under pre-European vegetation conditions.

European vegetation conditions was consistently lower than that under current vegetation conditions (Figs 9 and 12). Water yield increased from 0 to 80 mm/year with the most significant changes occurring in the catchments east of the Darling River (Fig. 13). On average, estimated water yield in the MDB has increased from 46 to 69 mm/year.

These results are indicative only and may not represent the actual water yield under pre-European vegetation conditions. However, they provide some estimates of likely changes in catchment water yields resulting from the clearing of native vegetation. There are no gauged stream flow data under pre-European vegetation conditions; the only descriptive information available is written records left by explorers, travellers and settlers. Their view of streams, based on European experience, may be subjective but it provides a qualitative picture of the streams under pre-European conditions. For example, in the Upper Murrumbidgee, 'It seems the small streams of the catchment were swampy at the time of European exploration, and many were chains-of-ponds.' (Starr et al. 1999). This information suggests that stream flow under pre-European vegetation conditions would be less than the current stream flow.

### Impact of potential afforestation on catchment water yield

Increased groundwater recharge has been identified as a major factor causing dryland salinity in the MDB. A number of land management options have been considered to reduce groundwater recharge; one is forest plantations. Forest can use more water than pasture and hence reduce recharge to groundwater systems. Afforestation can also affect water yield (Vertessy and Bessard 1999). A forest plantation capability scenario was mapped for the purpose of investigating potential commercially viable plantation areas (Booth and Jovanovic 1991). Plantation areas in the MDB were calculated from numerous factors, one of which was the absence of existing forests, which meant that a future scenario of

forested areas could only be estimated by combining the potential afforested areas with the m305 vegetation data set. The vegetation scenario was based on the potential implementation of eucalyptus, acacia and pine as commercial plantations. Table 5 lists the criteria on which each species was chosen.

Table 4 illustrates the potential rise in forest cover given full adoption of potential plantation areas. There is opportunity for a significant increase in plantation area in some catchments—such as Condamine–Culgoa Rivers, Moonie River, Border Rivers, Goulburn River, and Wimmera–Avon

**Table 4.** Current forest cover compared to pre-European forest cover and potential plantation forest cover for the 26 catchments of the Murray–Darling Basin.

Catchment	Current forest (%)	Pre-European forest (%)	Decrease (%)	Potential plantation (%)	Increase (%)
Warrego River	21	21	0	38	17
Condamine-Culgoa	25	40	15	55	30
Paroo River	4	4	0	7	3
Moonie River	31	34	2	70	36
Border Rivers	29	64	35	49	19
Gwydir	14	75	61	32	18
Namoi	24	78	54	38	14
Macquarie	16	88	72	29	13
Darling River	13	23	10	13	0
Castlereagh	16	72	56	37	21
Lower Murray	28	39	12	29	1
Lachlan River	14	71	57	21	7
Benanee	27	48	21	27	0
Murrumbidgee	16	70	54	26	10
Mallee	23	80	57	24	1
Avoca River	8	76	69	46	39
Lake George	17	76	59	36	19
Wimmera–Avon	13	66	53	53	40
Murray–Riverina	10	92	83	14	4
Loddon River	16	84	68	46	30
Upper Murray	69	99	30	85	16
Broken River	18	100	82	24	7
Ovens River	54	99	45	65	11
Goulburn	36	100	64	61	25
Campaspe	15	86	71	20	6
Kiewa	56	89	33	69	13

Rivers. Such plantations would increase catchment evapotranspiration and hence reduce water yield (Fig. 14).

Figure 15 shows changes in water yield from the current vegetation and the potential plantation for all catchments. The southeastern catchments of the MDB would have a low to moderate change in water yield as a result of the afforestation; the catchments at the headwaters of the Murray River, where annual rainfall is relatively high, would experience a reduction in water yield of 20–40 mm/year. Minimal changes in water yield would occur in other catchments that are not considered to be suited for sustainable plantations. Although these changes are not as dramatic as those under the pre-European vegetation conditions, they may have significant impacts on water supply and salinity

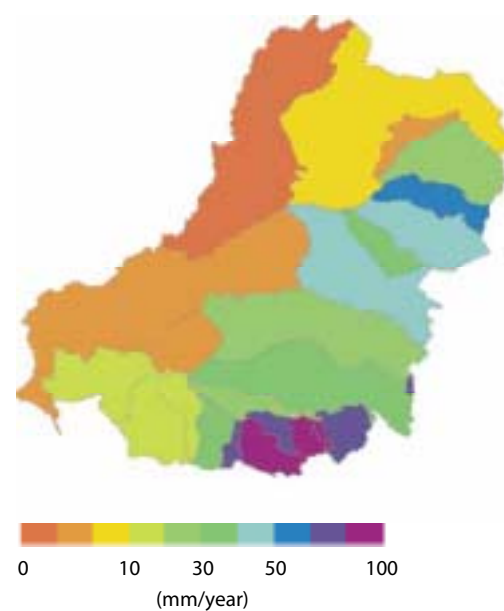


**Figure 13.** Increase in water yield from pre-European vegetation cover to current vegetation cover.

**Table 5.** Criteria for the selection of suitable forest plantation areas by species.

Species	Mean rainfall (mm/year)	Rainfall regime	Dry season length (months)	Mean max temp (°C)	Mean min temp (°C)	Mean annual temp (°C)	Soil
<i>Eucalyptus globulus</i>	600–1500	Winter/ uniform	0–5	19–30	2–12	9–18	Fertile loams
<i>Eucalyptus grandis</i>	800–2500	Summer	0–5	25–34	3–16	14–25	Alluvial, volcanic
<i>Eucalyptus nitens</i>	750–1500	All	0–4	20–28	–3–5	7–14	Granite, basalt
<i>Eucalyptus pilularis</i>	750–2000	Summer/ uniform	0–2	22–31	5–12	15–22	Sandy loams
<i>Eucalyptus regnans</i>	900–2000	Winter/ uniform	0–3	17–27	–2–6	7–14	Deep moist
<i>Eucalyptus saligna</i>	700–1800	Uniform/ summer	0–5	22–32	1–14	14–21	Sandy loams
<i>Acacia mangium</i>	1150–3700	Summer	0–5	29–33	12–30	23–28	Acid volcanic
<i>Acacia mearnsii</i>	800–1600	Uniform				16–20	Sands, loams
<i>Acacia melanoxylon</i>	480–2950			19–34	–3–16	9–25	Volcanic soils
<i>Pinus elliotii</i>	750–1700	Summer	0–5	26.5–31	5–12.5	18–23	Phosphorus soils
<i>Pinus radiata</i>	650–1600	Winter/ uniform	0–4	20–30	–2–12	11–18	Mixed

Source: Booth and Jovanovic (1991).

control. Vertessy and Bessard (1999) applied a similar relationship—developed by Holmes and Sinclair (1986)—to the Murrumbidgee catchment and concluded that afforestation in the catchment may significantly reduce mean annual runoff. Reduction in water yield not only imposes costs on users downstream but also affects stream salinity dilution. An important issue is the tradeoff between recharge control and water yield reduction, as these

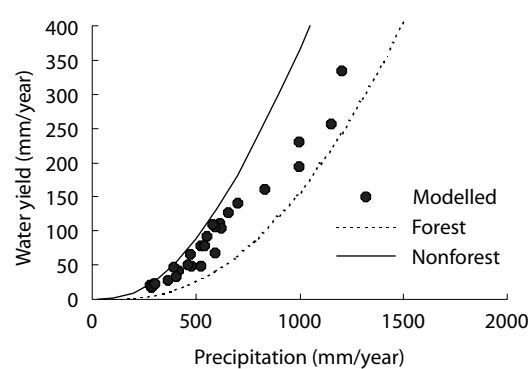


**Figure 14.** Estimates of water yield under the potential afforestation scenario.

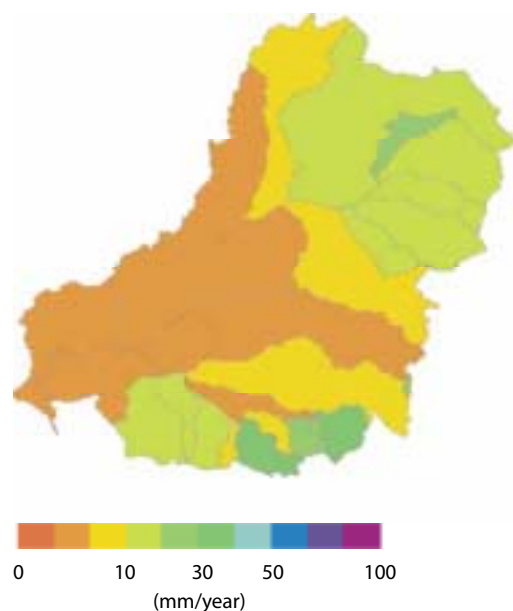


**Figure 15.** Change in water yield from current vegetation to potential afforested areas.

are likely to vary with rainfall. Such information can help us to make responsible management decisions about land-use changes in the MDB.

## Conclusions

This chapter demonstrates how the simple water balance model developed by Zhang et al. (2001) can be used in a GIS framework to estimate the impacts of vegetation changes on mean annual average water yield in a catchment. The model considers the effects of available energy and water on evapotranspiration and requires only mean annual rainfall and vegetation-cover measurements. Comparison between predicted and measured water yield under current land-use conditions agreed reasonably well for catchments with high rainfall; however, the model tended to overestimate water yield for low-rainfall catchments. The model may be improved by introducing a rainfall seasonality index and this will be further investigated. To evaluate the impact of clearing of the native vegetation in the MDB, we estimated water yield under pre-European vegetation conditions. The results showed significant reduction in water yield from most of the catchments within the basin. Although there are no direct stream flow data with which to compare these estimates, some descriptive information seems to indicate that there would be less runoff under pre-European vegetation conditions from the basin. We also attempted to evaluate the impact of afforestation on future catchment water yields and our analysis suggests that broad-scale afforestation in the basin may reduce mean annual water yield by up to 40 mm/year. This may be desirable from a point of view of recharge reduction but its impact on downstream water supply needs to be considered.

Large-scale afforestation affects not only mean annual stream flow, but also flow regime. Results from some paired catchment studies have shown significant changes in flow regime following clearing of forests (Burch et al. 1987; Jones 2000). Further studies are necessary to model these hydrological responses in large catchments.

## Acknowledgments

This study was supported by a Land and Water Australia through the National Dryland Salinity Program grant 'Predicting the Combined Environmental Impact of Catchment Management Regimes on Dryland Salinity' (CLW29), the Cooperative Research Centre for Catchment Hydrology and ACIAR (LWR 1/95/07). We gratefully acknowledge the Murray–Darling Basin Commission, the Australian Land and Information Group and the CSIRO Division of Forestry for providing data for this study. Dr Kim Ritman, Environmental Systems Research Institute (ESRI) Defence, Dr Tim McVicar and Susan Cuddy, CSIRO Land and Water assisted with review and structure of this chapter and we thank them for their contribution.

## References

- Booth, T.H. and Jovanovic, T. 1991. Identification of Land Capable of Private Plantation Development. Report of the National Plantations Advisory Committee. Canberra, Department of Primary Industries and Energy, Appendix B, 1–86.
- Burch, G.J., Bath, R.K., Moore, I.D. and O'Loughlin, E.M. 1987. Comparative hydrological behaviour of forested and cleared catchments in southeastern Australia. *Journal of Hydrology*, 90, 19–42.
- Department of Natural Resources 1976. Review of Australia's Water Resources (1975). Canberra, Australian Government Publishing Service.
- Department of Primary Industries and Energy (DPIE) 1997. The 2020 Vision Statement. Canberra, ACT, DPIE.
- Eagleson, P.S. 1982. Ecological optimality in water-limited natural soil vegetation systems. 1. Theory and Hypothesis. *Water Resources Research*, 18, 325–340.
- Holmes, J.W. and Sinclair, J.A. 1986. Water Yield from Some Afforested Catchments in Victoria.
- Jolly, I.D., Dowling, T.I., Zhang, L., Williamson, D.R. and Walker, G.R. 1997. Water and Salt Balances of the Catchments of the Murray–Darling Basin. Adelaide, CSIRO Land and Water Technical Report 37/97.
- Jolly I.D., Williamson D.R., Gilfedder M., Walker G.R., Morton R., Robinson G., Jones H., Zhang L., Dowling T.I., Dyce P., Nathan R.J., Nandakumar N., Clarke R., and McNeill V. 2001. Historical stream salinity trends and catchment salt balances in the Murray–Darling Basin, Australia. *Marine and Freshwater Research*, 52 (1): 53–63.
- Jones, J.A. 2000. Hydrologic processes and peak discharge response to forest removal, regrowth, and roads in 10 small experimental basin, western Cascades, Oregon. *Water Resources Research*, 36, 2621–2642.
- McDonald, R.C., Isbell, R.F., Speight, J.G., Walker, J. and Hopkins, M.S. 1990. Australian Soil and Land Survey Field Handbook, 2nd edition.
- Natural Heritage Trust. 2001. Australian Dryland Salinity Assessment 2000. National Land and Water Resources Audit, Land and Water Australia, Canberra ACT.
- Ritman, K.T. 1995. Structural Vegetation Data: a specification manual for the Murray Darling Basin Project M305.
- Starr, B.J. 1999. The catchment at the time of European settlement. In: Wasson, R.J. and Caitcheon, G., eds, *Soil Erosion, Phosphorous and Dryland Salinity in the Upper Murrumbidgee: Past Change and Current Findings*.
- Turner, K.M. 1991. Annual evapotranspiration of native vegetation in a Mediterranean-type climate. *Water Resources Bulletin*, 27, 1–6.
- Vertessy, R.A. and Bessard, Y. 1999. Anticipating the Negative Hydrologic Effect of Plantation Expansion: Results From a GIS-Based Analysis on the Murrumbidgee Basin.
- Zhang, L., Dawes, W.R. and Walker, G.R. 1999. Predicting the Effect of Vegetation Changes on the Catchment Average Water Balance. CSIRO Land and Water Tech Report 99/12.
- Zhang, L., Dawes, W.R. and Walker, G.R. 2001. The response of mean annual evapotranspiration to vegetation changes at catchment scale. *Water Resources Research*, 37, 701–708.

# 21 Land Degradation Assessment in the Mount Lofty Ranges: Upscaling from Points to Regions via a Toposequence

Phil J. Davies,<sup>\*</sup> Rob W. Fitzpatrick,<sup>\*</sup> David A. Bruce,<sup>†</sup>  
Leonie R. Spouncer<sup>\*</sup> and Richard H. Merry<sup>\*</sup>

## Abstract

Natural resource assessment at regional scales is often time consuming, expensive and reliant upon the local knowledge and judgment of the surveyor. In this chapter we describe the development of an efficient method to assess land degradation (specifically waterlogging and saline and acid soils) at a regional scale. We developed spatial models by integrating knowledge of landscape processes with remotely sensed, terrain and field data, within a geographic information system (GIS). The key to this approach was the linkage of soil and hydrological processes (identified at the point scale) to mapped soil units via toposequences, and the allocation of land degradation classes to each of the units. The data were aggregated to catchment and regional scale to produce maps of land degradation. The results obtained from the modelling were validated by random ground assessments of sites across the region. The method described here could be applied to the assessment of other types of land degradation, and to other regions with comparable landscapes and vegetative covers, where similar soils, terrain and remotely sensed data exist.

区域尺度的自然资源评价既费时又耗资，常常不现实，而且也依赖于评估人员的知识水平、对该地区的了解程度和个人判断能力。本研究提出了评估土地退化（尤其是酸化、盐碱化和渍涝状况）更有效方法，给研究区劳伏特山地各流域的健康状态排名。我们将景观信息、遥感数据、野外数据与地理信息系统相结合，开发出空间模型。该方法的关键在于由布点测量的土壤和水文数据，推算坡面数据，与土壤地图单元联系，确定各单元土壤退化程度。将这些数据再汇总得到流域和区域范围的土地退化图。模型给出的结果

<sup>\*</sup> CSIRO Land and Water, PMB 2, Glen Osmond, SA 5064, Australia. Email: phil.davies@csiro.au

<sup>†</sup> University of South Australia, GPO Box 2471, Adelaide, SA 5001, Australia.

Davies, P.J., Fitzpatrick, R.W., Bruce, D.A., Spouncer, L.R. and Merry, R.H. 2002. Land degradation assessment in the Mount Lofty Ranges: upscaling from points to regions via a toposequence. In: McVicar, T.R., Li Rui, Walker, J., Fitzpatrick, R.W. and Liu Changming (eds), *Regional Water and Soil Assessment for Managing Sustainable Agriculture in China and Australia*, ACIAR Monograph No. 84, 291–303.

和在整个地区野外随机检验结果一致。该方法可评估其他不同形式的土地退化，也可以应用到那些具有相似的景观和植被覆盖、存在类似的土壤地形和遥感数据的地区。

IN THE high-rainfall catchments of the Mount Lofty Ranges, South Australia, land degradation and poor quality of stream water contribute to losses in farm production and to off-site environmental impacts. The replacement of native vegetation by pastures and cereals that use less water has led to the development of salinity throughout the southern Australian agricultural zone. This change in land use increases the amount of water recharging to deeper groundwaters, which then rise and mobilise salt stored in soil profiles. The extent of waterlogged saline scalds is increasing. Such scalds are an early indicator of the formation of saline, structureless soils that are prone to water erosion. This land degradation has serious potential impacts on the supply and quality of Adelaide's drinking water, because the region contributes approximately 50–60% of the city's total supply.

There is no consistent method for assessing waterlogging and soil acidification or alkalinisation in catchments at regional scale. Organisations or individuals assessing land degradation have developed techniques and expertise best suited to the particular task, adopting methods that are subjective, not clearly defined and often only applied to one particular type of land degradation. This lack of consistency is a major obstacle to the reliable assessment of degradation caused, for example, by poor drainage, salinity and erosion.

Our aim was to develop appropriate methods for assessing potential land degradation at the regional level, by upscaling data from point to catchment scale and using it for spatial modelling in a geographic information system (GIS).

### Study Area

The region studied is centred east of the township of Mount Torrens in the Mount Lofty Ranges of South Australia and is approximately 80 km<sup>2</sup> in extent (Fig. 1). The climate is Mediterranean and representative of the eastern Mount Lofty Ranges, with a mean annual rainfall of 680 mm and a mean annual evaporation of 1170 mm. The generalised topography of the area consists of valley floors surrounded by rolling hills, with Mount Torrens lying to the west and a major faultline range defining the eastern extent of the area. A regional northeast to southwest topographic high, east of Mount Torrens township, bisects the area. Catchments to the west of this high drain into the Onkaparinga and Torrens catchment systems; catchments to the east of it form part of the Murray–Darling Basin catchment system. The topographic morphology of the area is strongly related to the underlying geology of near vertical dipping, north–south trending lineament features associated with Precambrian and Cambrian metamorphic formations.

Soils of the area are typical of the eastern Mount Lofty Ranges, being mostly Xerals (Soil Survey Staff 1998), formed from strongly weathered micaceous sandstones and schists of the underlying metasediments. These soils are characterised by abrupt textural boundaries between sandy and loamy textured surface horizons (A and E horizons) and clayey subsurface horizons (B horizons) with mottled and/or sodic properties. The land cover of the area is predominantly pasture, most native tree vegetation having been cleared by the end of the

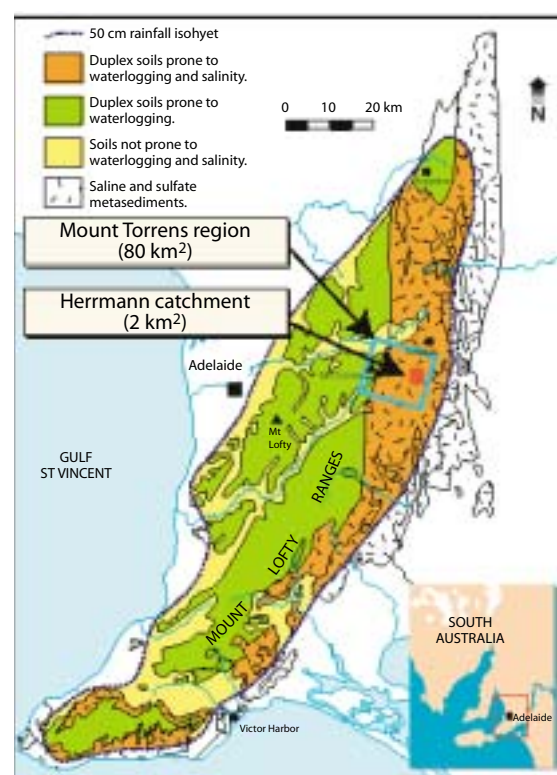


**Figure 1.** The Mount Torrens study area.

1800s. The remaining areas of remnant vegetation are associated mainly with topographic high points, roadways and watercourses.

To facilitate the process of upscaling, we selected a number of areas within the region for which data on soil, landscape, water quality and remote sensing were available. Detailed information on these studies is reported by Fritsch and Fitzpatrick (1994), Bruce (1996), Cox et al. (1996), Fitzpatrick et al. (1996) and Davies et al. (1998).

### Scales and Nature of the Data

This chapter lists and briefly describes some of the various data sets that were used in the analysis. Table 1 summarises the data sets used at each of the various scales within the 80 km<sup>2</sup> regional area. A more comprehensive discussion of these data and how they were derived can be found in Fitzpatrick et al. (1999).

#### Herrmann toposequence (~400 m) and key area (~0.2 km<sup>2</sup>)

Measurements were taken at strategic soil sample points along a 400 m long toposequence within a 0.2 km<sup>2</sup> key area. They include:

- soil morphology, chemistry and mineralogy
- topography (landform)
- vegetation
- hydrology (perched and groundwater fluctuations)
- geomorphology
- multitemporal aerial photography
- airborne thermal infrared (IR) video.

#### Herrmann catchment (~2.0 km<sup>2</sup>)

- 1:5000 scale soil survey mapping
- soil pH measurements
- grid digital elevation model (DEM) and derived topographic index
- airborne synthetic aperture radar (SAR) and derived soil dielectric constant
- airborne thermal IR video
- Landsat Thematic mapper
- airphoto-derived vegetation index
- EM31 derived apparent electrical conductivity (ECa) and discharge index.

#### Mount Torrens region (~80 km<sup>2</sup>)

- 1:50,000 scale landscape unit (SLU) mapping and derived aquic index
- 1:50,000 SLU derived acidity classes
- 1:50,000 scale geology and derived geosalinity classes
- DEM and derived topographic index
- airborne SAR and derived soil dielectric constant
- Landsat Thematic mapper.

### Description of derived data sets

The vegetation index for the catchment was linked to soil drainage conditions. We developed a computerised classification of multitemporal aerial photography corresponding to the late winter and late summer seasons using information collected for the toposequence and key areas. Native and introduced grass species found in different soil drainage and salinity conditions respond in different ways during these seasons. Thermal IR airborne video showed potential for assessing groundwater discharge sites and remnant stream channels. However, the poor geometry of this imagery only permitted interpretation at the key area scale.

Topographic index ( $\ln(A_s/\tan\beta)$ ) is a secondary terrain attribute. It represents the geomorphic processes associated with soil moisture and its spatial distribution in the landscape. To determine the topographic index for the study area, we created a hydrologically correct, grid DEM using the method of Hutchinson (1989), and evaluated the variables of the index using the procedure of Hutchinson and Dowling (1992).

A soil dielectric constant was derived using data from the National Aeronautics and Space Administration Jet Propulsion Laboratory's airborne synthetic aperture radar. We related the constant to soil moisture status by modelling the radar backscatter. For this study we used the empirical approach of Dubois et al. (1995) to derive a dielectric constant for the entire 80 km<sup>2</sup> region.

We used ECa, derived from the EM31 survey,<sup>1</sup> to determine the relative distribution of soluble salts in the landscape and preferred pathways of solute and water flow in the subsurface region. ECa was also a

quick and efficient means to interpolate between sites of known soil properties.

A discharge index, used to partition the landscape into zones of recharge or discharge (Cook and Williams 1998), was also derived from EM31 survey data. This index adds an extra dimension to salinity hazard mapping; it provides a numerical value ranging from strongly negative for low salinity/strongly recharging soils to strongly positive for high salinity/strongly discharging soils.

We derived an aquic index from the land classification attributes associated with the digital 1:50,000 scale SLU data mapped by Primary Industries and Resources South Australia (PIRSA). These attributes or land qualities include drainage, water erosion potential, scalding, salinity and recharge potential. The classification ranks each of these qualities on a numeric scale according to eight generically defined class limits. We considered salinity and drainage to be indicative of aquic conditions (i.e. soil landscape units prone to waterlogging).

We constructed geosalinity classes from the digital geology 1:50,000 scale coverage from PIRSA and classified representative units on the basis of inferred landscape salinity effect. Unit classifications ranged from no significant effect, to acting as a potential source of cyclic salt, to being a source of pyritic materials capable of causing aggressive acid weathering and salt generation (sulfate, chloride, magnesium, sodium, calcium and iron).

To predict the distribution of acidity classes over the region, we consolidated the acidity attribute of the 1:50,000 SLU data from the catchment survey into five classes that represent the progression from extreme profile alkalinity (and sodicity) to extreme profile acidity. These classes are associated with susceptibility to dispersion, salinity and erosion in the case of extreme alkalinity and acidification.

<sup>1</sup> EM31-D is an electromagnetic induction instrument (manufactured by Geonics Ltd, Mississauga, Ontario, Canada), used to measure the apparent electrical conductivity of the ground.

## Methodology

### Upscaling and spatial modelling

Our approach was to extrapolate soil and hydrological process patterns recognised in the field from point scale to catchment and region by aggregating them. Such upscaling is generally difficult due to the lack of relevant and precise data at the broader scale (Wood et al. 1988; King et al. 1998). The problem can be overcome by linking process patterns to mapped soil units via the toposequence and allocating land degradation classes to each of the units. This approach integrates broader-scale soil, geology, terrain and remotely sensed data within a GIS modelling environment.

Most of the nonpoint data used for this study consists of multiclass raster (regular grid cell) coverages. As the objective was to assess potential land degradation at the regional level, we decided to use a weighted index overlay as the spatial modelling technique (Bonham-Carter 1994). This model is linear, additive and suitable for ranking areas according to potential for degradation (i.e. it is predictive). We evaluated each coverage according to a weighted criterion, based on both

trial data and expert knowledge, and scaled the results of the model by applying a classification table of breakpoints to the ranking. The resulting classified data set provided an estimate of potential land degradation that could be verified by limited, random field survey.

The modelling procedures for waterlogged, saline and acid soil conditions are described below for each of the scales. To illustrate the approach we give examples of data models and results for estimates of drainage/waterlogging at each scale. Full details of the procedures and results are reported in Fitzpatrick et al. (1999).

### Toposequence/key area

For the toposequence/key area, we analysed a range of detailed point data. The steps outlined below were used to select, describe, distinguish and construct the soil layers in the toposequence. Using this data we could map soil profiles in the key area surrounding the toposequence and thus extrapolate landscape degradation patterns to the catchment and regional level.

**Table 1.** Summary of data sets used at different scales for different types of land degradation.

Data	Scale											
	Toposequence			Key area			Catchment			Region		
	D/W	SAL	A/A	D/W	SAL	A/A	D/W	SAL	A/A	D/W	SAL	A/A
Soil samples												
Hydrology												
Topography												
Vegetation												
EM31												
Soil dielectric												
SLU												
Geology												

Note: shaded boxes indicate data used for that scale; if boxes are not shaded, data were not used at that scale. A/A = acidity/alkalinity; D/W = drainage/waterlogging; EM31 = conductivity; SAL = salinity; SLU = scale landscape unit

*Steps in the process**Select representative catchments and toposequences*

- Collate existing information on soil, geology and vegetation.

*Describe morphological features in toposequences*

- Describe morphological features in soil layers (e.g. soil colour and stone lines).
- Identify soil horizons (e.g. E or Btg) to compare with common scientific terminology.

*Group and map morphological features in toposequences*

- Group similar morphological features into a smaller number of soil layers (soil systems) using the structural analysis approach (Fritsch et al. 1992), which groups soil features by nested or concordant relationships.
- Develop cross-sections of toposequences for the combined soil layers.

*Match soil layers to pedohydrological processes*

- Monitor watertable fluctuations (using piezometers and dipwells), soil redox potentials (using Eh probes) and geochemical changes such as EC.
- Link soil and hydrological processes, such as water flow paths and salinity, to each soil layer.

*Identify soil mapping units in a key study area surrounding the toposequence*

- Collect field survey data from boreholes and representative soil profiles down several toposequences, and analyse soil samples in the laboratory.
- Define landscape and soil mapping units in the key study area using 1:5000 scale aerial photography.
- Determine a range of diagnostic variables for each mapping unit from field observations and soil profile analysis.

*Link soil and hydrological processes to the soil mapping units*

- Allocate drainage/waterlogging, salinity and acidity/alkalinity classes to each map unit by linking to soil and hydrological processes.

For each type of land degradation (drainage/waterlogging, salinity and acidity/alkalinity), eight classes were allocated to soil layers in the toposequence and five to soil profiles for the key area. Figure 2 illustrates the model used to estimate soil drainage/waterlogging at both scales.

*Results—toposequence/key area*

Table 2 illustrates the relationships that were developed for each of the three types of land degradation from the toposequence and key area studies. Figure 1 of Chapter 9 shows the estimate of soil drainage/waterlogging for the toposequence and Figure 3 of this paper shows the estimate for the key area. The types of land degradation were verified using soil survey and hydrological data (Cox et al. 1996; Fitzpatrick et al. 1996).

**Catchment**

Before data modelling and mapping, we developed a GIS for the catchment area to integrate and analyse field and remote sensing data. We digitised the soil survey data at 1:5000 scale, derived from aerial photography and borehole investigations (Fig. 4) and attributed it to the classes defined in Table 2. This information helped us to rank potential drainage/waterlogging, salinisation and acidification at the catchment scale.

We estimated soil drainage/waterlogging from the weighted overlay of vegetation index, topographic index, soil dielectric and EM31-derived discharge index (Fig. 5); salinity from the weighted overlay of topographic index, soil dielectric and EM31-derived EC; and acidity/alkalinity from the weighted overlay of topographic index, geology and soil pH measures.

**Table 2.** Soil mapping units and associated drainage/waterlogging, salinity and acidity/alkalinity classes for the Herrmann toposequence and key area.

Map unit	Landform elements	Soil description	Drainage/waterlogging	Acidity/alkalinity <sup>a</sup>	Salinity (EC <sub>se</sub> )/depth to saline water (m)
1a	Flat	Grey sandy loam surface layer over yellow-grey mottled clay	Poorly drained Strongly waterlogged	Moderately acidic (pHw=<6.5) surface, neutral to alkaline at depth	Slightly saline 1–4 dS/m; 1–1.5 m
2n	Flat	Salt efflorescence (halite and gypsum) on surface with grey sandy loam surface over yellow-grey clay	Poorly drained Strongly waterlogged	Mostly alkaline throughout (pHw >7.5)	Very saline >8–16 dS/m < 1 m
3s	Flat/lower slope seepages	Salt efflorescence (halite and gypsum) on surface with loamy black sulfidic material overlying yellow-grey clay	Very poorly drained Strongly waterlogged	Mostly alkaline throughout (pHw >7.5); sporadic occurrences of highly acidic (pHw <5.5) near-surface layers (<5cm), which develop due to oxidation of sulfidic materials	Extremely saline >16 dS/m; < 1 m
4a	Lower slope, open depression	Grey sandy loam surface layer over yellow-red-grey mottled clay	Poorly drained Periodic waterlogging	Neutral throughout (pHw 6.5–7.5)	Slightly saline 1–4 dS/m 1.5–3 m
5s	Lower slope, open depression	Deep grey sand over yellow-grey mottled clay	Poorly drained Periodic waterlogging	Acidic throughout (pHw=<6.5) (low buffer capacity)	Nonsaline <1 dS/m; 1.5–3 m
6l	Crest	Shallow sandy loam over red uniform coloured clay over weathered rock	Freely drained Infrequently waterlogged	Very acidic throughout (pHw <5.5)	Nonsaline <1 dS/m > 3 m
7a	Mid-slope	Brown loam over red and yellow uniform coloured clay. Deep.	Freely drained Infrequently waterlogged	Moderately acidic (pHw <6.5) throughout	Nonsaline <1 dS/m > 3 m
7ag	Crest, upper-slope	Deep well-drained red and yellow soils	Freely drained Infrequently waterlogged	Moderately acidic (pHw <6.5) surface, neutral to alkaline at depth	Nonsaline <1 dS/m > 3 m
7b	Crest, upper-slope	Deep well-drained red and yellow soils	Freely drained Infrequently waterlogged	Very acidic throughout (pHw <5.5)	Nonsaline <1 dS/m > 3 m
7bg	Crest, upper-slope	Shallow well-drained red yellow soils	Freely drained Infrequently waterlogged	Moderately acidic (pHw <6.5) throughout	Nonsaline <1 dS/m > 3 m
7c	Lower slope, open depression	Shallow well-drained yellow soils	Moderately drained Infrequently waterlogged	Neutral throughout (pHw 6.5–7.5)	Nonsaline <1 dS/m 1.5–3 m
Rq	Crest, upper-slope	Shallow well-drained yellow and red soils with quartz fragments	Freely drained Infrequently waterlogged	Moderately acidic (pHw <6.5) throughout	Nonsaline <1 dS/m > 3 m
Rf	Crest, upper-slope	Shallow well-drained yellow and red soils with ferricrete fragments	Freely drained Infrequently waterlogged	Very acidic throughout (pHw <5.5)	Nonsaline <1 dS/m > 3 m
Rs	Mid-slope	Shallow well-drained red soils with micaceous rock fragments	Freely drained Infrequently waterlogged	Moderately acidic (pHw <6.5) surface, neutral at depth, high buffer capacity	Slightly saline 1–4 dS/m > 3 m
E	Flat/stream channel	Gully, tunnel and rill erosion	Very poorly drained Strongly waterlogged	Mostly alkaline throughout (pHw >7.5)	Extremely saline >16 dS/m; < 1 m

<sup>a</sup> pHw means that the pH measurement was taken in water

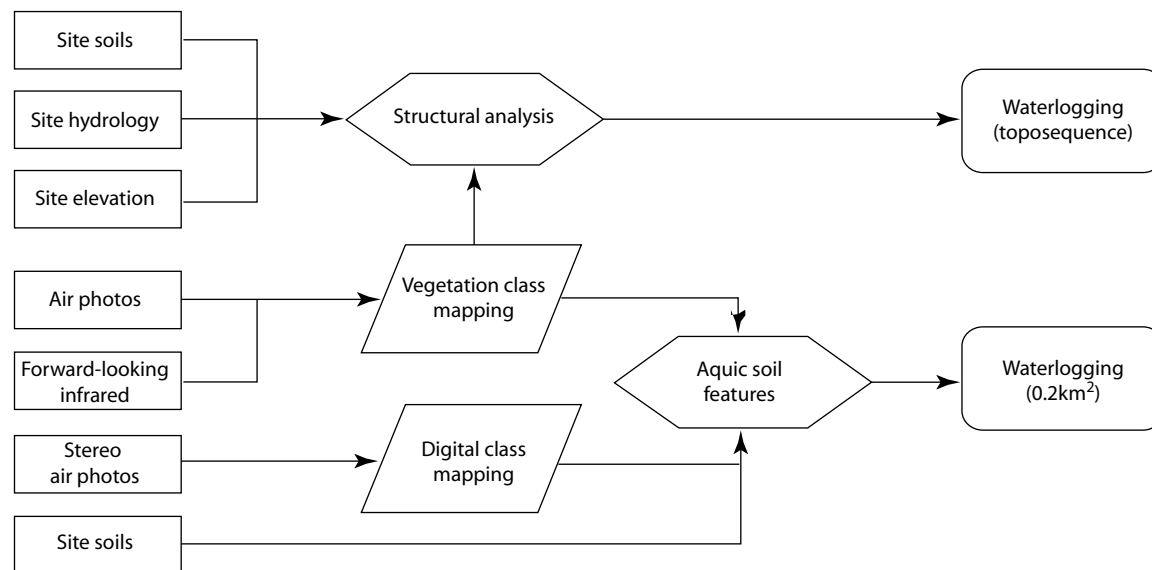


Figure 2. Drainage/waterlogging data model for the toposequence and key area.

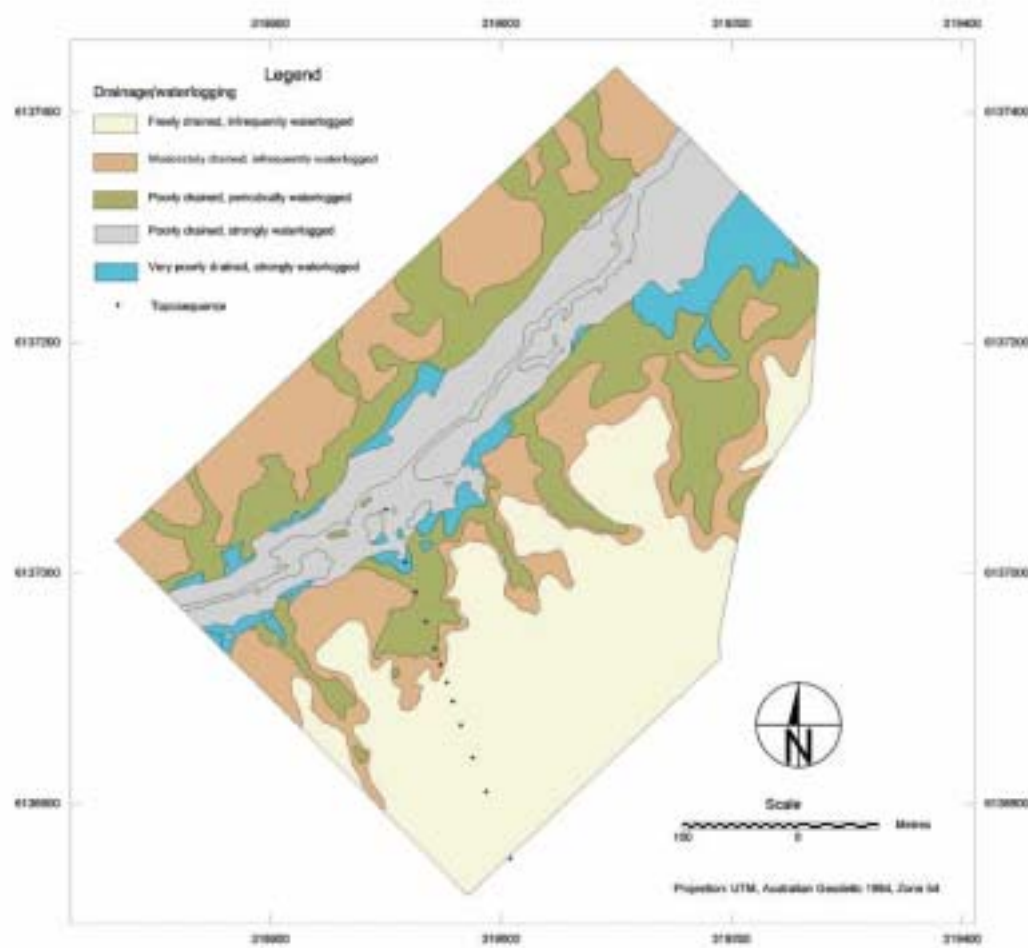


Figure 3 Estimate of drainage/waterlogging for the key area.

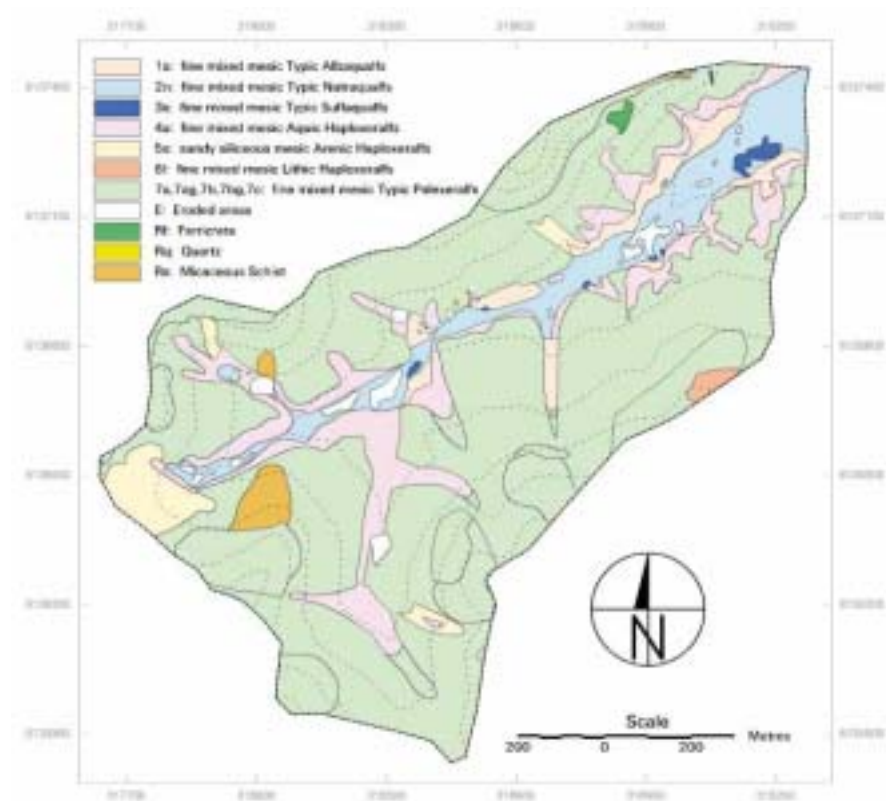


Figure 4. 1:5000 scale soil survey of the Herrmann catchment.

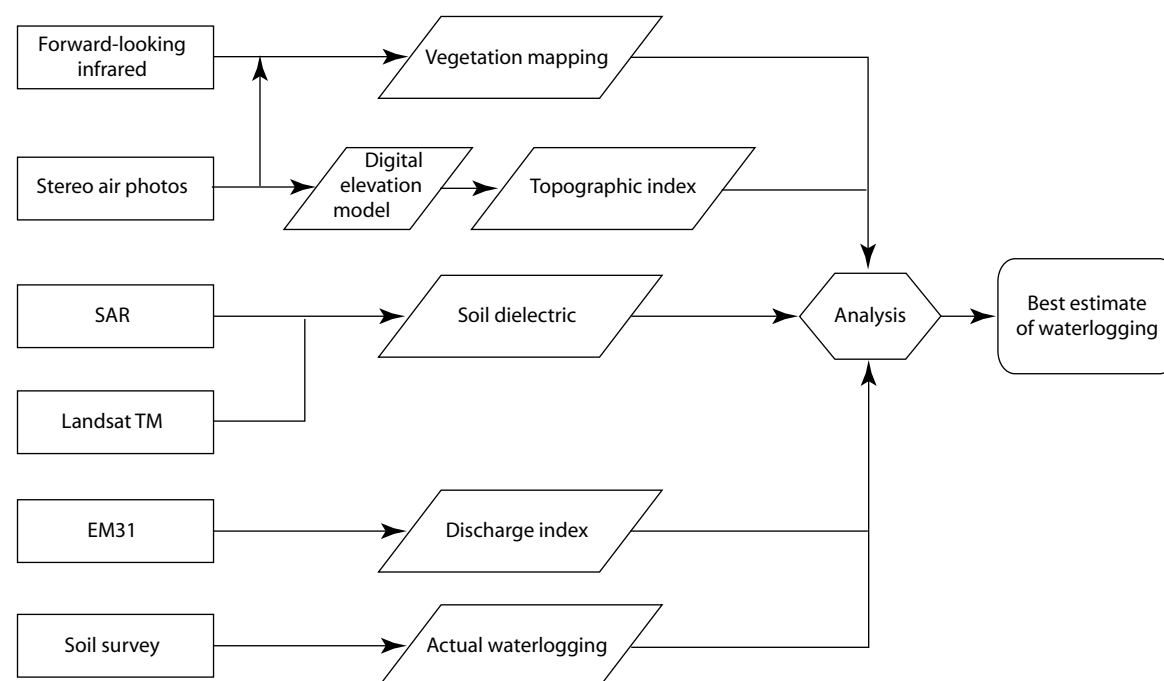


Figure 5. Drainage/waterlogging data model for the catchment. SAR is airborne synthetic aperture radar; Landsat TM is Landsat Thematic mapper; EM31 is derived apparent electrical conductivity.

### Results—catchment

Each of the three estimates for the catchment was classified according to the relevant types of land degradation mapped by the 1:5000 scale soil survey. Figure 6 compares the estimate of drainage/waterlogging to mapped information. In general, the estimated results show a positive relationship with the field mapping (Davies et al. 2000). The results of the weighted overlay modelling are affected by any anomalies in the input data. For example, the discharge index showed an area of discharge in the catchment that does not correlate with drainage/waterlogging as mapped by survey. This was explained by field investigations, which indicated an area of clay-rich soil (not previously mapped) that was being incorrectly sensed by the EM31 survey as an area of high ECa.

### Region

Some of the higher resolution data used for catchment modelling are not available at regional scale. The weighted overlay model provided a

means to aggregate the appropriate broader scale data with suitable higher resolution data, to allow ranking of the potential for land degradation.

At a regional scale, drainage/waterlogging was estimated from the weighted overlay of topographic index, soil dielectric and SLU-derived aquic index (Fig. 7); salinity from the weighted overlay of geology, soil dielectric and topographic index; and acidity/alkalinity from the weighted overlay of topographic index and SLU-derived acidity index.

### Results—region

Figure 8 shows the results of modelling to estimate drainage/waterlogging at the regional scale. Thirty-five independent historical sites and five recently sampled random sites were used to verify the three land degradation estimates at regional scale. The estimates from the model correlated well with the site samples. More detailed analyses of the acidity estimates are included in Merry et al. (2000).

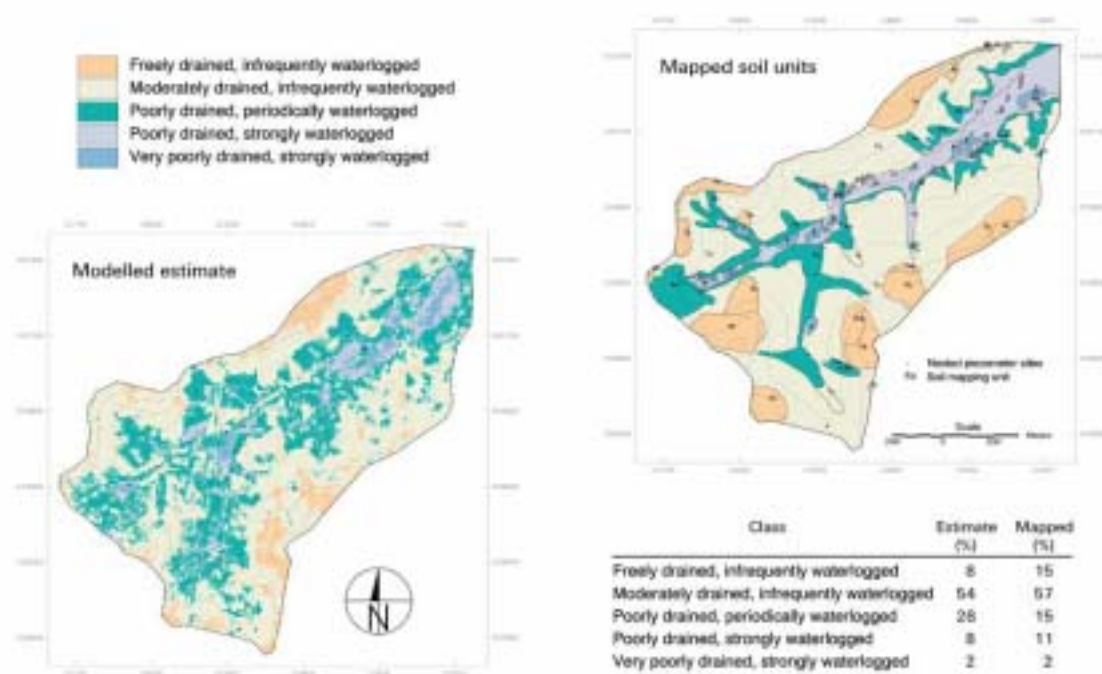


**Figure 6.** Potential waterlogging in the Herrmann catchment: comparison of map of best estimate data with mapped soil units.

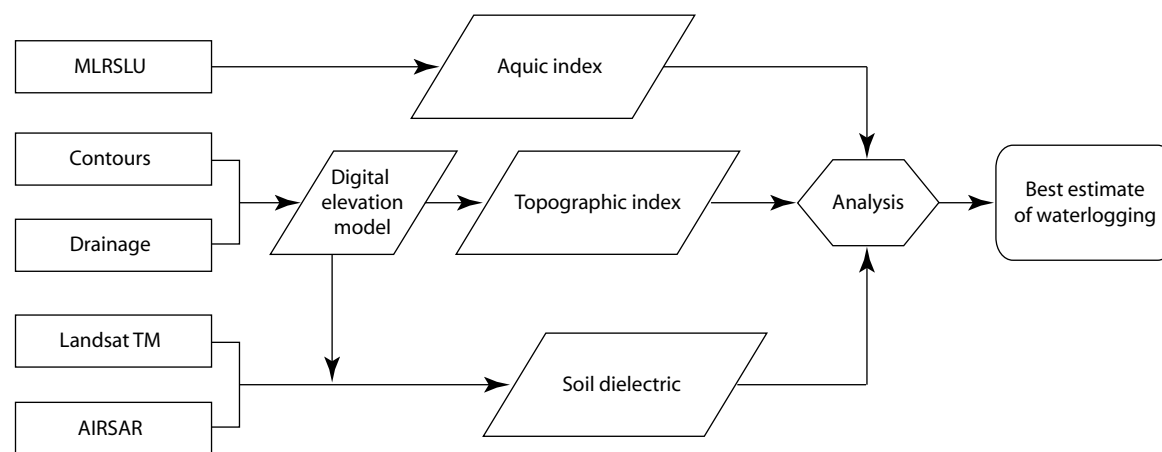


**Figure 7.** Drainage/waterlogging data model for the Mount Torrens region. MLRSLU = Mount Lofty Ranges scale landscape unit; TM = Thematic mapper.

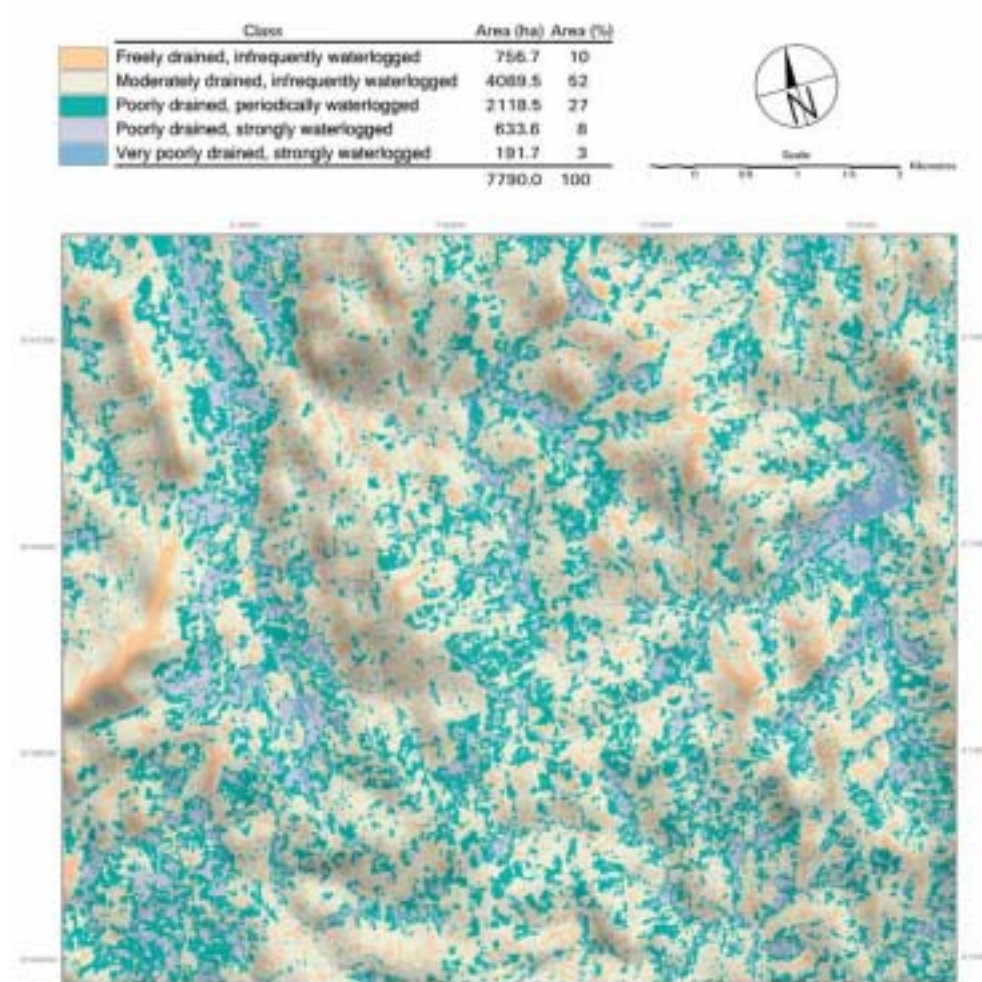


**Figure 8.** Estimate of drainage/waterlogging for the Mount Torrens region.

## Discussion

Using relationships developed from detailed toposquence studies we were able to classify each type of land degradation for the 1:5000 scale soil survey. This classification allowed us to explore the value of broader-scale spatial data in weighted overlay modelling.

Using the models, we could aggregate many of the data sets at the regional scale and rank the potential for land degradation. These rankings could then be classified at the catchment scale using mapped areas and at the regional scale using information obtained from random sites. The extensive use of topography in the form of a grid-based DEM at all scales was a major factor in the ability to aggregate many of the data sets at the regional scale.

The linear, additive nature of the weighted index overlay technique has some disadvantages — any anomalies in the input data tend to modify the results. In such cases, a fuzzy logic method with more flexible combination rules would be advantageous. In this study, anomalies were partially resolved by obtaining appropriate field samples.

The classified ranking provided estimates of waterlogged, saline and acid soils at the regional scale. Although the results have only been analysed qualitatively and have not undergone spatial statistical analyses, they show good agreement with data from independent site checks across the region.

## Conclusions

We successfully used a number of different sets of data to upscale assessment of land degradation. The key to translating between scales is to link point-scale process patterns to mapped soil units and allocate land degradation classes to each of the units. We were able to extrapolate point observations to the catchment and regional scale by integrating broader-scale data through weighted overlay modelling within a raster GIS environment.

Using models, we could characterise and assess natural resource status and condition at a scale appropriate for ranking the relative quality of catchments. Regional assessment of land degradation can be used in conjunction with a soil assessment manual (Fitzpatrick et al. 1997) to map problem sites and develop strategies for property management. This approach can help Landcare groups and government agencies to make decisions on resource management based on the knowledge of soil conditions.

The approach described here could be applied to other types of land degradation, and could be used in other regions with comparable landscapes and vegetative covers, where there are similar soils, terrain and remotely sensed data.

## Acknowledgments

The authors gratefully acknowledge funding support and assistance: The research was funded by ACIAR and in part by the National Heritage Trust through the National Land and Water Resources Audit. Dr Emmanuel Fritsch (pedology) and Mr David Maschmedt (pedology, interpretation of SLU data) contributed substantially to this study. The Tungkillio Landcare Group provided encouragement and assistance with site access. PIRSA kindly provided the 1:50,000 scale soil landscape unit and geology data.

## References

- Bonham-Carter, G.F. 1994. *Computer Methods in the Geosciences: geographic information systems for geoscientists: modelling with GIS*. Oxford, Pergamon.
- Bruce, D.A. 1996. Soil moisture from multi-spectral, multi-polarising SAR. In: *Proceedings of 8th Australasian Remote Sensing Conference*, Canberra, March.
- Cook, P.G. and Williams, B.G. 1998. *Basics of Recharge and Discharge: Part 8 Electromagnetic induction techniques*. Collingwood, CSIRO Publishing.
- Cox, J.W., Fritsch, E. and Fitzpatrick, R.W. 1996. Interpretation of soil features produced by ancient and modern processes in degraded landscapes: VII. Water duration. *Australian Journal of Soil Research*, 34, 803–824.
- Davies, P.J., Bruce, D.A., Fitzpatrick, R.W., Cox, J.W., Maschmedt, D. and Bishop, L. 1998. A GIS using remotely sensed data

- for identification of soil drainage/waterlogging in southern Australia. Proceedings of the International Soil Science Society Congress, Montpellier, France. 20–26 August, 1998.
- Davies, P.J., Fitzpatrick, R.W., Bruce, D.A., Spouncer, L.R. and Merry, R.H. 2000. Use of spatial analysis techniques to assess potential waterlogging in soil landscapes. In: Adams, J.A. and Metherell, A.K., eds, *Soil 2000: New Horizons for a New Century*. Australian and New Zealand Second Joint Soils Conference. Volume 3: Poster Papers. 3–8 December 2000, Lincoln University. New Zealand Society of Soil Science.
- Dubois, P.C., van Zyl, J.J. and Engman, E.T. 1995. Measuring soil moisture with imaging radars. *IEEE Transactions on Geoscience and Remote Sensing*, 33, 4, 510–516.
- Fitzpatrick, R.W., Fritsch, E. and Self, P.G. 1996. Interpretation of soil features produced by ancient and modern processes in degraded landscapes: V. Development of saline sulfidic features in non-tidal seepage areas. *Geoderma*, 69, 1–29.
- Fitzpatrick, R.W., Cox, J.W. and Bourne, J. 1997. Managing waterlogged and saline catchments in the Mount Lofty Ranges, South Australia: a soil-landscape and vegetation key with on-farm management options. *Catchment Management Series*. CRC for Soil and Land Management. CSIRO Publishing, Melbourne. 36 pp. ISBN 1 876162 30 9.
- Fitzpatrick, R.W., Bruce, D.A., Davies, P.J., Spouncer, L.R., Merry, R.H., Fritsch, E. and Maschmedt, D.J. 1999. Soil Landscape Quality Assessment at Catchment and Regional scale: Mt Lofty Ranges Pilot Project, final technical report. CSIRO Land and Water Technical Report No. 28/1999, 50 p.
- Fritsch, E., Peterschmitt, E. and Herbillon, A.J. 1992. A structural approach to the regolith: Identification of structures, analysis of structural relationships and interpretations. *Sciences Géologiques*, 45, 2, 77–97.
- Fritsch, E. and Fitzpatrick, R.W. 1994. Interpretation of soil features produced by ancient and modern processes in degraded landscapes: I. A new method for constructing conceptual soil–water–landscape models. *Australian Journal of Soil Research*, 32, 889–907 (colour figs. 880–885).
- Hutchinson, M.F. 1989. A new procedure for gridding elevation and stream line data with automatic removal of spurious pits. *Journal of Hydrology*, 106, 211–232.
- Hutchinson, M.F. and Dowling, T.I. 1992. A continental hydrological assessment of a new grid-based digital elevation model of Australia. In: Beven, K.J. and Moore, I.D., eds, *Terrain Analysis and Distributed Modelling in Hydrology*. Chichester, John Wiley.
- King, D., Fox, D.M., Daroussin, J., Le Bissonnais, Y. and Danneels, V. 1998. Upscaling a simple erosion model from small area to a large region. *Nutrient cycling in Agroecosystems*, 50, 143–149.
- Merry, R.H., Spouncer, L.R., Fitzpatrick, R.W., Davies, P.J. and Bruce, D.A. 2000. Prediction of soil profile acidity and alkalinity—from point to region. In: Adams, J.A. and Metherell, A.K., eds, *Soil 2000: New Horizons for a New Century*. Australian and New Zealand Second Joint Soils Conference. Volume 3: Poster Papers. 3–8 December 2000, Lincoln University. New Zealand Society of Soil Science.
- Soil Survey Staff 1998. *Keys to Soil Taxonomy*, 8th edition. Washington, US Government Printing Office: USDA, Natural Resources Conservation Service.
- Wood, E.F., Sivapalan, M., Bevan, K.J. and Band, L.E. 1988. Effects of spatial variability and scale with implications to hydrological modelling. *Journal of Hydrology*, 102, 28–47.

# 22 Regional Evaluation of Soil Erosion by Water: a Case Study on the Loess Plateau of China

Yang Qinke,\* Li Rui,\* Xiaoping Zhang\* and Liangjun Hu\*

## Abstract

This chapter discusses how spatial information techniques can be used to predict and evaluate regional soil erosion. The study, carried out in central China, identified sediment discharge, precipitation, soil composition, gully density and land use as the controlling factors of regional erosion. The authors found that soil erosion can be assessed and predicted quantitatively at a regional scale; that quantitative evaluation can be used to study and describe the soil erosion mechanism at the macro scale; and that soil erosion at the national or provincial scale can be rapidly surveyed using remote sensing, geographic information systems (GIS) and erosion modelling.

本研究以黄土高原为例，在分析了区域水土流失过程、类型和分布特点的基础上，拟定了区域水土流失评价指标体系，包括：沟壑密度、汛期降雨量、土壤团粒含量、植被盖度、坡地面积比等。根据遥感影像划分编制了评价单元图并在 GIS 环境下集成各评价因子建立了评价数据库。根据地理统计方法建立了评价模型。研究表明：区域水土流失宏观趋势的定量评价预测是可能的，基于水土保持类型区的定量评价，可以揭示区域水土流失的宏观规律，进而实现区域水土流失快速调查是可能的。最后对于模型进一步改进方法和途径进行了讨论。

\* Institute of Soil and Water Conservation, Chinese Academy of Sciences and Water Resources Ministry, Yangling, Shaanxi 712100, PRC.  
Email: qkyang@ms.iswc.ac.cn

Yang Qinke, Li Rui, Xiaoping Zhang and Liangjun Hu. 2002. Regional evaluation of soil erosion by water: a case study on the Loess Plateau of China. In: McVicar, T.R., Li Rui, Walker, J., Fitzpatrick, R.W. and Liu Changming (eds), *Regional Water and Soil Assessment for Managing Sustainable Agriculture in China and Australia*, ACIAR Monograph No. 84, 304–310.

CHINA suffers severe soil erosion (Xianmo Zhu et al. 1999; Qinke Yang 1994). As the country's economy has developed, soil conservation and ecological rehabilitation have been increasingly taken into account and land-use policy has shifted its focus from small watersheds to large regions (China's Agenda 21 1994; Posen et al. 1996). As a result, policy makers and those responsible for planning soil conservation and environmental rehabilitation measures are demanding systematic information about the current situation and trend of soil erosion, and the benefits of soil conservation and ecological rehabilitation practices. This information is required urgently and will need to be continually updated.

Regional soil erosion and conservation are not just local effects; they also affect the surrounding region, including rivers downstream. Widespread events such as floods, sediment deposition in rivers and reservoirs, dust storms, land degradation and water shortages may result from localised erosion events. Consequently, we must quantify and predict the degree and effects of soil erosion at the regional, national and even global scales.

Spatial information sciences and techniques—including remote sensing, geographic information systems (GIS), global positioning systems (GPS) and related internet technology—have been widely applied to soil erosion monitoring and surveying since the 1980s. In China, the technology for modelling and predicting soil erosion has been developed and applied at the regional scale using GIS and remote sensing (Rui Li et al. 1998; Qinke Yang and Rui Li 1998; Feng Jiao et al. 1998). Usually the study area is divided into several integrated spatial units, so the heterogeneous characteristics or spatial differentiation of the units can be taken into account. Most research into erosion evaluation and prediction has been carried out at the scale of the slope or plot (Renard et al. 1997); there have been relatively few regional studies. Where studies have been carried out, they have usually been based on small areas, with scaling up and/or aggregation being used to extrapolate soil erosion data to a

regional or even global scale (Posen et al. 1996; Kirkby et al. 1996; Qinke Yang and Rui Li 1998).

China has been divided into eight soil erosion areas and the soil erosion trend in each has been predicted by relating sediment discharge to factors such as annual runoff, daily maximum runoff and control area (%) (Peihua Zhou 1988). Soil erosion data can also be obtained by the aggregation method using plot data from the United States Department of Agriculture (USDA) monitoring network (Rui Li et al. 1998). However, the problems of evaluating and predicting soil erosion regionally are not entirely solved.

## Methodology

### Study area

The study area was the 623,700 km<sup>2</sup> Loess Plateau, in central China. The plateau includes the southern part of Ningxia Autonomous Region, the whole of Shanxi Province, northern Shaanxi Province, the eastern and central parts of Gansu Province, the southern part of the Inner Mongolia Autonomous Region, and the western part of Henan Province. It borders the Riyue Mountains to the west and the Taihang Mountains to the east; and it extends from Qinling Mountains in the south to the Yingshan Mountains in the north. Figure 1 in the Overview shows the general location of the area.

The Loess Plateau is located in the second of the three grand relief landform terraces in China. The basic geomorphological types include loess hills, sand-loess hills and loess tableland; the gully density is 4–6 km/km<sup>2</sup> and 40–60% of the area has gullies. The climate is continental monsoonal, with mean annual temperature between 6.6 and 14.3°C and mean annual precipitation between 250 and 700 mm. Rain falls mainly in summer (50–70% of the annual total) and is most intense from July to October. The dominant soils are widely eroded, especially in northern Shaanxi Province, central eastern Gansu Province and western Shanxi Province. Secondary vegetation is limited to only a

few stony hills. For over 2000 years, crop growing has been the main form of land use in the area. The population density is 40–270/km<sup>2</sup>. The relationship between the agricultural activities of people and the natural environment is not harmonious.

Figure 1 shows how erosion can be subdivided according to erosive intensity. According to this classification, the Loess Plateau has three erosion regions: the water erosion region, the wind–water erosion region and the wind erosion region.

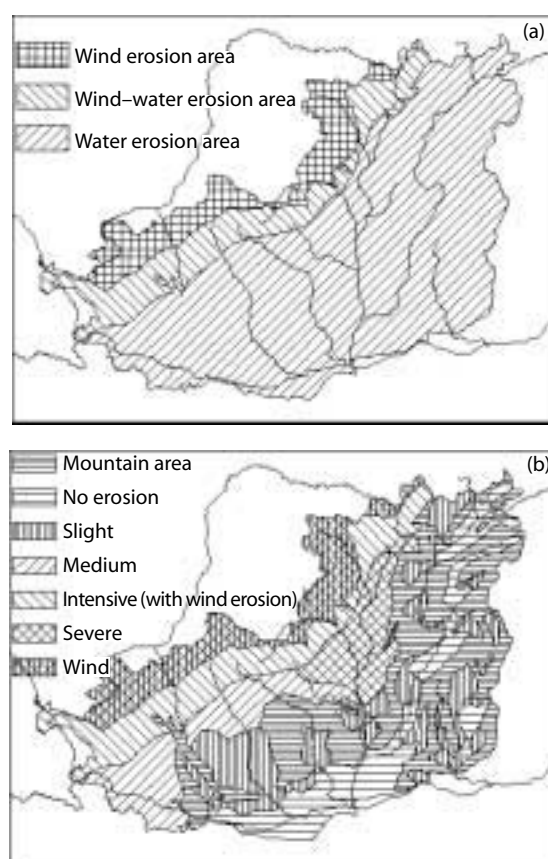


**Figure 1.** Soil erosion map of the Loess Plateau, showing (a) the types of erosion and (b) the major regions of erosion.

### Data and materials

Field surveys and cartographic research by Xianmo Zhu (1981a, b; 1982a, b) show that regional soil erosion is a very complicated process that is affected

by many factors, including geomorphology, soil conditions, meteorology, hydrology, land use, vegetation coverage and soil conservation measures. By analysing these environmental factors and how they affect erosion, we describe the processes of regional erosion and quantitatively evaluate the interactions of the factors and the ability to semi-empirically model the spatial distributions of erosion intensity. In this study, we use the following data.

- **Sediment discharge data** were obtained from the records of 250 hydrological stations covering the period from 1959 to 1986.
- **Precipitation data** measured from 1955 to 1986 at 178 meteorology stations were used to calculate the mean rainfall in the rainy season (July to October).
- **Soil classification data** were obtained from the 1:2,000,000 Loess Plateau soil map produced in 1991 by the Institute of Soil and Water Conservation (ISWC), the Chinese Academy of Sciences and the Ministry of Water Resources. Soil organic matter content data were extracted from monographs that reported the results of the second national soil survey.
- **Gully density data** were determined from gully density annotation points from a 1:500,000 soil erosion map of the Loess Plateau that was produced in 1991.
- **Land-use data.** We estimated the ratio of cropland to forest/grassland from a 1:250,000 land-use map in ArcInfo format, produced by ISWC in 1993 based on the interpretation of Landsat Thematic mapper (TM) data (see Chapter 16 for further details).

Precipitation, sediment and gully density data were in coordinate format ( $x,y,z$ ) and were spatially interpolated and contoured using ArcInfo. All data were transformed into the Albers projection.

### Parameters and database

Table 1 shows the parameters selected for the evaluation. Their choice was dictated by what was needed for prediction and by what was available over the entire study area.

The characteristics of regional soil erosion vary over space and time. Consequently, multilevel areas and classes of erosion can be identified. The study of erosion on a regional scale is based on experimentation and observation at plot and watershed scales, but the data cannot simply be extrapolated from a slope surface or other small area to a larger area using spatiotemporal modelling of the environment (Burrough 1998).

To adequately describe the study, the study area must be discretised in space and time. Conventionally, geonities in space are described by vector data such as points, lines and polygons and other common factors. We divided our study area into 3380 spatial units of uniform map area (UMA) according to Landsat TM imagery.

The parameters were processed into map format and integrated into each of the UMAs, based on the theory and method of the georelationship model. During the process of integration, the data for location and topology were based on the UMA map or base map. The number of data entities on the base map remained constant during data integration.

## Results and Analysis

### Modelling regional erosion

The general format of the model of regional erosion is:

$$A = f(Q, S, g, v, c) \quad (1)$$

**Table 1.** Parameters used in the evaluation.

Erosion factor	Soil erosion	Climate	Soil	Plant	Land use	Relief
Parameter	Sediment intensity	Rainfall in wet season	The fraction of soil (g/kg) with a diameter > 0.25 mm	Plant cover	Slope to area ratio	Gully density

where  $A$  is the erosion intensity,  $Q$  is a hydrological/climate factor,  $S$  is a soil factor,  $g$  is a landform factor,  $v$  is a vegetation factor, and  $c$  is a conservation measure factor.

There is an exponential correlation between the amount of erosion, the amount of rainfall in the rainy season, the gully density, the proportion of slope cropland, the coverage of vegetation and the content of aggregate ( $\geq 0.25$  mm) (JunJie Ma 1990; JiYang Liang 1992; QiuSheng Wang 1991). The relationship can be expressed as:

$$L = 0.4735P^{0.9282} S^{-0.08855} \times G^{2.2666} M^{0.07254} e^{-0.00047C} \quad (2)$$

where  $L$  is the erosive intensity (tonnes/km<sup>2</sup>/year),  $P$  is the precipitation in the wet season (mm),  $S$  is aggregate content (g/kg),  $G$  is the gully density (km/km<sup>2</sup>),  $M$  is the ratio of slope cropland (%), and  $C$  is vegetation cover (%).

The highly significant regression result ( $r = 0.937$ ,  $F = 2984.64 \gg F_{0.05} = 2.21$  where  $F$  is the  $F$ -statistic, which is much higher than the level for 5%) indicates that the erosive intensity is positively correlated with rainfall quantity in the wet season, gully density, and the proportion of slope cropland. It is negatively correlated with the content of aggregate and vegetation cover. In other words, the higher the rainfall in the wet season, the greater the erosion intensity; the higher the aggregate content and vegetation covering, the lower the erosion intensity. This accords with general principles of soil erosion, and with other research in this field.

### Evaluating the erosion factors

We have identified five variables controlling erosion regionally. These variables can be converted into

specific units and extracted from existing survey or remote sensing information. The variables are suitable for a macro study to evaluate trends, as in our study. Land-use data provide some indication of the extent to which soil and water conservation are practised in the region. For the purpose of analysing erosion potential, the landscape can be categorised into plains, terraces, hills and mountains. There are obvious differences between the categories in patterns of erosion, measures and patterns of soil conservation and types of reasonable land use. Topographic maps and TM imagery have made it possible to determine locations with a high degree of accuracy. As the UMA map has 2230 polygons and the 1:500,000 Loess Plateau erosion map has only 1100 polygons, each UMA can contain values derived from different thematic layers. Thus, erosion levels can differ within UMAs for the same landscape zone.

We applied several algorithms for attribute values from the maps (in digital format) to the databases. We used a flexible method to calculate the relationship between location and descriptive data. Consequently, all variables in the model can be integrated into the UMA map, and a database with multi-items can be built to satisfy the demands of multifactor evaluation (Qinke Yang 2001).

Figure 2 is a GIS map showing soil erosion calculated using Equation 2; it shows the relationships among the different factors affecting soil erosion and accords with the spatial differentiation pattern of soil erosion observed on the Loess Plateau. The result is useful in macro policy making.

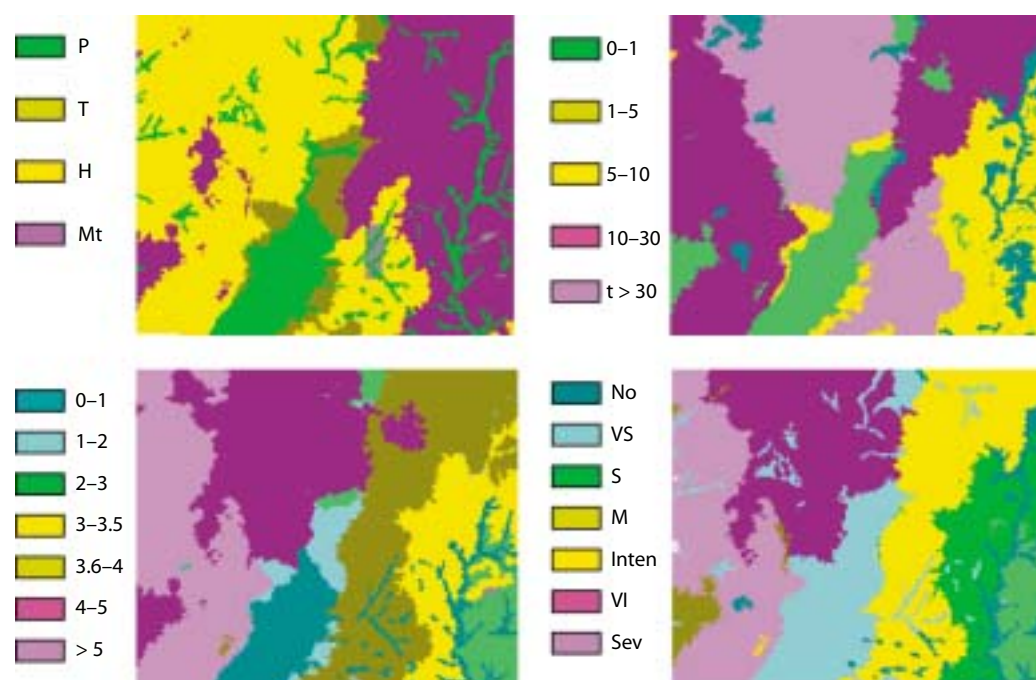


**Figure 2.** An example of factors influencing regional erosion modelling for a 127 km × 117 km portion of the Loess Plateau situated in Shaanxi Province. The top left image is of landform; P is plain; T is tableland; H is hill; and Mt is mountains. The top right image is the percentage slope of cropland for each polygon. The lower left image shows the density of gullies (km/km<sup>2</sup>). The lower right image illustrates erosion intensity (t/km<sup>2</sup>/year), which can be used for regional decision making on soil erosion control and ecorehabilitation; No is none, VS is very slight, S is slight, M is medium, Inten is intensive, VI is very intensive and Sev is severe.

*Modelling regional soil erosion*

Equation 1 allows runoff modulus ( $\text{kL}/\text{km}^2/\text{year}$ ) to be used as a measure of relevant hydrology factors ( $Q$ ) and soil antiscourability ( $\text{kg}/\text{kL}$ ) as a measure of soil factors ( $S$ ). Information for the landform factor ( $g$ ) can be derived from regional DEMs, where the relative relief—the maximum elevation difference in a specified area—is used (Xinhua Liu et al. 2001). The remaining two factors, the vegetation index and soil conservation index, can be derived from advanced very high resolution radiometer (AVHRR) data (see Chapter 16 for further details) and soil conservation statistics, respectively.

### Discussion

It is possible and practical to quantitatively assess and predict macro trends in soil erosion at the regional scale, using the theory and methodologies of regional soil conservation and GIS. The methodology involves:

- dividing the study area into discrete units in space and time with homogeneous factors and erosion types based on the analysis of processes and the spatial differentiation of soil erosion and related environmental factors at the regional scale;
- using research on the factors affecting regional erosion and the results of erosion evaluation studies, coordinated with the characters of GIS modelling methods, to identify the relevant parameters of the model;
- extracting the parameters one by one from many kinds of approaches, including field tests, thematic maps, descriptions of observed materials and remote sensing imagery/DEM analysis, and integrating all the parameters into the basic unit map to build up a parameter database; and
- establishing a statistical model for the sediment discharge (the sediment yield from erosion) and each relevant factor using geostatistical and correlative analysis methods.

Our study supports unpublished work of the national soil erosion survey that suggests that remote sensing, GIS and erosion modelling can be used to efficiently survey soil erosion at the national or provincial scale. In the 1980s, it took about 10 years to map soil erosion in China at the national scale using mainly manual methods; in 1998–2000, it took only two years to do the same using a combination of manual and computer methods. When we have all the basic information at the national scale, we will be able to survey erosion quantitatively and annually. The increased timeliness in providing a nationwide overview by performing this massive task in temporal GIS (TGIS, see Chapter 16) will allow cost–benefit analysis of soil conservation and ecological rehabilitation practices to feed back more quickly into policy decisions and directions. The development of this TGIS will not only allow monitoring of the environmental response, but also allow central government officials to determine the effectiveness of money spent in different regions.

### Conclusions

This study has shown that soil erosion can be assessed and predicted quantitatively at a regional scale; and that soil erosion at the national or provincial scale can be rapidly surveyed using remote sensing, GIS and erosion modelling. The information so provided will assist macro policy making at the national and provincial levels. The accurate evaluation and prediction of regional soil erosion should be based on systematic research on the genesis and evolution of erosion at the macro scale, and on the factors that cause erosion. The current situation is far from perfect; we are doing more work on this topic.

### References

- Burrough, P.A. 1998. Dynamic modeling and geo-computation. In: Karssenber, D. and Burrough, P.A., eds, *Environmental Modeling in GIS*. Utrecht University, The Netherlands, Faculty of Geographical Sciences.

- China's Agenda 21. 1994. White Paper on China's Population, Environment, and Development in the 21st Century. Beijing.
- Feng Jiao, Xiaoping Zhang and Rui Li 1998. Application of GPS in soil and water conservation. *Bulletin of Soil and Water Conservation*, 18(5), 32–34.
- Jiyang Liang 1992. Analysis and simulation of storm, runoff and sediment on the Loess Plateau. *Journal of Soil and Water Conservation*, 6(2), 12–16.
- Junjie Ma 1990. The regression analysis of soil erosion on loess hill and tableland in the middle of Shaanxi. *Journal of Soil and Water Conservation*, 4, 21–28.
- Kirkby, M.J., Imeson, A.G., Bergkamp, G. and Cammeraat, L.H. 1996. Scaling up processes and models from the field plot to the watershed and regional areas. *Journal of Soil and Water Conservation*, 391–396.
- Peihua Zhou 1988. The prediction and prevention of soil erosion in China in 2000. *Memoir of the Institute of Soil and Water Conservation, Academia Sinica*, 1988(7), 57–71.
- Posen, J.W., Boardman, J., Wilcox, B. and Valentin, C. 1996. Water erosion monitoring and experimentation for global change studies. *Journal of Soil and Water Conservation*, 386–390.
- Qinke Yang 1994. The classes and regions of soil erosion in China. In: *Soil Science Study in Modern Time*. Beijing, Agriculture, Science and Technology Publishing House.
- Qinke Yang 2001. Study on overlay and its application of digital map overlay analysis. In Rui Li and Qinke Yang, eds, *Study on Rapid Survey of Region Soil Erosion and Soil Conservation Information System*. Zhengzhou, Huanghe Water Resources Press, 126–134.
- Qinke Yang and Rui Li 1998. Review of quantitative assessment on soil erosion in China. *Bulletin of Soil and Water Conservation*, 18 (5), 13–18.
- Qinke Yang and Rui Li 1999. Application of GIS. In: Li Rui and Yang Qinke, eds, *Research on the Rapid Survey and Management Information System at Regional Scale*. Zhengzhou, Huanghe Water Resources Press, 19–24.
- QiuSheng Wang 1991. The mathematical model for vegetation control of soil erosion and its application. *Journal of Soil and Water Conservation*, 5(4), 68–72.
- Renard, K.G., Foster, G.R., Weesies, G.A., McCool, D.K. and Yoder, D.C. 1997. *Predicting Soil Erosion by Water: a guide to conservation planning with the revised universal soil erosive (RUSLE)*. Washington DC, United States Department of Agriculture, Agriculture Handbook, 703.
- Rui Li, Qinke Yang and Yong'an Zhao 1998. Application of spatial information technology in soil and water conservation of China. *Bulletin of Soil and Water Conservation*, 18(5), 1–5.
- Xianmo Zhu 1981a. The main types of water erosion and their related factors in the Loess Plateau (1). *Bulletin of Soil and Water Conservation*, 1981(3), 1–9.
- Xianmo Zhu 1981b. The main types of water erosion and their related factors in the Loess Plateau (2). *Bulletin of Soil and Water Conservation*, 1981(4), 13–18.
- Xianmo Zhu 1982a. The main types of water erosion and their related factors in the Loess Plateau (3). *Bulletin of Soil and Water Conservation*, 1982(1), 25–30.
- Xianmo Zhu 1982b. The main types of water erosion and their related factors in the Loess Plateau (4). *Bulletin of Soil and Water Conservation*, 1982(3), 40–44.
- Xianmo Zhu, Daizhong Cheng and Qinke Yang 1999. 1:15000,000 soil erosion map of China. In: *Atlas of Physical Geography of PRC (2nd edition)*. Beijing, Cartographic Publishing House, 200.
- Xinhua Liu, Qinke Yang and Rui Li 2001. Extraction of relief roughness and its application in regional erosion prediction in China. *Bulletin of Soil and Water Conservation*, 21(1), 57–59.

# 23 Assessing Cropland Using Geographical Information Systems and Land Survey Data: an Example from China

Yang Qinke,<sup>\*</sup> Tim R. McVicar,<sup>†</sup> Li Rui<sup>\*</sup> and Xiaoping Zhang<sup>\*</sup>

## Abstract

China's current cropland taxation policy is based on the results of a land survey carried out in the 1950s. There is an urgent need to evaluate cropland quality so that land can be taxed and managed using up-to-date information. In China, different agricultural areas are taxed at different rates, based on land evaluation assessment. Farmers on more favourable land pay higher levels of tax. This chapter describes how 15 parameters were integrated into basic polygons to create a database for use in land evaluation. The parameters were obtained mainly from the national land survey and included accumulated annual temperature, annual precipitation, soil organic matter, elevation, slope and soil erosion. We evaluated cropland for each of the polygons using ArcInfo and Foxbase, integrated the database with an aggregated model produced from cropland evaluation of Shaanxi Province and created maps of cropland classes and related tables of statistics.

中国的农业税率因土地质量而异，好地课税率高。现行的税率是根据 50 年代土地详查结果而定的，目前亟需对农地的质量重新评价，以便采用最新数据来征税和管理。本文将 15 个参数集成于地块单元以建立耕地评价数据库。这些参数主要来源于国土详查资料，也包括相关研究中积累的年气温、降水、土壤有机质、海拔、坡度和土壤侵蚀数据。在 ArcInfo 和 Foxbase 环境下评价每个地块的质量等级，将数据库与陕西省农地评价所生成的模型结合，得到农地质量等级图以及有关的统计图表。

<sup>\*</sup> Institute of Soil and Water Conservation, Chinese Academy of Sciences and Ministry of Water Resources, Yangling, Shaanxi 712100, PRC.  
Email: qkyang@ms.iswc.ac.cn

<sup>†</sup> CSIRO Land and Water, PO Box 1666, Canberra, ACT 2601, Australia.

Yang Qinke, McVicar, T.R., Li Rui and Xiaoping Zhang. 2002. Assessing cropland using geographical information systems and land survey data: an example from China. In: McVicar, T.R., Li Rui, Walker, J., Fitzpatrick, R.W. and Liu Changming (eds), *Regional Water and Soil Assessment for Managing Sustainable Agriculture in China and Australia*, ACIAR Monograph No. 84, 311–320.

THE QUALITY and quantity of cropland in China was surveyed in the 1950s, soon after the creation of the People's Republic of China. The cropland taxation policy used today is based on the results of this 1950s survey, which evaluated land according to its type (e.g. hills, tablelands and plains) and features (e.g. soil organic matter content, bulk and porosity). In China, farmers pay different tax rates depending on the land evaluation assessment. For example, farmers located on fertile soils close to water sources pay a higher tax rate than those located on relatively infertile soils with lower rainfall or less access to irrigation. Hence, land assessment plays a critical role in agricultural economies at both micro (farmer) and macro (all China) levels.

Since the original survey, farmers and/or government have introduced land improvement measures such as capital works, irrigation networks and improvements to low-quality soils. Because productivity of the land has changed greatly over the intervening years, the 1950s-based land taxation criteria are no longer appropriate. Consequently, it has become necessary to reassess the land in order to adjust the taxation regime in a rational and balanced way that takes into account regional land conditions.

In the early 1990s, aerial photographs were used to construct a nationwide land survey at a scale of 1:10,000 in agricultural areas and 1:50,000 in forest and grassland areas. To date, only the areas of land parcels have been mapped; land quality has not been evaluated. There is an urgent need to evaluate cropland quality so that land can be taxed and managed using up-to-date information.

Three classification systems have been used for nationwide land evaluation in China:

- the land capability classification of the United States Department of Agriculture (USDA) (Klingebiel and Montgomery 1961) (this system was used in 1982 by the central Chinese Government Office of the Second Soil Survey);

- the Food and Agriculture Organization land evaluation system (FAO 1976) (this system has been used to assess the suitability of the land for different purposes); and
- a hybrid system, based on the USDA and FAO methods, modified to suit Chinese conditions (Shi Yulin 1982) (this system was used to report at a scale of 1:1,000,000 for all China).

These systems of land evaluation are designed primarily to help set policies that use land resources sustainably at a regional and national scale, or to gain maximum benefit from land improvement practices (e.g. establishing an irrigation area) for minimal cost. Our aim was to improve the basis for land taxation by using land survey data and geographic information systems (GIS). Two key steps are reported here. First, we identified and mapped the land evaluation units using GIS overlay techniques and readily available regional databases. Second, we developed a land evaluation model in a GIS environment.

### Methodology

Land resources are affected by geographical factors (e.g. geomorphology, soil, vegetation, climate and hydrology) and socioeconomic factors (e.g. the infrastructure associated with agronomy, transportation and location). The quality of the land can be represented generally by the following equation:

$$Lq = f(c, g, s, p, e) \quad (1)$$

where  $Lq$  is a measure of land quality,  $c$  is a measure of climate,  $g$  is a measure of geomorphology,  $s$  is a measure of soil type,  $p$  is a measure of cropland infrastructure and  $e$  is a measure of economic conditions.

Land evaluation requires identification and mapping of the evaluation unit (the basic polygon), development of databases to be used in the analysis, and construction of a model to score the land with

respect to different (either real or potential) land uses. Additionally, maps and statistical summaries must be produced for the end user.

In this study, the parameters used, their ranking and their weight were taken from the guide for cropland evaluation of Shaanxi Province (Zhang Qifan 1994). The approach used was based on research from the West and from China. In the light of the information we have accumulated, our data handling capacity and trials in northern, central and southern Shaanxi Province (Zhang Qifan 1994), we believe that 15 parameters are required (Table 1). These parameters cover climate, geomorphology, soil, agricultural infrastructure and economic factors. Cropland quality maps are generally at a scale of 1:10,000, which is suitable for use in the field. The parameters and classes are listed in Tables 1 and 2 and can be expressed as:

$$P = \sum_{i=1}^n A_i K_i \quad (2)$$

where  $P$  is the score for the evaluation unit,  $A_i$  is a measure of the score for the specified factor,  $K_i$  is a measure of the weight of the specified factor, and  $n$  is the serial number of the evaluation unit (polygon).

### Study Area

The study was performed in Changwu County, which is located in western Shaanxi Province, in the south of the Loess Plateau and covers an area of 565.9 km<sup>2</sup>. Figure 1 shows the location of the study area. The dominant geomorphological types in the Loess Plateau are loess tablelands, loess hills and river plains. Background information about the plateau is contained in the Overview. Mean annual rainfall is 584.1 mm, mean annual temperature is 9.1°C and total annual sunshine is 1659.9 hours. A detailed land survey was completed in 1992 at a scale of 1:10,000 and the information has been upgraded yearly since 1995. The maps, tables and other related data are all managed in paper format and must be accessed manually (Office of the Land Detail Survey

of Changwu County 1994; Committee of the Land Detail Survey of Shaanxi Province 1987).

The six data sets used in this study, and the general data constructs, are described below.

- *Land-use maps* (1:10,000). These were produced from the detailed survey of land resources (Committee of the Land Detail Survey of Shaanxi Province 1987). Each polygon has two items of data: the land-use code, and the number of the polygon. Items recorded in the map table associated with each land-use polygon were the map-sheet code; the administrative region (village, township, county); the type of land use; the area of the polygon and lines (roads, canals, etc.); and the ownership of land. The map also shows a third class of land use classified mainly by environmental factors such as landform, soil type and slope.
- *Cropland slope maps* (1:10,000). These are based on the land-use map and contain data about the cropland slope for each polygon.
- *Land-use change maps* (1:10,000). These are based on the land-use update. Where land use has changed, the old land use, the new land use, and the date of change are recorded for each polygon.
- *Climate condition maps* (1:100,000). These include contour maps of annual precipitation and annual cumulative mean daily air temperature when the air temperature is greater than 10°C. Both were produced by the Meteorological Bureau of Changwu County, based on 40 years data.
- *Soil maps* (1:50,000). These include soil type and soil organic matter maps, based on soil survey data produced in 1980 by the Agricultural Bureau of Changwu, Shaanxi Province.
- *Topographic maps* (1:10,000). These maps are produced by the Survey and Mapping Bureau of Shaanxi Province and are based on aerial photographs from flights conducted in 1976. The contour interval is 10 m.

**Table 1.** The 15 parameters (bold numbers) used in the land evaluation model, and the weighting factor (Wt), criteria and score used.

	Factor	Wt (%)	Criteria	Marks
Climate	<b>1</b> ≥10°C accumulated temp	8	> 4600	9
			4600–4300	8
			4300–4000	7
			4000–3700	6
			3700–3400	5
			3400–3100	4
			3100–2800	3
			2800–2500	2
			< 2500	1
			<b>2</b> Precipitation (mm)	10
640–600	8			
600–560	7			
560–520	6			
520–480	5			
480–440	4			
440–400	3			
400–360	2			
Geomorphology	<b>3</b> Elevation (m)	4	<400	9
			400–500	8
			500–600	7
			600–700	6
			700–800	5
			800–900	4
			900–1000	3
			1000–1100	2
			> 1100	1
			<b>4</b> Slope (°)	10
2–6	7			
6–15	5			
15–25	3			
> 25	1			
Soil	<b>5</b> Erosion	6	None	9
			Slight	7
			Medium	5
			Strong	3
			Severe	1
			<b>6</b> Depth (cm)	4
100–70	7			
70–50	5			
50–30	3			
<b>7</b> Texture	5	Fine sand	9	
		Clay/fine sand	7	
		Clay	5	
		Sandy/stone	3	
		Stone	1	
Soil (continued)	<b>8</b> Organic (%)	5	> 1.8	9
			1.8–1.6	8
			1.6–1.4	7
			1.4–1.2	6
			1.2–1.0	5
			1.0–0.8	4
			0.8–0.6	3
			0.6–0.4	2
			< 0.4	1
			<b>9</b> Saline or wet	5
0.6	6			
Slight	3			
Seasonal > 1.0 water < 0.5	0			
<b>10</b> Pollution	4	None	9	
		Slight	6	
		Medium Strong	3 0	
Condition of irrigation	<b>11</b> Irrigation	12	Irrigation if needed	9
			20% need	7
			Three times	5
			Twice	3
			Once	1
			Not possible <sup>a</sup>	0
<b>12</b> Contain water	8	Best	9	
		Better	7	
		OK	5	
		Poor Worse	3 1	
<b>13</b> Distance	7	< 1 km	9	
		1–2 km	7	
		2–3 km	5	
		3–4 km	3	
		> 4 km	1	
<b>14</b> Transport	6	Fair	9	
		OK Poor	5 1	
<b>15</b> Location	7	Very large city	9	
		Large city	7	
		Medium city	5	
		Small city	3	
		County Rural area	1 0	

<sup>a</sup> There is no infrastructure to irrigate the crops

## Generation of Parameters and Integration of Data

The spatial map unit is the basic polygon of the digital map. Each polygon has uniform attributes of land use, land management, cropping practice and related environmental factors. Figure 1 of Chapter 16 shows this stratification overlay concept. Additionally, each basic polygon has a definite boundary and area (Yang Qinke et al. 1985). In the field, the polygons are bounded by field engineering



**Figure 1** Shaanxi Province counties (Changwu County is shaded grey).

or clear line entities such as roads, canals, gullies or cliffs (Zhang Qifan 1994). Research and mapping of these units provided the basis for the scientific and practical evaluations in this study.

We used the land-use map as a basis for identifying and mapping the units, taking into consideration environmental factors and their relationship with land quality. Each unit has a unique identity and is related to one record in the attribute database; Table 3 shows an example of the database for 10 polygons. The overlaying and merging of the polygon attribute table (PAT) and ArcInfo (boundary of polygons) attributes table (AAT) were automated in order to manage the data. In the overlay process, the basic polygon map was used as a base map, with all the other maps overlaid in GIS. For integration, we added an item or parameter into the attribute table of the base map one or more times, as required. Figure 2 shows the steps in this process.

The data were manipulated in three ways:

- Attribute data with ArcInfo were used to map basic polygons and integrate them into multithematic maps. In this way, a database of parameters in the georelational data structure was developed, with multiple items describing each of

**Table 2.** Stratification of the land evaluation score into classes calculated from the 15 parameters and weighting factors, both introduced in Table 1, using Equation 2.

Class	Subclass	Score	Potential yield (kg/ha)	Class	Subclass	Score	Potential yield (kg/ha)
I	1	900–855	7500–7050	V	10	495–450	3450–3000
	2	855–810	7550–6600	VI	11	450–405	3000–2625
II	3	810–765	6600–6150	VII	12	405–360	2625–2250
	4	765–720	6150–5700		13	360–315	2250–1875
III	5	720–675	5700–5250	VIII	14	315–270	1875–1500
	6	675–630	5250–5175		15	270–225	1500–1125
IV	7	630–585	5175–4350	IX	16	225–180	1125–750
	8	585–540	4350–3525		17	180–135	750–225
V	9	540–495	3525–3450		18	135–0	<225

the basic polygons. Thematic management of data is easier than manual management.

- Cropland evaluation was scripted with SML (simple micro language of ArcInfo) and Foxbase, to calculate the cropland classes automatically.
- A cropland classes map was created by programming with SML according to the guide

to cropland evaluation issued by Shaanxi Province. Three categories and 25 types of table were also created automatically.

In order to avoid creating many erroneous new small polygons due to 'gaps' and 'slivers' (Burrough 1986) when overlaying two, or more, vector GIS data sources, we developed a new method, which is based on the selection of primary, secondary and

**Table 3.** An example set of the database for 10 polygons. The score of the 15 parameters (here called A1 to A15) results from the criteria and weighting introduced in Table 1. The final score, class and subclass are derived from Table 2.

Bnd	Poly#	LU	A1	A2	A3	A4	A5	A6	A7	A8	A9	A10	A11	A12	A13	A14	A15	Score	Class-Subclass
403	38-2	146	3200	530	1150	3	3	55	5	7	9	9	0	0	4500	1	0	289	VII-14
403	51-0	144	3200	530	1150	5	5	80	9	8	9	9	0	0	4500	1	0	349	VII-13
402	37-1	145	3100	540	1150	9	9	95	7	8	9	9	0	0	4500	1	0	395	VI-12
403	1-4	145	3300	530	1150	9	9	95	7	9	9	9	0	0	4500	1	0	408	VI-11
403	7	145	3300	530	1150	9	9	95	7	10	9	9	0	0	4500	1	0	408	VI-11
401	60	145	3200	540	1150	9	9	95	7	12	9	9	0	0	4500	1	0	413	VI-11
401	61-1	145	3200	540	1150	9	9	95	7	12	9	9	0	0	4500	1	0	413	VI-11
402	39	145	3200	540	1150	9	9	95	7	12	9	9	0	0	4500	1	0	413	VI-11
402	15-1	211	3200	540	1150	7	7	95	7	8	9	9	0	0	1000	1	0	413	VI-11
401	25	135	3200	540	1150	7	7	95	7	10	9	9	0	0	500	1	0	432	VI-11

bnd = administrative area code; poly# = no of the polygon of the parcel map; LU = code of land use

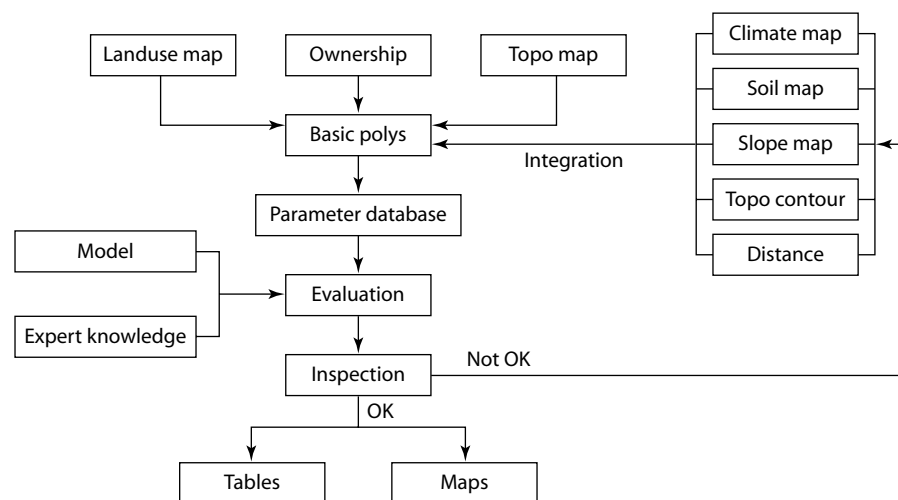


**Figure 2.** Flow chart of the development of the basic map unit for the land evaluation, the data used in generating the score and the inspection decision point. If the GIS-based land evaluation score, and hence the resulting class and subclass stratification, is deemed not okay, then the process cycles to reviewing the input data.

subsequent data layers in the GIS overlay process. In Figure 3, the upper two data layers are inputs to be overlapped, the primary layer is the top layer and the secondary layer the one below. The top layer has two attributes (A and B); the second layer also has two attributes (a and b). The attributes and areas are shown in 1.pat and 2.pat, respectively. The third layer is the result of overlaying the two input layers; this results in four polygons, which have attributes Aa, Ab, Ba and Bb, as shown in 3.pat. In 3.pat the spurious new polygons (Ab and Ba) are probably the result of slight misregistration of the vectors used in the two input data sets. In the lower data layer, the boundary from the primary data and the area of the resulting sliver polygons are used to assign the slivers to one of the two primary map units (see 4.pat). In addition to misregistration, there are instances where it is unnecessary or impossible for cartographers to locate the same ge- entity with the same geographic coordinates. This

may be due to different input data layers being produced by different mapping programs having slightly different, though related, thematic classes and these having different positional accuracies.

We extracted the parameters from a group of thematic maps, including those for slope, cumulative air temperature, precipitation, soil, soil organic matter, topographic shape, road network and village boundary. After entering the values into ArcInfo, we mapped the field data and other parameters, such as soil depth, texture, salinity, water-holding capacity and pollution, the state of irrigation and the location. The data were inserted into a common GIS, and each of the digital maps was projected using the Gauss–Krug projection—the official projection used in China for scales between 1:10,000 and 1:500,000. The land evaluation was programmed according to the method shown in Tables 1 and 2, with Equation 2,

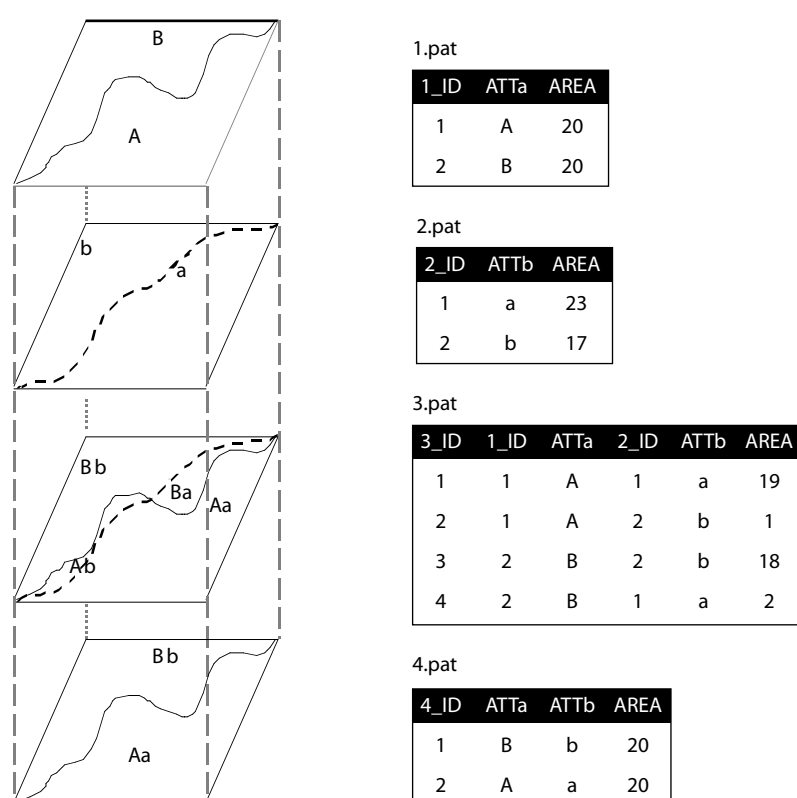


**Figure 3.** A schematic diagram illustrating the overlay procedure (see text for full details). The spatial data are denoted 1 to 4 from top to bottom.

using an extension developed in ArcInfo to deal with slivers (Figure 3).

The reliability of the land evaluation was verified by comparing the land evaluation map generated by GIS with the actual situation. The local government land surveyor helped to build a simple expert system, through their independent in situ databases. This allowed us to validate the quality of the data ingested and the approach used (specifically, the weighting values selected) for modelling the GIS-based land evaluation.

### Analysis

When assessing cropland for local government, the results should be repeatable, should be practical, and should be obtained using the methods specified by local government. This study meets these three criteria. The need for the assessment to be repeatable and transparent is particularly important in China, because land evaluation is used as the basis for tax rates for farming communities. Thus, farmers on high-quality fertile land adjacent to rivers, possibly with access to irrigation water, are taxed at a higher rate than farmers situated on lands with greater slopes or less fertile soils, and relying on rainwater or water that they haul to their farms.

We found that evaluating cropland using GIS gave results that were both theoretically and technically valid. The results of the evaluation, in either map or tabular format, were consistent with the actual situation for more than 95% of the polygons and are accepted by the farmers and local cadastral recorders. The method, the parameterisation, the mapping and the tabular data all closely followed the Shaanxi Province guide. All results, including maps, tables, and related documents, have been approved by scientists and officers of the Bureau of Land Management and Finance of Shaanxi Province. It is important to note that the results from this study have been endorsed by both the taxpayers (the farmers) and the tax collectors (government officers).

Land evaluation can be used not only for taxation management, but also for estimating grain yields, creating policies for cropland building and improvement, land management, and designing and building a practical land information system.

### Discussion

To build a parameter database for a region of China, it is more practical to use a spatial unit than to use soil series or land-type data. This is because China has more traditional cropping systems and technologies than the West, and a much greater degree of spatial, physical and socioeconomic variation. For example, the status of fertiliser use, field management and infrastructure is highly dependent on the distances between the land and the owners, and on transport conditions.

Multithematic map data can be integrated automatically by using GIS overlays and database manipulation. This can be achieved without generating spurious polygons, which can be an issue for GIS research and application (Burrough 1986; McAlpine and Cook 1971; Goodchild 1978; Arbia et al. 1998; Smith and Campbell 1989). A parameter database with multiple items for each polygon can be built efficiently using integration processes. The results of the integration reflect the macro features of environmental factors; errors in the land-evaluation GIS-based model were about 2% of the total number of base polygons (Table 4). Producing maps of 98% accuracy is acceptable to policy makers involved in land-evaluation assessment to decide farmer taxation levels. Parameterisation and evaluation can be programmed and integrated with GIS; the evaluation method has been automated and is hence repeatable.

### Conclusion

Information technology can be useful in managing land resources, but is in the early stages of development. It is time consuming to digitise land data (maps), and problems with raw data must be

**Table 4.** Differences in overlaying, shown as both m<sup>2</sup> and % area of the base map.

Accumulated temperature	Area (m <sup>2</sup> )		Difference	
	In base map	In attribute map	Area (m <sup>2</sup> )	%
3300	7,944,437	7,797,598	146,839	1.85
3400	11,547,616	11,488,230	59,386	0.51
3500	5,596,422	5,480,886	445,536	2.06

overcome when entering them into the GIS. These include maintaining accurate metadata, geometrically matching maps from different data sources; and keeping track of the temporal changes in GIS data sets. Many of these issues are areas of active research, and practical tools are starting to become available to operational users of GIS technology.

More research is needed on how to handle errors introduced during overlay processing through the removal of spurious polygons. There is also a need to assess the sensitivity of the final results by reducing the number of input GIS data layers from 15 to about four or five (hence simplifying the model). If the results are similar, then the method developed here can be more easily translated to other counties in the Loess Plateau, as the input data requirements will better match the regional data availability.

### Acknowledgments

Financial support was provided by ACIAR and by the Bureau of Land Management of Xian Yang City, Shaanxi Province, PRC.

### References

- Arbia, G., Griffith, D. and Haining, R. 1998. Error propagation modelling in raster GIS: overlay operations. *International Journal of Geographical Information Science*, 12, 2, 145–167.
- Burrough, P.A. 1986. *Principles of Geographical Information Systems for Land Resources Assessment*. Oxford, Clarendon Press.
- Committee of the Land Detail Survey of Shaanxi Province 1987. *Guide of the land detail survey of Shaanxi Province*, Xi'an.
- FAO (Food and Agriculture Organization) 1976. *A framework for land evaluation*. Soils Bulletin 32, FAO, Rome.
- Goodchild, M.F. 1978. Statistical aspects of the polygon overlay problem. In: Dutton, G., ed., *Harvard Papers on Geographic Information Systems*, 6, Addison-Wesley Reading, Mass.
- Klingebiel, A.A. and Montgomery, P.H. 1961. *Land-capability Classification of the United States Department of Agriculture (USDA) Agriculture Handbook 210*. Soil Conservation Service. USDA, Washington, DC.
- McAlpine, J.R. and Cook, B.G. 1971. Data reliability from map overlay. In: *Proceedings of the Australian and New Zealand Association for the Advancement of Science*, 43rd Congress, Brisbane, May. Section 21—Geographical Science.
- Office of the Land Detail Survey of Changwu County 1994. *The land resources in Changwu County*. Changwu, 1994–6.
- Shi Yulin 1982. *Guide of the land resources mapping at 1:1,000,000 in China*. *Journal of Natural Resources*.
- Smith, J.W.F. and Campbell, I.A. 1989. Error in polygon overlay processing of geomorphic data. *Earth Surface Processes and Landforms*, 14, 703–717.
- Yang Qinke, Song Guiqin, and Li Rui 1985. The mapping and discussion of basic polygon—a case study in Chang area. *Bulletin of Soil and Water Conservation*, 13, 5, 34–38.
- Zhang Qifan (ed.) 1994. *The theory and practice of the cropland evaluation*. Xi'an Map Press, Xi'an.